

---

# Dual-Frequency-Comb Two-Photon Spectroscopy

Arthur Hipke

---



München 2016



---

# Dual-Frequency-Comb Two-Photon Spectroscopy

Arthur Hipke

---

Dissertation  
an der Fakultät für Physik  
der Ludwig–Maximilians–Universität  
München

vorgelegt von  
Arthur Hipke  
aus Duschanbe

München, den 19.04.2016

Erstgutachter: Prof. Dr. Theodor W. Hänsch  
Zweitgutachter: Prof. Dr. Harald Weinfurter  
Tag der mündlichen Prüfung: 08.04.2016

# Zusammenfassung

Diese Arbeit hat experimentelle Demonstrationen einer neuartigen direkten Frequenzkamm-spektroskopietechnik zum Thema. Erzeuger optischer Frequenzkämme emittieren eine Vielzahl hochgradig kohärenter Lasermoden, deren Oszillationsfrequenzen abstandsgleich und eindeutig durch zwei messbare und einstellbare Radiofrequenzparameter sowie der ganzzahligen Modenzahl bestimmt sind. Direkte Frequenzkamm-spektroskopie kann traditionell durchgeführt werden, indem die Kammlinien des Frequenzkamms über die interessierenden Übergänge gescannt werden und ein Signal, das proportional zur gesamten Anregung durch alle Kammlinien ist, gemessen wird. Da die Moden, die zur Anregung beitragen nicht individuell bestimmt werden können, können die Übergangsfrequenzen nur modulo des Kammmodenabstandes gemessen werden. Die dadurch bedingten Limitationen werden durch die hier vorgestellte Technik, in der der erste Frequenzkamm mit einem zweiten Frequenzkamm in räumlichen Überlapp gebracht wird, überwunden. Die beiden Käme dieses sogenannten Zweikamm-aufbaus unterscheiden sich im Idealfall nur in ihren Träger-Einhüllenden-Frequenzen und ihren Pulswiederholraten. Die Interferenz zwischen den beiden Kämmen führt zu Schwebungen zwischen benachbarten Kammlinien, was effektiv die Anregungsamplituden eines jeden solchen Paares (bestehend aus je einer Kammlinie pro Kamm) moduliert. Folgerichtig ist die Anregungswahrscheinlichkeit durch ein jedes solches Kammlinienpaar ebenfalls mit der entsprechenden Schwebungsfrequenz moduliert. Diese Schwebungsfrequenzen sind im Abstand des Unterschieds der Pulswiederholraten angeordnet und sie kodieren eindeutig für einzelne Kammlinienpaare, was die Identifikation derjenigen Kammlinien ermöglicht, die die beobachtete Anregung bewirken.

In einer ersten Demonstration wurden Doppler-limitierte Einphotonenanregungsspektren der Übergänge  $5S_{1/2}-5P_{3/2}$  (bei 384 THz/780 nm),  $5P_{3/2}-5D_{3/2}$  und  $5P_{3/2}-5D_{5/2}$  (beide bei 386 THz/776 nm) und Zweiphotonenspektren des Übergangs  $5S_{1/2}-5D_{5/2}$  (bei  $2\times 385$  THz/ $2\times 778$  nm), mit hoher Übereinstimmung zu simulierten Spektren zeitgleich für beide stabilen Isotope von Rubidium gemessen. In einer Messzeit von 18 s wird ein Spektralbereich von über 10 THz (20 nm) abgedeckt und ein Signal-Rausch-Verhältnis (SRV) von 550 erzielt. Meines Wissens ist dies die erste Demonstration zweikammbasierter Zweiphotonenspektroskopie und fluoreszenzbasierter Zweikamm-spektroskopie.

In einem nachfolgenden Experiment an der gleichen Probe und den gleichen Zweiphotonenübergängen wird das Doppler-Auflösungslimit durch die Implementierung eines antiresonanten Rings überwunden. Die Eliminierung des Doppler-Effektes erster Ordnung ermöglicht es 33 Hyperfeinzweiphotonenübergänge aufzulösen. Die hochaufgelösten (1 MHz Messpunkt-abstand) und akkuraten (systematische Unsicherheit von  $\sim 340$  kHz) Spektren mit schmalen Übergangslinienbreiten (5 MHz) und hohem SRV ( $10^5$ ) sind – wie gezeigt wird – konsistent mit simulations-basierten Vorhersagen. Da die vermessene spektrale Spanne im Prinzip nur durch die Bandbreite der Anregungsquellen limitiert ist, scheint die Messung Doppler-freier Zweiphotonenspektren mit einigen 10 THz Breite in greifbare Nähe zu rücken.

Schließlich wird noch die Möglichkeit untersucht den Anwendungsbereich der Technik auf das Feld der Biochemie, z.B. auf Zweiphotonenmikroskopie, zu erweitern. Zu diesem Zwecke werden erste Hochgeschwindigkeitsmessungen bei niedriger Auflösung durchgeführt, mittels derer Kammstabilisierungsbedingungen und Einschränkungen für die vorgestellte hochgradig multiplexen Spektroskopietechnik identifizieren lassen, die sich aus ihrem begrenzten Dynamikbereich ergeben.



# Abstract

This thesis reports on experimental demonstrations of a novel direct frequency-comb spectroscopic technique for the measurement of one- and two-photon excitation spectra. An optical-frequency-comb generator emits a multitude of highly coherent laser modes whose oscillation frequencies are evenly spaced and uniquely determined by only two measurable and adjustable radio-frequency parameters and the integer-valued mode number. Direct frequency-comb spectroscopy can traditionally be performed by scanning the comb lines of the frequency comb across the transitions of interest and measuring a signal that is proportional to the excitation by all comb lines in concert. Since the modes that contribute to the excitation cannot be singled out, transition frequencies can only be measured modulo the comb-line spacing with this scheme. The so arising limitations are overcome by the technique presented here, where the first frequency comb is spatially overlapped with a second frequency comb. Both combs of this so-called dual-comb setup are ideally identical except for having different carrier-envelope frequencies and slightly different repetition rates. The interference between the two combs leads to beat notes between adjacent comb lines, forming pairs (with one line from each comb) with an effectively modulated excitation amplitudes. Consequently the probability of excitation by any given comb-line pair is also modulated at the respective beat-note frequency. These beat-note frequencies are spaced by the repetition-rate difference and uniquely encode for individual comb-line pairs, thus enabling the identification of the comb lines causing an observed excitation.

In a first demonstration, Doppler-limited one-photon excitation spectra of the transitions  $5S_{1/2}$ - $5P_{3/2}$  (at 384 THz/780 nm),  $5P_{3/2}$ - $5D_{3/2}$ , and  $5P_{3/2}$ - $5D_{5/2}$  (both at 386 THz/776 nm), and two-photon spectra of the  $5S_{1/2}$ - $5D_{5/2}$  (at  $2\times 385$  THz/ $2\times 778$  nm) transition, agreeing well with simulated spectra, are simultaneously measured for both stable Rb isotopes. Within an 18-s measurement time, a spectral range of more than 10 THz (20 nm) is covered at a signal-to-noise ratio (SNR) of up to 550. To my knowledge, this is the first demonstration of both dual-comb-based two-photon spectroscopy and fluorescence-based dual-comb spectroscopy.

In a follow-up experiment probing the same sample and two-photon transitions, the Doppler-resolution limit is overcome by implementation of an anti-resonant ring configuration. Cancellation of the first-order Doppler effect makes it possible to resolve 33 hyperfine two-photon transitions. The highly resolved (1 MHz point spacing), narrow transition-linewidth (5 MHz), accurate (systematic uncertainty of  $\sim 340$  kHz), high-SNR ( $10^4$ ) spectra are shown to be consistent with basic simulation-based predictions. As the spectral span is, in principle, only limited by the bandwidths of the excitation sources, the acquisition of Doppler-free two-photon spectra spanning 10s of THz appears to be in reach. To my knowledge, this is the first demonstration of Doppler-free Fourier-transform spectroscopy.

Lastly, the possibility of extending the technique's scope to applications in the field of biochemistry, such as two-photon microscopy, are explored. To that end, first high-speed, low-resolution ( $\gg 1$  GHz) experiments are carried out identifying comb-stabilization requirements and measurement constraints due to the limited dynamic range of the presented highly multiplexed spectroscopic technique.





# Contents

<b>Zusammenfassung</b>	<b>v</b>
<b>Abstract</b>	<b>vii</b>
<b>1 Introduction</b>	<b>1</b>
<b>2 Fundamentals of Dual-Comb Two-Photon Spectroscopy</b>	<b>5</b>
2.1 Two-Photon Phenomena & Two-Photon Spectroscopy . . . . .	6
2.2 Michelson-Based Interferometry . . . . .	9
2.3 Ultrafast Lasers and the Optical Frequency Comb . . . . .	13
2.4 Dual-Comb Linear Transmission Spectroscopy . . . . .	15
2.5 Dual-Comb Two-Photon Excitation Spectroscopy . . . . .	19
<b>3 Doppler-Limited Dual-Comb Two-Photon Spectroscopy</b>	<b>25</b>
3.1 Electronic Properties of Rubidium . . . . .	26
3.2 Operating Principle . . . . .	27
3.3 Experimental Setup . . . . .	29
3.4 Results and Discussion . . . . .	35
<b>4 Sub-Doppler Dual-Comb Two-Photon Spectroscopy</b>	<b>41</b>
4.1 Background . . . . .	42
4.1.1 General Principle of Doppler-Free Spectroscopy . . . . .	42
4.1.2 Hyperfine Energy Levels of Rubidium . . . . .	44
4.2 Experimental Setup . . . . .	45
4.2.1 Setup Overview . . . . .	45
4.2.2 Polarization of the Excitation Beams . . . . .	47
4.2.3 Frequency-Comb Stabilization and Phase-Correction-Signal Generation	47
4.2.4 Computation of a Single Interleaving-Step Spectrum . . . . .	49
4.2.4.1 Correction of Inter-Comb Phase Instabilities . . . . .	50
4.2.4.2 Calibration of the Frequency Scale . . . . .	52
4.2.5 Stitching of the Interleaved Spectra . . . . .	53
4.3 Results . . . . .	54
4.4 Analysis of Systematic and Statistical Errors . . . . .	60
4.4.1 Accuracy of the Frequency Scale . . . . .	60
4.4.2 Determination of the Transition Frequencies . . . . .	61
4.4.3 Transit-Time Broadening . . . . .	64
4.4.4 Magnetic-Field-Induced (Zeeman) Shifts . . . . .	64

4.4.5	Collisions and Impurities . . . . .	66
4.4.6	AC Stark Shift . . . . .	67
4.4.7	Frequency Pulling . . . . .	67
4.4.8	Systematic Effects Induced by the Dual-Comb Technique . . . . .	68
4.4.9	Errors from the Fit and Deviations from Literature Values . . . . .	69
4.5	Summary . . . . .	70
<b>5</b>	<b>Towards Liquid-Phase Dual-Comb Two-Photon Spectroscopy</b>	<b>73</b>
5.1	Background . . . . .	73
5.2	Experimental Setup . . . . .	75
5.3	Results and Discussion . . . . .	80
<b>6</b>	<b>Summary and Outlook</b>	<b>87</b>
<b>Appendix</b>		<b>89</b>
A	Supplementary Information on Doppler-Limited Dual-Comb Two-Photon Spectroscopy on Rb . . . . .	89
B	Supplementary Information on Doppler-Free Dual-Comb Two-Photon Spectroscopy on Rb . . . . .	91
B.1	Statistical Fit-Quality Measures . . . . .	91
B.2	Details on the Calculation of Transition Intensities . . . . .	91
C	Supplementary Information on Liquid-Phase Dual-Comb Two-Photon Spectroscopy . . . . .	93
C.1	Linear-Scale Liquid-Phase Dual-Comb Two-Photon Spectra . . . . .	93
C.2	Details on the Calculation of the Shot-Noise-Equivalent Power . . . . .	94
	<b>List of Abbreviations</b>	<b>96</b>
	<b>List of Figures</b>	<b>99</b>
	<b>List of Tables</b>	<b>100</b>
	<b>Bibliography</b>	<b>101</b>
	<b>Acknowledgements</b>	<b>114</b>
	<b>List of Publications</b>	<b>116</b>
	<b>Curriculum Vitae</b>	<b>118</b>

# 1 Introduction

Since their development at the end of the last century, optical frequency combs (OFCs) have strongly influenced a vast variety of research fields and inspired numerous innovative applications. As their leading developers were actively engaged in the field of metrology, OFCs were first applied to precision spectroscopy and the read-out of optical clocks, rendering cumbersome, lab-filling frequency chains obsolete [1]. In optical clocks, the OFC enables precise measurements of the frequency of a CW laser that is itself stabilized to a narrow high-frequency transition of an unperturbed atomic ensemble. These early experiments demonstrated the unprecedented power of the OFC to establish a well-calibrated frequency scale that was subsequently also harnessed for optical component metrology, the hunt for extrasolar planets, high-precision ranging, and much more [2]. Given that many of these developments are current hot topics of research, the Nobel committee's decision to honor the pioneer developers of the optical frequency comb, John L. Hall and Theodor W. Hänsch, with a half share of the 2005 Nobel prize in physics can only be called visionary.

Another field of research where OFCs are set to have a dramatic impact is the field of molecular spectroscopy. Much in the spirit of the late 1990's, when frequency chains were becoming obsolete, the current development of dual-optical-frequency-comb spectroscopy (short: DCS) aims at making one of the most widespread molecular-spectroscopy tools, the Michelson spectrometer, largely redundant.

In a scanning Michelson spectrometer [3], part of the light from an arbitrary light source is split, delayed, and recombined collinearly on a photodetector. The spectrum of the so-recorded time-domain interference trace is then obtained by Fourier transformation. The delay is typically introduced by a retroreflector mounted on a movable mechanical stage. The development of Michelson-based Fourier-transform spectroscopy (FTS) in the late 1950's triggered the end of the era of grating monochromators as the unrivaled standard tool for molecular spectroscopy. Today, a Fourier-transform spectrometer can be found in nearly every analytical chemistry laboratory of the developed world. This success is mainly owed to a few key advantages of FTS

over dispersion-based spectrometers [4, Sec. 2.2.2]: (i) The resolving power, defined as the ratio between the measured optical wavelength and the resolution, is increased by a factor of 10–100, (ii) The geometric throughput of light is also increased by a factor of 10–100 (Jacquinot’s advantage), (iii) The signal-to-noise ratio (for a given measurement time) and the consistency of spectra can be increased (multiplex advantage). The multiplex advantage, also called Fellgett’s advantage, originates in the fact that all wavelengths are measured simultaneously on only a single photodetector in FTS. This property is especially important for measurements in the mid-infrared wavelength region, where array detectors are rather noisy and expensive.

The delay-introduction mechanism is the defining property of a Michelson interferometer, and at the same time, it is the origin of its severest limitations: The acquisition rate is limited to video frequencies ( $\lesssim 100$  kHz) by the stage’s maximum travel speed, making it unsuitable for many instances of time resolved spectroscopy. The resolution is limited by the stage’s travel range of up to 10 m for commercially available devices, corresponding to a resolution of 15 MHz in terms of optical frequencies. In consequence, miniaturization attempts, i.e. by replacing the mechanical stage by other means to control the path difference, e.g. a piezoelectric transducer or a loudspeaker, always mean a trade-off between compactness and resolution. This causes medium-to-high resolution Michelson interferometers to be inherently bulky and expensive.

All of these limitations are overcome in DCS by the introduction of an alternate delay mechanism: The arbitrary light source of the Michelson interferometer is replaced by an ultrashort pulsed laser, periodically emitting pulses of coherent light at a set repetition rate, and the moving stage is replaced by a second ultrashort pulsed laser that has a repetition rate slightly differing from the first one. By virtue of the different repetition rates, the time separation between adjacent pulses (one pulse from each comb), i.e. the time delay, is discretely increased at a rate proportional to the repetition rate difference between the two lasers. The difference in repetition rates thus has an analogous effect as the moving mirror in a Michelson spectrometer when the spectrometer is operated using an ultrashort pulsed laser as its light source [5]. Once the two pulsed lasers of the DCS scheme are made sufficiently stable, i.e. they are converted into OFCs, molecular spectra can be acquired at radio frequencies (as high as 5 GHz [6] with commercially available technology), and a resolution without any limits imposed by the technique itself<sup>1</sup>. With the advent of  $\sim$ mm-sized OFC generators [7, 8] small-footprint inexpensive dual-comb spectrometer can be envisioned to become a ubiquitous tool in any research or industry that seeks to analyze matter optically.

---

<sup>1</sup>The potential resolution limit imposed by the comb-line spacing can be overcome by scanning the combs.

---

An important aspect of DCS, that has so far gone largely unexploited, and that has only recently attracted significant interest, is the superior ability of pulsed lasers to drive nonlinear transitions. The probability for nonlinear transitions to occur depends on the peak power of the excitation source, rather than its average power. Exploiting nonlinearities often enables a more efficient acquisition of spectra than would be possible by linear techniques. An important example for this is coherent anti-stokes Raman spectroscopy (CARS) where Raman spectra are measured exploiting CARS's  $E^6$  signal dependence, where  $E$  is the incoming electric field. In fact, one of the first proof-of-principle demonstrations of the potential of nonlinear DCS was performed using CARS [9]. This study by Ideguchi et al. demonstrates a previously unprecedented combination of broad spectral coverage (36 THz), high resolution (100 GHz), fast acquisition (measurement time 14.8  $\mu$ s), and high signal-to-noise ratio (210) in addition to showcasing the superb suitability of DCS for hyperspectral imaging.

Similar to the above example of Raman spectroscopy, multiphoton spectroscopy techniques can be used for samples with low intrinsic symmetry to more efficiently measure spectra that could also be measured with linear spectroscopies. This is particularly true for excitation wavelength regions like the ultraviolet, vacuum ultraviolet, or extreme ultraviolet, where primary laser sources are not always available and wavelength conversion is extremely tedious. More importantly, however, multiphoton spectroscopy allows access to spectroscopic information that cannot be acquired by means of linear spectroscopy. Textbook examples [10, Chap. 2] for this are the one-photon forbidden  $\Delta\ell = 0, 2$  transitions in atomic physics, or equal-parity transitions (gerade $\leftrightarrow$ gerade, ungerade $\leftrightarrow$ ungerade) in molecular physics. Moreover, nonlinear optical processes often have features that can be harnessed to overcome limitations encountered in linear spectroscopy. A paradigm example is the absorption of two photons with antiparallel wavevectors, which can be used to overcome the resolution limit set by Doppler broadening [10, Chap. 2]. Proving the feasibility of extending DCS to two-photon excitation spectroscopy, and hence combining their many advantageous properties lies at the heart of this thesis.

Traditionally, two-photon precision spectroscopy is performed by scanning either a powerful CW laser, a nanosecond (ns) pulsed laser, or a single frequency comb across the transitions of interest. In contrast, in dual-comb two-photon excitation spectroscopy (DC2pES), the technique introduced here, two frequency combs are used to irradiate the sample, and only need to be scanned if the inter-comb line separation is larger than the widths of the spectral lines of interest. DC2pES can be characterized as an extension of traditional direct (single) comb spectroscopy in which it becomes possible to identify the individual comb lines the sample is responding to. This is achieved by the addition of the second comb, leading to beat notes between pairs

of comb lines (one from each comb) that are close in frequency. The associated beat-note frequency is unique to each such pair of comb lines and is transferred to any excitation process that is stimulated by the respective comb line pair. This property of DC2pES eliminates the folding issue of direct single comb spectroscopy, where all spectral lines are folded and often overlapped in the tiny optical domain of half the comb's repetition rate. The elimination of the need to unfold spectra greatly simplifies the analysis of direct frequency comb spectral acquisitions and, for the first time, makes it applicable to excitation spectra of arbitrary number of levels, transition frequencies, and linewidths.

Compared to the CW-laser- and ns-pulsed-laser-based techniques, DC2pES has the obvious advantage of being broadband. A large frequency range of transitions is covered at once, without the need of performing rapid scans, which frequently leads to mode hops. This advantage comes without any cost in excitation efficiency: The resonance condition for excitation of a given transition can be satisfied by many pairs of comb lines, so that the excitation probability of any single level can be the same as for a resonantly tuned CW laser of the same average power [11, 12]. In the presence of intermediate levels within the combs' bandwidths, the excitation efficiency tips even more in favor of comb-excitation, because it intrinsically enables resonant multi-color excitation. Lastly, frequency conversion is much easier with pulsed laser sources than with CW lasers, so that a wider range of spectral domains can be covered cost-effectively. This is especially true if the frequency-converted CW lasers need to remain tunable.

The remaining part of this thesis is structured as follows: The **second chapter** provides a brief introduction into the concepts required for a solid understanding of the measured quantities, the most important basic tools used to perform these measurements, and the underlying concept describing how these tools work in concert. The **third chapter** describes the first proof-of-principle experiment of dual-comb two-photon spectroscopy. Within 18 s measurement time, fine-structure-resolved two-photon excitation spectra of natural rubidium are acquired with an excitation bandwidth of 10 THz and a Doppler-limited resolution of  $\sim 1$  GHz. The **fourth chapter** describes a further development of this experiment, overcoming the Doppler resolution barrier and achieving a transit-time broadening limited resolution of 7 MHz. 33 hyperfine transitions of natural rubidium are measured with an accuracy of better than a few 100 kHz. The **fifth chapter** extends the previous atomic gas-phase experiments to molecular liquid-phase experiments. First preparatory experiments, paving the way towards hyperspectral microscopy are reported. The **sixth chapter** concludes this thesis by providing an outlook onto possible future developments and applications of dual-comb two-photon spectroscopy.

# 2 Fundamentals of Dual-Comb Two-Photon Spectroscopy

In this thesis, I report on the development of a novel technique which involves two-photon excitation by two optical frequency combs. This chapter serves the purpose of establishing a conceptual and notational framework for the description of this technique. To that end, fundamental quantities associated with two-photon spectroscopy and interferometric principles are introduced. Thereafter, the light source used for two-photon excitation, the optical frequency comb (OFC), and the technique of linear dual-frequency-comb spectroscopy are introduced. The response of two-photon-absorbent samples to two-photon excitation in a dual-frequency-comb scheme is explored lastly. The sections of this chapter are outlined in the following way:

Dual-comb two-photon spectroscopy (DC2pES) is a particular two-photon spectroscopic technique that itself is a particular nonlinear spectroscopic technique. Section 2.1 of this chapter puts two-photon spectroscopy into the general context of nonlinear spectroscopy and fundamentally defines the measurement quantities.

Dual-comb spectroscopy (DCS) can be described in the time-domain as a cross-correlation measurement technique and in the frequency domain as a multi-heterodyne beat detection technique. Often times, more intuition can be gained in one domain than in the other and a basic understanding of the underlying working principles in both of these domains is generally beneficial. This understanding is provided in Sec. 2.2, by studying a system that shares many similarities with DCS: the Michelson interferometer.

The most commonly utilized generator of an OFC is a mode-locked laser. Section 2.3 gives a brief description of a mode-locked laser and establishes a link between its time-domain description as a pulsed laser and its frequency-domain description as a comb of lasing frequencies.

An understanding of nonlinear effects generally necessitates a solid understanding of related linear effects. To that end, Sec. 2.4 introduces linear DCS. The same section also introduces the concept of comb interleaving allowing high-resolution measurements.

Finally, in Sec. 2.5, DC2pES is introduced with its conceptually most intuitive interpretation as a Ramsey-type spectroscopic technique. Throughout the entire chapter, angular frequencies, denoted by  $\omega$ , will be used when notational clarity is paramount. However, in a few instances, such as when specifying repetition rates, it is much more common to instead use ordinary frequencies, denoted by  $f$ . This convention is adhered to in such cases.

## 2.1 Two-Photon Phenomena & Two-Photon Spectroscopy

Spectroscopic absorption-emission-based techniques measure the work that is done on an electric charge by an electromagnetic field. Within the framework of classical electrodynamics, the energy flow associated with electromagnetic fields is described by Poynting's theorem

$$-\nabla \cdot (\mathbf{E} \times \mathbf{H}) = \frac{\partial}{\partial t} \left( \frac{1}{2} \varepsilon_0 \mathbf{E} \cdot \mathbf{E} \right) + \mathbf{E} \cdot \frac{\partial \mathbf{P}}{\partial t} + \frac{\partial}{\partial t} \left( \frac{1}{2} \mu_0 \mathbf{H} \cdot \mathbf{H} \right) + \mathbf{H} \cdot \frac{\partial (\mu_0 \mathbf{M})}{\partial t} + \mathbf{E} \cdot \mathbf{J}_f, \quad (2.1)$$

which can be derived using Maxwell's equations and the Lorentz force. Here,  $\mathbf{E}$  is the electric field,  $\mathbf{H}$  is the magnetic field,  $\mathbf{P} = \mathbf{D} - \varepsilon_0 \mathbf{E}$  is electric polarization density with the the electric displacement  $\mathbf{D}$ ,  $\mathbf{M}$  is the magnetic polarization density,  $\varepsilon_0$  is the electric constant,  $\mu_0$  is the magnetic constant, and  $\mathbf{J}_f$  is the free current density. From Eq. 2.1 it can directly be seen that the energy exchange that is due to induced polarization of matter is given by the second term on the right hand side. Fundamentally, it is the average value of this term over multiple cycles of the electric field, i.e.

$$\frac{dW}{dt} = \langle \mathbf{E} \cdot \frac{\partial \mathbf{P}}{\partial t} \rangle, \quad (2.2)$$

that is studied in spectroscopic absorption-emission measurements [13]. In Eq. 2.2,  $W$  denotes the energy exchanged between the light beam and the irradiated matter.

$\mathbf{P}$  can generally be an arbitrarily complicated function, and for its analysis, one generally



resorts to the study of individual elements of its Taylor series expansion about  $\mathbf{E} = \mathbf{0}$ , i.e.

$$\mathbf{P}(\mathbf{E}) = \varepsilon_0 \left( \chi^{(1)} \cdot \mathbf{E} + \chi^{(2)} : \mathbf{E} \cdot \mathbf{E} + \chi^{(3)} \vdots \mathbf{E} \cdot \mathbf{E} \cdot \mathbf{E} + \dots \right). \quad (2.3)$$

This approach is valid for fields  $\mathbf{E}$  that are relatively weak compared to characteristic intraatomic, intramolecular, or crystalline fields. The electric susceptibilities  $\chi^{(n)}$  are tensors of rank  $n + 1$  that characterize the matter's response to the incident light field. This response cannot physically be instantaneous, and the material's polarization  $\mathbf{P}(t)$  at time  $t$  therefore depends on the incident electric field  $\mathbf{E}(t')$  at all times  $t' \leq t$ . Its time parametrization therefore reads

$$\begin{aligned} \mathbf{P}(t) = \varepsilon_0 \left( \int \chi^{(1)}(t_1) \cdot \mathbf{E}(t - t_1) dt_1 + \iint \chi^{(2)}(t_1, t_2) : \mathbf{E}(t - t_1) \cdot \mathbf{E}(t - t_1 - t_2) dt_1 dt_2 \right. \\ \left. + \iiint \chi^{(3)}(t_1, t_2, t_3) \vdots \mathbf{E}(t - t_1) \cdot \mathbf{E}(t - t_1 - t_2) \cdot \mathbf{E}(t - t_1 - t_2 - t_3) dt_1 dt_2 dt_3 + \dots \right). \end{aligned} \quad (2.4)$$

Representing the incident electric field in the form of a sum of plane monochromatic waves,  $\mathbf{E}(t) = \sum_i \mathcal{E}(\omega_i) \exp(-i\omega_i t)$ , the Fourier-transform of Eq. 2.4 is given by

$$\begin{aligned} \mathbf{P}(\omega) = \varepsilon_0 \sum_{i,j,k} \left( \chi^{(1)}(-\omega; \omega_i) \cdot \mathcal{E}(\omega_i) \delta(\omega_i - \omega) + \chi^{(2)}(-\omega; \omega_i, \omega_j) : \mathcal{E}(\omega_i) \cdot \mathcal{E}(\omega_j) \delta(\omega_i + \omega_j - \omega) \right. \\ \left. + \chi^{(3)}(-\omega; \omega_i, \omega_j, \omega_k) \vdots \mathcal{E}(\omega_i) \cdot \mathcal{E}(\omega_j) \cdot \mathcal{E}(\omega_k) \delta(\omega_i + \omega_j + \omega_k - \omega) + \dots \right), \end{aligned} \quad (2.5)$$

where, in keeping with the common Maker-Terhune notation,

$$\begin{aligned} \chi^{(1)}(-\omega; \omega_i) &= \tilde{\chi}^{(1)}(\omega_i), \\ \chi^{(2)}(-\omega; \omega_i, \omega_j) &= \tilde{\chi}^{(2)}(\omega_i + \omega_j; \omega_i), \\ \chi^{(3)}(-\omega; \omega_i, \omega_j, \omega_k) &= \tilde{\chi}^{(3)}(\omega_i + \omega_j + \omega_k, \omega_i + \omega_j, \omega_i), \end{aligned} \quad (2.6)$$

and  $\tilde{\chi}^{(n)}(\omega_i + \omega_j + \dots, \dots, \omega_i)$  is the  $n$ -dimensional Fourier transform of  $\chi^{(n)}(t_1, \dots, t_n)$  [14, Chap. 5]. The  $\delta$ -functions in Eq. 2.5 originate in the discreteness of  $\mathbf{E}(t)$ .

Light-matter interactions are usually classified according to their E-field dependence following Eq. 2.3. One-photon absorption and one-photon stimulated emission are  $\chi^{(1)}$  processes [14, Chap. 6]. The polarization induced in these processes is linear in  $\mathbf{E}$  and the material response only produces field oscillations at frequencies equal to the frequencies of the incoming field.

In contrast, the nonlinear  $\chi^{(n \geq 2)}$  processes generally are frequency conversion processes. E.g. setting  $\omega_i = \omega_j = \omega_0$  in the second-order term of Eq. 2.5 gives  $\omega = 2\omega_0$ , which corresponds to second-harmonic generation (SHG), controlled by the second-order nonlinear susceptibility  $\chi_{\text{SHG}}^{(2)} = \chi^{(2)}(-2\omega_0; \omega_0, \omega_0)$ . Similarly, for  $\omega_i = \omega_1 \neq \omega_j = \omega_2$ , the nonlinear polarization can lead to sum-frequency generation (SFG)  $\omega_{\text{SFG}} = \omega_1 + \omega_2$ .

In the following, relationships between the polarization and two-photon absorption are established. For monochromatic waves with amplitudes  $\mathcal{E}$  and  $\mathcal{P}$  and the same frequency  $\omega$ , the time average in Eq. 2.2 is given by

$$\frac{dW}{dt} = \frac{1}{2} \omega \text{Im}(\mathcal{E} \cdot \mathcal{P}). \quad (2.7)$$

For two-photon absorption, the relevant nonlinear polarization is

$$\mathbf{P}(t) = \frac{1}{8} \chi^{(3)}(-\omega; \omega, \omega, -\omega) : \mathcal{E} \cdot \mathcal{E} \cdot \mathcal{E}^* \exp(i\omega t) \quad (2.8)$$

and the energy absorbed through two-photon processes is hence

$$\frac{dW}{dt} = \frac{8\pi^2 \omega}{\tilde{n}^2 c^2} I^2 \text{Im}(\chi^{(3)}), \quad (2.9)$$

where  $I = \mathcal{E} \mathcal{E}^* \tilde{n} c / (8\pi)$  is the intensity of the incident beam,  $\tilde{n}$  is the refractive index, and  $c$  is the speed of light. For time-varying amplitudes  $\mathcal{E}(t)$ , a consequence of the square dependence of  $dW/dt$  on the intensity  $I$  is, that the total absorbed energy  $W$  is dependent on its temporal shape. For equal average intensities  $\langle I \rangle$ ,  $W$  increases with increasing temporal confinement, i.e. decreasing temporal width, of  $\mathcal{E}$ . This statement, which similarly can be shown to be true for other nonlinear processes, has made pulsed lasers (see Sec. 2.3) ubiquitous in nonlinear spectroscopy.

In this thesis, the two-photon sum-frequency resonant components of  $\chi^{(3)}$  are measured. The resonant tensor elements describing two-photon absorption of a field oscillating at  $\omega_1$  and  $\omega_2$  are explicitly given in the electric-dipole approximation by [15]

$$\begin{aligned} \chi_{ijkl}^{(3)}(-\omega_1; -\omega_2, \omega_1, \omega_2) = & \frac{(N_o - N_t) / (\epsilon_0 6\hbar^3)}{\omega_{to} - (\omega_1 + \omega_2) - i\Gamma_{to}} \sum_b \left( \frac{(p_i)_{ob} (p_j)_{bt}}{\omega_{bo} - \omega_1} \right. \\ & \left. + \frac{(p_j)_{ob} (p_i)_{bt}}{\omega_{bo} - \omega_2} \right) \cdot \sum_b \left( \frac{(p_k)_{tb} (p_l)_{bo}}{\omega_{bo} - \omega_2} + \frac{(p_l)_{tb} (p_k)_{bo}}{\omega_{bo} - \omega_1} \right). \end{aligned} \quad (2.10)$$

In the above expression, the subscripts  $o$  and  $t$  denote the unperturbed energy eigenstates

of the atom or molecule fulfilling the resonance condition  $\omega_1 + \omega_2 = \omega_{to}$ ,  $b$  designates all other energy eigenstates, and  $i, j, k, l \in \{x, y, z\}$ . Relaxation rates are denoted  $\Gamma_{nm}$ , electric dipole moments  $p_{nm}$ , and number densities  $N_n$ . Bohr frequencies, denoted as  $\omega_{nm}$ , are defined by  $\omega_{nm} = (E_n - E_m)/\hbar$  [16, p. 119], where  $E_n$  and  $E_m$  denote the energy eigenvalue of the state identified by the subscript  $n$  and  $m$ , respectively. Analogously the attenuation of fields oscillating at  $\omega_2$  is described by the imaginary part of  $\chi^{(3)}(-\omega_2; -\omega_1, \omega_1, \omega_2)$ .

Traditionally, absorption processes are also described by phenomenological rate equations. The rate equation associated with two-photon absorption reads

$$\frac{dn_p}{dt} = \delta N F^2. \quad (2.11)$$

Here,  $dn_p/dt$  is the number of photons absorbed per unit time,  $N$  is the density of absorbing molecules,  $F = I/(\hbar\omega)$  is the photon flux, and  $\delta$  is the two-photon absorption cross section. Comparison of Eq. 2.11 with Eq. 2.9 yields

$$\delta = \frac{8\pi^2\hbar\omega^2}{\tilde{n}^2 c^2 N} \text{Im}(\chi^{(3)}). \quad (2.12)$$

The usefulness of absorption cross sections (if known for sufficiently many frequencies) is two-fold: (i) They can serve as identifiers by comparing them to cross sections of known substances. (ii) ‘‘The [...] cross section is the physical magnitude with which the current quantum field theories come down to earth.’’ [17]. I.e. cross sections can be used to derive structural information of the sample or a theoretical model by comparing one with the other. One possible tool that enables one to perform two-photon-absorption spectroscopy and measure absorption cross sections is the Michelson interferometer. A description of the basic working principle of this interferometer type is provided in the subsequent section.

## 2.2 Michelson-Based Interferometry

The oscillation frequencies of the electric field of visible light approximately range from 400 to 750 THz. These frequencies are much higher than the analog bandwidth of any currently available detector (at most of order 0.01 THz), and therefore cannot be measured directly in the time domain. Instead, the field’s frequency can be determined interferometrically, i.e. by creating a superposition of fields in a way that allows to extract the frequency of interest from measurements performed on the created superposition. One possible interferometer type that

can be used for this purpose is the Michelson interferometer. Interferometers of the Michelson type measure optical wavelengths  $\lambda$ , from which the optical frequencies can then be calculated using  $f = c/\lambda$ , and can be set up in the form shown in Fig. 2.1.

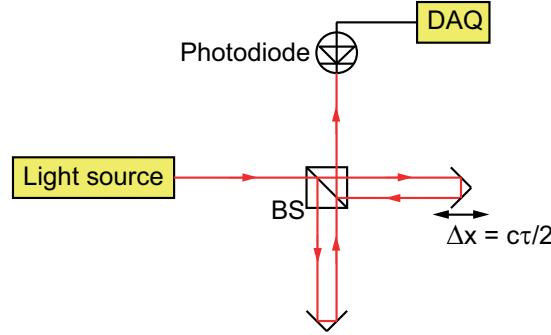


Figure 2.1: Schematic of a Michelson interferometer. The light source can be monochromatic, broadband, coherent, or incoherent. The delay-introducing moveable mirror is shown on the right-hand side. BS: beam splitter, DAQ: data acquisition system.

The measurement with a Michelson interferometer can be described in terms of heterodyne beat measurements, or in terms of autocorrelation measurements. The following description of Michelson-based measurements is structured as follows: In a preparatory step, the heterodyne signal generated by superposition of two monochromatic electric fields is described. Thereafter, the signal resulting from Michelson interferometers is described as a collinear linear interferometric autocorrelation. Finally, it is pointed out that the two approaches are merely two sides of the same coin.

The heterodyne signal, i.e. the time-domain intensity interference pattern  $S(t)$ , of two electric fields  $E(t) = \mathcal{E} \exp(-i\omega t) + c.c.$  and  $E'(t) = \mathcal{E}' \exp(-i\omega' t) + c.c.$  (including the time-independent relative phase in the complex amplitudes  $\mathcal{E}$  and  $\mathcal{E}'$ ) can be calculated as

$$\begin{aligned}
 S(t) &\propto |E(t) + E'(t)|^2 = \left| \mathcal{E} \exp(-i\omega t) + \mathcal{E}^* \exp(i\omega t) + \mathcal{E}' \exp(-i\omega' t) + \mathcal{E}'^* \exp(i\omega' t) \right|^2 \\
 &\propto \underbrace{\frac{1}{2} \mathcal{E} \mathcal{E}^* + \frac{1}{2} \mathcal{E}' \mathcal{E}'^*}_{\text{DC component}} + \underbrace{\mathcal{E} \mathcal{E}'^* \exp(-i(\omega - \omega')t)}_{\text{detectable AC frequency}} + \underbrace{\mathcal{E} \mathcal{E}' \exp(-i(\omega + \omega')t)}_{\text{optical frequency}} + \dots + c.c. \quad (2.13)
 \end{aligned}$$

Note that *c.c.* generally denotes the complex conjugate of all terms left of it. Knowledge of one of the frequencies,  $\omega$  or  $\omega'$ , and the sign of  $\omega - \omega'$  therefore allows one to determine the other frequency by only measuring this AC component, also often referred to as beat note.

For a monochromatic light source emitting the electric field  $E(t) = \mathcal{E}_0 \exp(-i\omega_0 t) + c.c.$ , the mea-

surement by a Michelson interferometer, can be identified as a collinear linear interferometric autocorrelation of form [18]

$$S(\tau) \propto \lim_{T \rightarrow \infty} \frac{1}{T} \int_0^T |\mathcal{E} \exp(-i\omega_0(t + \tau)) + \mathcal{E}^* \exp(i\omega_0(t + \tau)) + \mathcal{E}' \exp(-i\omega_0 t) + \mathcal{E}'^* \exp(i\omega_0 t)|^2 dt. \quad (2.14)$$

Experimentally, the delay  $\tau$  is introduced by movement of a beam-reflecting mirror as a function of time. Carrying out the same expansion as in Eq. 2.13 and keeping only the detectable frequency components one derives

$$S(\tau) \propto \frac{1}{2} \mathcal{E} \mathcal{E}^* + \frac{1}{2} \mathcal{E}' \mathcal{E}'^* + \mathcal{E} \mathcal{E}'^* \exp(-i\omega_0 \tau) + c.c.. \quad (2.15)$$

In Eq. 2.14 and 2.15  $\mathcal{E}$  denotes the amplitude of the field which was reflected by the moving mirror, and  $\mathcal{E}'$  denotes the amplitude of the field which was not reflected by the moving mirror. Common choices of  $\tau(t)$  are step-wise delaying, i.e. by steps of  $\tau_0$  via  $\tau(t) = \tau_0 \sum_{n=1}^N \Theta(t - n\Delta t)$ , where  $\Theta$  denotes the Heavyside step function, and linear delaying, i.e.  $\tau(t) = \frac{2v}{c} t$ , where  $v$  denotes the constant mirror velocity. In the first case, the measurement takes place while the mirror is not in translation, corresponding to homodyne detection. In the second case, the so-called “down-conversion factor”  $\frac{2v}{c}$  scales the optical frequency  $\omega_0$  down to the measurable video frequency  $\omega'_0 = \frac{2v}{c} \omega_0$ . Knowledge of the mirror velocity allows to deduce  $\omega_0$  from  $\omega'_0$ . From another point of view, the frequency  $\omega'_0$  equals the Doppler-effect-induced frequency shift imprinted onto the incoming light by the movement of the mirror. This establishes a correspondence between the notion of a heterodyne beat note and a linear-scan autocorrelation<sup>1</sup>: the latter records the heterodyne beat between  $\omega_0$  and  $\omega_0 + \omega'_0$ .

For both ways of translating the mirror, the acquired signal is a discrete set of measurement points<sup>2</sup>  $S(\tau_n)$  that, according to the Wiener-Khintchine theorem [14, Appx. 8D], contain all information necessary to calculate the light’s spectral amplitude by virtue of Fourier transformation. This spectral amplitude identifies all frequencies at which one-photon transitions can be stimulated by the light source.

Completely analogously to the linear (one-photon) regime described above, the frequencies at

<sup>1</sup>Strictly speaking, the Fourier-transform of a time-domain transmission signal can only be equated to the heterodyne detected signal, i.e. the frequency dispersed transmission spectrum, if the electric fields can be approximated by  $\delta$ -functions in the frequency domain. Differences arise e.g. for Lorentzian fields [19].

<sup>2</sup>For step-wise delaying, the digitization is given by the step size. For continuous delaying, the digitization is introduced by the analog-to-digital converter (ADC).

which two-photon transitions can be stimulated by the light source can be shown [20] to be given by the  $2\omega_0$  component of the collinear quadratic interferometric autocorrelation

$$S(\tau) \propto \lim_{T \rightarrow \infty} \frac{1}{T} \int_0^T \left| \left( \mathcal{E} \exp(-i\omega_0(t + \tau)) + \mathcal{E}^* \exp(i\omega_0(t + \tau)) \right. \right. \\ \left. \left. + \mathcal{E}' \exp(-i\omega_0 t) + \mathcal{E}'^* \exp(i\omega_0 t) \right) \right|^2 dt \quad (2.16)$$

$$= \frac{1}{2} |\mathcal{E}|^4 + 2 |\mathcal{E}|^2 |\mathcal{E}'|^2 + \frac{1}{2} |\mathcal{E}'|^4 + 2 \mathcal{E} \mathcal{E}^* \mathcal{E} \mathcal{E}'^* \exp(-i\omega_0 \tau) + 2 \mathcal{E} \mathcal{E}'^* \mathcal{E}' \mathcal{E}^* \exp(-i\omega_0 \tau) \\ + \mathcal{E} \mathcal{E} \mathcal{E}'^* \mathcal{E}'^* \exp(-i2\omega_0 \tau) + c.c.. \quad (2.17)$$

The measurement of a quadratic autocorrelation can e.g. be realized in practice by inserting a nonlinear crystal in between the beam splitter and the photodetector of Fig. 2.1 and detecting the light generated by SHG. Measuring the last term in Eq. 2.17,  $S_{2\omega_0}(\tau) = \mathcal{E} \mathcal{E} \mathcal{E}'^* \mathcal{E}'^* \exp(-i2\omega_0 \tau)$ , is analogous to, but more general than, measuring the factor  $I^2$  in Eq. 2.9. This can be seen when calculating the  $2\omega_0$  component  $S_{2\omega_0}(\tau)$  for the polychromatic field  $E(t) = \sum_{n=-N}^N 2\mathcal{E}_n \exp(-i(\omega_0 + n\Delta\omega)t - i\Phi_n) + c.c.$ , with constant phases  $\Phi_n$  and under the assumption of equal field amplitudes in the two interferometer arms and zero losses from the beam splitter:

$$S_{2\omega_0}(\tau) \propto \sum_{n=-N}^N \sum_{m=-N}^N \mathcal{E}_n \mathcal{E}_n \mathcal{E}_m \mathcal{E}_m \exp(-i(2\omega_0 + (n + m)\Delta\omega)\tau - i2(\Phi_n + \Phi_m)) + c.c.. \quad (2.18)$$

Equation 2.18 shows that the signal from quadratic interferometric autocorrelations is sensitive to the relative phase between interacting field components, in particular it is sensitive to the interference between different terms where  $n + m$  is the same. This phase-sensitivity is a phenomenon often termed multiphoton intrapulse interference. By appropriately tailoring the relative phases, this interference effect can e.g. be used to completely cancel the second-order signal (destructive interference) [21]. Because of its importance for Chap. 5, it might be worth restating here that the spectral amplitude obtained by Fourier transformation of  $S_{2\omega_0}(\tau)$  phase-sensitively identifies all frequencies at which two-photon transitions can be stimulated by the light source.

In transitioning from Eq. 2.16 to Eq. 2.18 the single-frequency electric field is replaced by a multiple-frequency electric field and each frequency component of the latter field is considered individually. An alternative approach to carry out this transition is to interpret  $\omega_0$  in Eq. 2.16 as the “carrier” frequency of a broadband light source emitting electric waves of now time-dependent amplitudes (or “pulse envelopes” or more precisely “pulse-train envelopes”)  $\mathcal{E}(t + \tau)$ ,

and  $\mathcal{E}'(t)$ , respectively. The introduction of the terminology and the concept of coherent broadband light sources is the goal of the next section.

## 2.3 Ultrafast Lasers and the Optical Frequency Comb

The distinction between wavelength and frequency measurements which is made in the previous section is notable in particular because both types of measurements are affected by different error sources. The relative accuracy of wavelength measurements is intrinsically limited to  $\sim 10^{-10}$  by geometric wave front errors, and achieving higher accuracies is only possible by measuring the frequency of light rather than its wavelength [1]. The ultimate tool for frequency measurements that has essentially rendered all other frequency measurement approaches obsolete is the subject of this section: the optical frequency comb (OFC).

The resonant optical cavity of a laser imposes boundary conditions on intra-cavity solutions of the wave equation. For an ideal empty cavity of length  $d$ , this constrain leads to wave solutions with wavelengths  $\lambda$  obeying

$$2d = n\lambda, n \in \mathbb{N}. \quad (2.19)$$

The round-trip frequency,  $f_{\text{rep}}$ , for light inside an empty cavity is given by  $f_{\text{rep}} = c/(2d)$  and the relationship between the wavelength and oscillation frequency is given by  $f = c/\lambda$ . Using these frequencies, the resonator condition 2.19 can be rewritten as

$$f_n = nf_{\text{rep}}, n \in \mathbb{N}. \quad (2.20)$$

Waves at these frequencies are also called longitudinal modes or the resonator's eigenmodes. Because of the regular spacing between adjacent modes by  $\Delta f = f_{\text{rep}}$ , the frequencies given by Eq. 2.20 are said to form a (harmonic) frequency comb. Virtually all applications of OFCs rely on, or at least benefit from highly coherent modes, which implies a fixed phase relationship between between all modes. This fixed phase relation is established through a group of techniques referred to as 'mode-locking'. The two techniques that are applied in lasers used for experiments described in this thesis are nonlinear-polarization-rotation and Kerr-lens mode locking. Both of these these techniques result in a mode-locking state where the phases of all modes coincide at one point in time  $t_0$  and, by virtue of periodicity of the involved functions at times  $t_0 + m/f_{\text{rep}}$ ,  $m \in \mathbb{Z}$ . As shown in Fig. 2.2, this coherent superposition of resonator modes results in the formation of pulses. To allow for a simplified and intuitive treatment of

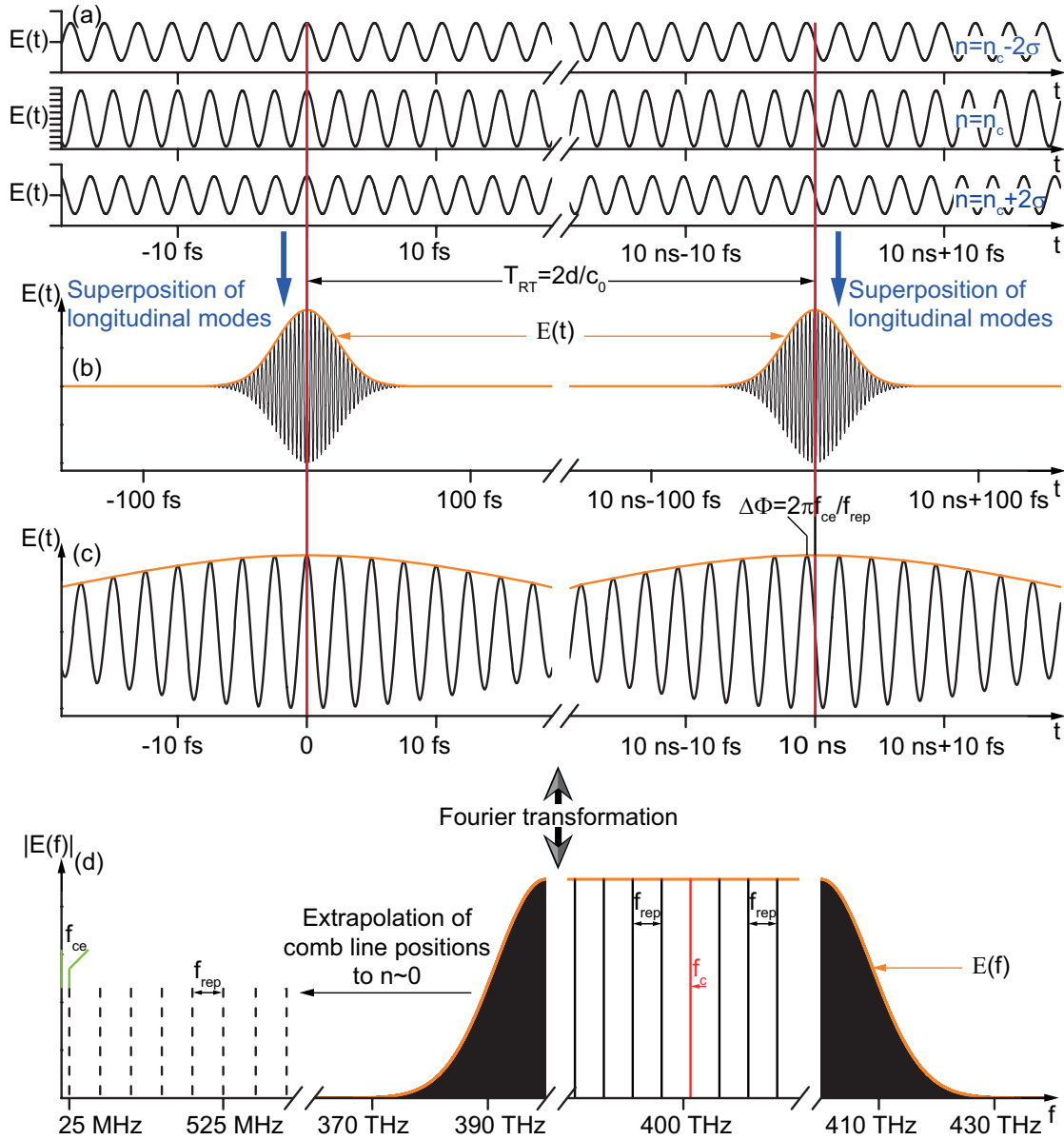


Figure 2.2: Principle of optical frequency comb generation. Panel (a): Individual longitudinal modes with Gaussian amplitude distribution  $E_n = 1/(\sigma \sqrt{2\pi}) \exp(-(n - n_c)^2/(2\sigma^2))$ ,  $n_c = 4 \cdot 10^6$ ,  $\sigma = 87381.5$ . The tick-spacing is equal on all three vertical scales. Panel (b): Linear superposition of  $2^{18} + 1$  modes of frequency  $f = 25$  MHz +  $n \cdot 100$  MHz,  $n = 3737856, \dots, 4262144$ . Panel (c): Zoom into the pulses shown in Panel (b). Panel (d): Frequency-domain picture that is connected to the above displayed time-domain picture via Fourier-transformation. The first frequency segment shows the extrapolated comb line positions around  $n = 0$ . The second and fourth frequency segment show the full frequency comb, including its spectral envelope, however, the comb lines are too dense to be individually visible. The third frequency segment shows the central part of the frequency comb on a smaller scale.

these pulses, they are often described by a “carrier” frequency  $f_c$  overlapped by an “envelope” function (also shown in Fig. 2.2).



An instrumental aspect of laser cavities that has so far gone unmentioned is that they, by definition, contain a gain medium. This gain medium, and possibly other elements like, e.g., air or mirror coatings, give rise to chromatic dispersion. As a consequence, the light's group velocity  $v_g = \partial\omega/\partial k = v_p(1 + \lambda/\tilde{n} \partial\tilde{n}/\partial\lambda)$  differs from its phase velocity  $v_p = \omega/k$  leading to a phase shift  $\Delta\Phi = (1/v_g - 1/v_p)2d\omega_c$  between consecutive pulses, i.e. from time  $t_0 + m/f_{\text{rep}}$  to time  $t_0 + (m + 1)/f_{\text{rep}}$ . In the preceding equations,  $k$  is the wavenumber, and  $\tilde{n}$  is the refractive index. A time dependent phase change corresponds to a frequency, in this case to the so-called carrier-envelope frequency denoted by  $f_{\text{ce}} = 1/(2\pi)f_{\text{rep}}\Delta\Phi$ . The addition of this frequency to Eq. 2.20 completes the so-called comb equation

$$f_n = f_{\text{ce}} + nf_{\text{rep}}, n \in \mathbb{N}. \quad (2.21)$$

The above description of OFCs largely leaves out effects of optical nonlinearities which, however, are often instrumental for their practical realizations and in-depth technological insight. Readers interested in such details are referred to Refs. [22, 23]. In this thesis, OFCs are only used as tools for spectroscopy experiments, and the accessible and intuitive picture provided in this section is well-suited for comprehending them. The following two sections introduce the specific employed spectroscopic technique, namely dual-comb spectroscopy.

## 2.4 Dual-Comb Linear Transmission Spectroscopy

This section details on how two OFCs can be combined to enable broadband spectroscopic measurements. The experimental setup of a dual-comb spectrometer is shown in Fig. 2.3. Two independent OFCs are combined on a beam splitter, propagate through the sample of interest, and illuminate a single photodetector.

The two combs are ideally identical except for differing comb-line frequencies. Let the comb-line frequencies of Comb 1 and 2 be given by  $f_{n,1} = f_{\text{ce},1} + nf_{\text{rep},1}$  and  $f_{m,2} = f_{\text{ce},2} + mf_{\text{rep},2}$ , respectively. The corresponding electric field then reads  $E_1(t) = \mathcal{E}_{n,1} \exp(-2\pi i f_{n,1} t) + c.c.$  for Comb 1 and  $E_2(t) = \mathcal{E}_{m,2} \exp(-2\pi i f_{m,2} t) + c.c.$  for Comb 2. Let  $E(t) = E_1(t) + E_2(t)$ , the interferometric time-domain beating signal as produced by the ‘‘dual-comb’’ and recorded by the photodetector then reads

$$S(t) \propto |E(t)|^2 = \sum_{n,m} \mathcal{E}_{n,1} \mathcal{E}_{m,2}^* \exp(2\pi i (f_{\text{ce},1} - f_{\text{ce},2} + nf_{\text{rep},1} - mf_{\text{rep},2})t) + c.c. \quad (2.22)$$

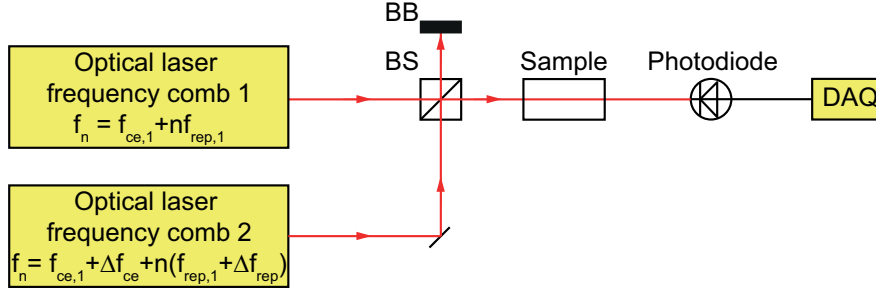


Figure 2.3: Schematic of a linear dual-comb spectrometer. The sample could also be placed in the beam path of only one of the two combs to allow for the measurement of phase spectra, however, the depicted configuration is the only one used in this thesis. BS: beam splitter, BB: beam block, DAQ: data acquisition system.

For operation of the dual-comb spectrometer, usually the  $n = m$  regime is chosen. When using  $\Delta f_{ce} = f_{ce,1} - f_{ce,2}$  and  $\Delta f_{rep} = f_{rep,1} - f_{rep,2}$  Eq. 2.22 becomes

$$S(t) \propto \sum_n \mathcal{E}_{n,1} \mathcal{E}_{n,2}^* \exp(2\pi i (\Delta f_{ce} + n \Delta f_{rep}) t) + c.c., \quad (2.23)$$

which itself is a frequency comb, usually consisting of frequencies in the radio frequency (RF) band. This RF comb has the frequency offset  $\Delta f_{ce}$ , line spacing  $\Delta f_{rep}$ , and its envelope is the product of the envelopes of the two OFCs. Superimposing Comb 1 and Comb 2 effectively down-converts Comb 1 (Comb 2) by the down-conversion factor  $\eta = \Delta f_{rep} / f_{rep,1}$  ( $\eta = \Delta f_{rep} / f_{rep,2}$ ). This factor is typically 1-3 orders of magnitude larger than the down-conversion factor of a Michelson interferometer (see Sec. 2.2), resulting in an acquisition rate of dual-comb spectra that is faster than the acquisition rate of Michelson spectra by the same 1-3 orders of magnitude. This gain in acquisition speed in conjunction with a resolution that is—in principle—only limited by the comb-line widths of the employed OFCs<sup>3</sup> are the two main factors driving the development of linear dual-comb spectroscopy. Figure 2.4 illustrates the principle of dual-comb spectroscopy in some more detail. All parameters therein were chosen to be realistic and generate informative visualizations at the same time.

The amplitude response of the sample on the transmission signal is usually included via the Beer-Lambert law

$$I(z) = I_0 \exp(-\kappa(\omega) \rho_0 z), \quad (2.24)$$

where  $\rho_0$  is the density of absorbers,  $z$  is the length of the absorption cell,  $\kappa(\omega) = \frac{4\pi\omega}{\tilde{n}(\omega)c} \text{Im}(\chi^{(1)}(\omega))$  is the absorption coefficient, and  $\tilde{n}(\omega) = \sqrt{1 + 4\pi \text{Re}(\chi^{(1)}(\omega))}$  is the index of refraction.

<sup>3</sup>OFCs with submillihertz linewidths are achieved by Schibli et al. [24].

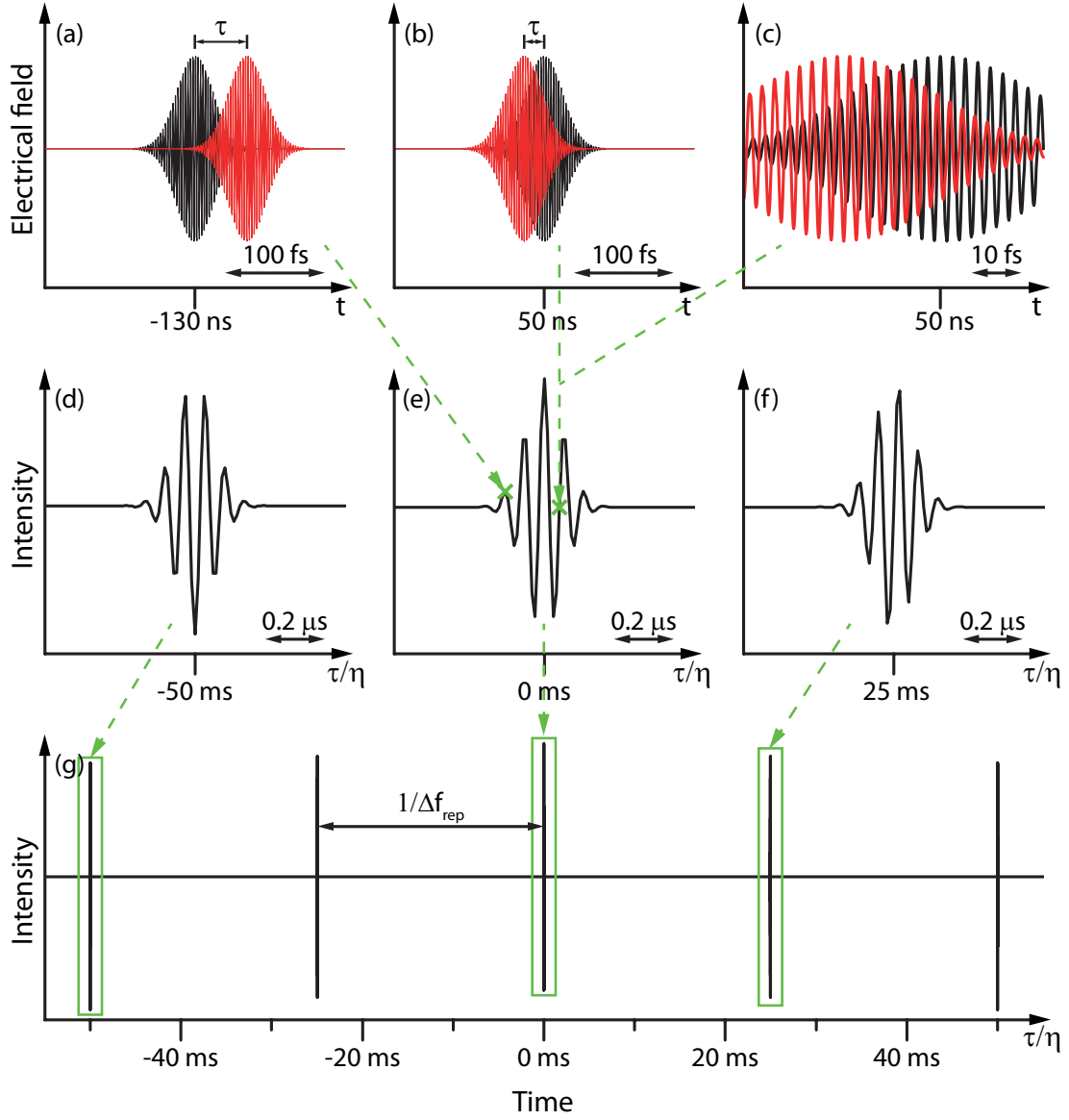


Figure 2.4: Time-domain principle of a dual-comb spectrometer. Panels (a-c) show the pulses emitted by Comb 1 (black) and Comb 2 (red) for an inter-pulse delay  $\tau$  of  $-52$  fs (a) and  $20$  fs (b,c). The time scale of Panel (c) is expanded compared to (a,b). The time  $t = 0$  is defined as the point in time where both pulses perfectly overlap and the pulse envelopes have their respective maximum value. The dual-comb time-domain intensity pattern arising from the linearly delayed pulses are shown in Panels (d-g). Each point in the latter panels corresponds to a single delay position. The two points corresponding to the graphs shown in the Panels (a-c) are marked by green crosses in Panel (e). The time scales of Panels (d-f) are expanded compared to (g). The simulation parameters for Comb 1 correspond to the ones used for Fig. 2.2, in particular  $f_{\text{ce},1} = 25$  MHz,  $f_{\text{rep},1} = 100$  MHz. Comb 2 differs from Comb 1 only in the two parameters  $f_{\text{ce},2} = f_{\text{ce},1} + 10$  Hz,  $f_{\text{rep},2} = f_{\text{rep},1} + 40$  Hz. The resulting dual-comb parameter  $\Delta f_{\text{ce}} = 10$  Hz leads to a carrier-envelope-phase change of  $2\pi\Delta f_{\text{ce}}/\Delta f_{\text{rep}} = \pi/2$  between Panel (e) and (f), and of  $\pi$  between (d) and (e). Panel (g) visualizes  $\Delta f_{\text{rep}} = f_{\text{rep},2} - f_{\text{rep},1} = 40$  Hz.

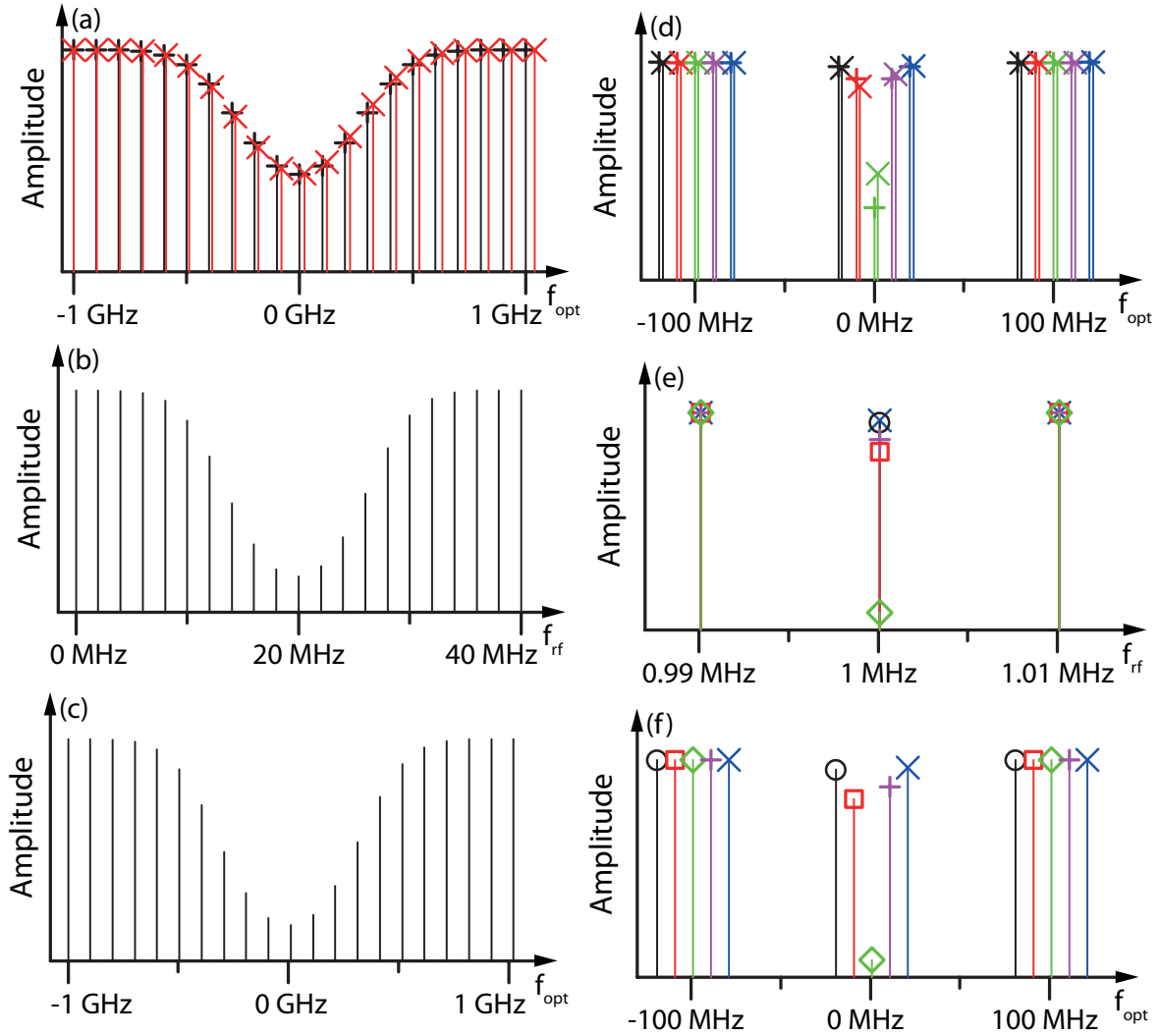


Figure 2.5: Simulated dual-comb absorption spectra, for an absorption line that is either broader (left panels) or narrower than the combs' mode spacings (right panels). Panel (a) shows how the dual-comb spectrally samples the (Gaussian) D2 absorption line of  $^{85}\text{Rb}$  at  $T = 321$  K, yielding a Doppler width of  $\Delta f_{\text{FWHM}} \approx 535$  MHz. The combs' repetition rates are  $f_{\text{rep},1} = 100$  MHz (black comb lines, “+” indicating comb line peaks) and  $f_{\text{rep},2} = 102$  MHz (red comb lines, “x” indicating comb line peaks). Panel (b) shows the inter-comb beat-note spectrum, yielding an RF comb. Knowledge of the combs' parameters allows to reconstruct the optical frequency axis of Panel (c). Panel (d) shows the spectral dual-comb sampling of the  $^{85}\text{Rb}$  D2 line assuming pure (Lorentzian) lifetime broadening,  $\Delta f_{\text{FWHM}} \approx 6.06$  MHz. Comb lines from the same dual-comb have the same color. Those comb lines drawn in red, green, magenta, blue are shifted from the black comb lines by 10, 20, 30, 40 MHz, respectively, by shifting both,  $f_{\text{ce},1}$  and  $f_{\text{ce},2}$ , by the respective amount. The value of  $\Delta f_{\text{rep}} = 10$  kHz chosen here is too small to be visible. Panel (e) shows the inter-comb beat-note spectrum, yielding five overlapping RF combs. They can be distinguished by their peak indicator symbol: circle=black, rectangle=red, diamond=green, +=magenta, x=blue. Knowledge of the combs' parameters allows to reconstruct the spectrally interleaved optical transmission spectrum shown in Panel (f).

With  $\omega_{ce} = 2\pi f_{ce}$ ,  $\omega_{rep} = 2\pi f_{rep}$ , and under the assumption  $\kappa(\omega_{ce,1} + n\omega_{rep,1}) \approx \kappa\left(\frac{\omega_{ce,1} + \omega_{ce,2}}{2} + n\frac{\omega_{rep,1} + \omega_{rep,2}}{2}\right) \approx \kappa(\omega_{ce,2} + n\omega_{rep,2})$ , Eq. 2.23 and Eq.2.24 can be combined to yield the intensity as a function of space and time:

$$S(t) \propto \sum_n \mathcal{E}_{n,1} \mathcal{E}_{n,2}^* \exp\left(-\kappa\left(\frac{\omega_{ce,1} + \omega_{ce,2}}{2} + n\left(\frac{\omega_{rep,1} + \omega_{rep,2}}{2}\right)\right)\rho_0 z\right) \exp(i(\Delta\omega_{ce} + n\Delta\omega_{rep})t) + c.c. . \quad (2.25)$$

The absorption spectrum can now easily be obtained by measuring the dual-comb spectrum with and without the sample and dividing the former by the latter. Figure 2.5 illustrates the sampling of an absorption line by a dual comb. It also illustrates how spectral interleaving can be used to overcome the potential resolution limit set by the mode spacing. Spectral interleaving can be performed by changing the comb-line positions of one or both combs of the dual comb and then measuring the dual-comb spectrum for each value of the changed parameters. In the case exemplified in Fig. 2.5, both  $f_{ce,1}$  and  $f_{ce,2}$  are changed by the same amount to scan over the absorption line. Since neither  $\Delta f_{ce}$  nor  $\Delta f_{rep}$  are affected by this change, the frequencies of the resulting RF comb coincide and the absorption spectrum becomes only apparent after individual retrieval of the optical frequency scale for each (optical) dual-comb position.

A dual-comb interferometer was first set up by S.-J. Lee et al. in 2001 [25] who used it for optical coherence tomography. Its use for linear spectroscopy was first proposed by S. Schiller in 2002 [26], and experimentally implemented first by F. Keilmann et al. in 2004 [27]. By now, many groups have built and utilized dual-comb spectrometers and the technique can be considered well-established. Nonlinear dual-comb spectroscopy, however, has only recently been experimentally demonstrated [28] and theoretically explored [19]. The next section introduces dual-comb-based two-photon spectroscopy.

## 2.5 Dual-Comb Two-Photon Excitation Spectroscopy

Dual-comb two-photon excitation spectroscopy (DC2pES) can most easily be understood conceptually as a Ramsey-type spectroscopic technique. The characteristic feature of this type of spectroscopies is the separation of the interaction of an atom with an oscillatory field into multiple (usually two) temporal windows in between which the atom time-evolves unperturbed by this field. In Ramsey's original implementation, an oscillatory (microwave) field was applied at two spatially separated positions to an atomic beam traveling at a constant thermal velocity [29]. Emphasizing the time-domain picture in DCS, this separation is due to the pulsed

nature of the excitation sources: A pulse from Comb 1 interacts with the sample at time  $t_0$ , the sample is left to evolve freely for a time  $\tau$ , and interacts with a pulse from Comb 2 at time  $t_0 + \tau$ .

In traditional optical Ramsey spectroscopy, the time delay between the pulses is generally fixed and the frequency (or phase between the pulses) is varied. The resonance positions and profiles are thus obtained by scanning of a cw [30] or ns-pulsed [31] laser through the sample's resonance transitions and measurement of the induced excitation. In contrast, the time delay is varied in DC2pES, whereas the laser frequencies remain fixed. The basic idea here is that the first pulse creates a coherent superposition of states, the superposition is then left to evolve freely for a variable period of time, and finally the second pulse either constructively or destructively builds on the excitation of the first impulse. The time evolution of the created superposition, predominantly determined by phase factors  $\exp(i(\Delta E/\hbar)\tau)$ , where  $\Delta E$  denotes the energy gaps between states of the superposition, can thus be sampled by scanning the time delay between the two pulses and measuring the induced excitation.

To arrive at a simple (but still meaningful) result, a few simplifications are made in the treatment of DC2pES compared to its experimental implementation. In accordance with the above definition of Ramsey spectroscopy (the sample is left to evolve freely between two distinguishable pulses)  $\tau$  is assumed to be larger than the temporal pulse width. The pulses are furthermore assumed to be rectangular in shape, and interactions between three or more pulses are not incorporated, thus leaving out any coherent pulse accumulation [32].

To describe the experimentally-observed oscillatory structure of the time-domain DC2pES signal, a semi-classical formalism originally developed for optical Ramsey spectroscopy on hydrogen atoms is repurposed. This formalism incorporates the discrete nature of the resonant excitation/emission frequencies (so-called Bohr frequencies), as well as the AC-Stark effect, which is intrinsic to any interaction between light and matter. Other effects, such as collisional shifts and broadening or transit-time broadening, are highly dependent on the specifics of the experimental configuration and are considered in the experimental chapters as they become relevant.

The time evolution of the wavefunction  $|\Psi\rangle$  of a sample particle is generally given by the Schrödinger equation, here with a time-dependent perturbative potential  $V(t)$ :

$$-i\hbar \frac{\partial}{\partial t} |\Psi(t)\rangle = H(t) |\Psi(t)\rangle, \text{ with } H(t) = H_0 + V(t). \quad (2.26)$$

Equation 2.26 does not account for relaxation and dephasing processes. Those are commonly conveyed in form of a damping matrix  $\Gamma(\rho)$  and included by switching to the Liouville equation

$$i\hbar \frac{\partial}{\partial t} \rho = [H(t), \rho] + i\hbar \Gamma(\rho), \quad (2.27)$$

where the density matrix, denoted by  $\rho$ , takes the role of the wavefunction  $|\Psi(t)\rangle$  in describing the quantum system's (mixed) state. For a two level system with eigenstates  $|a\rangle$  and  $|b\rangle$  and Bohr frequencies  $\omega_a, \omega_b$  (let without loss of generality  $\omega_a > \omega_b$ ) of the unperturbed Hamiltonian  $H_0$ ,  $V(t)$  and  $\Gamma(\rho)$  can be represented by

$$H_0 = \begin{pmatrix} \hbar\omega_a & 0 \\ 0 & \hbar\omega_b \end{pmatrix}, \quad V(t) = \begin{pmatrix} \hbar\Delta\omega_a(t) & V_{ab}(t) \\ V_{ab}^*(t) & \hbar\Delta\omega_b(t) \end{pmatrix}, \quad \Gamma(\rho) = \begin{pmatrix} \gamma\rho_{aa} & \frac{\gamma}{2}\rho_{ab} \\ \frac{\gamma}{2}\rho_{ba} & -\gamma\rho_{aa} \end{pmatrix}, \quad (2.28)$$

with field-induced shifts of the Bohr frequencies denoted by  $\Delta\omega_a(t)$  and  $\Delta\omega_b(t)$ ,  $\rho_{ij} = \langle i|\rho(t)|j\rangle$  with  $i, j \in \{a, b\}$ , and the relaxation rate of the higher-energy state given by  $\gamma$ . Then, with  $\omega_{ab} = \omega_a - \omega_b$  and the AC Stark shift  $\Delta\omega_{ab} = \Delta\omega_a - \Delta\omega_b$  the population of state  $|a\rangle$  to second order in  $V_{ab}(t)$  is given by [33]

$$\rho_{aa}^{(2)}(t) = \exp(-\gamma t) \left| \int_{-\infty}^t dt' \frac{V_{ab}(t')}{\hbar} \exp\left(i\omega_{ab}t' + i \int_{-\infty}^{t'} dt'' \Delta\omega_{ab}(t'') + \gamma t'/2\right) \right|^2. \quad (2.29)$$

For a two-photon resonant transition,  $V_{ab}(t)$  is of order two in the interaction potential  $H_1(t) = -\boldsymbol{\mu} \cdot \mathbf{E}(t)$ , where  $\boldsymbol{\mu}$  is the electric dipole operator. For an electric field of form  $\mathbf{E}(t) = \boldsymbol{\epsilon}\mathcal{E}(t) \exp(-i\omega_c t) + c.c.$ , where  $\boldsymbol{\epsilon}$  is a complex polarization vector having unit magnitude, it can be shown that  $V_{ab}(t)$  in principle contains all possible second-order mixing frequencies  $\Omega$  of  $\mathbf{E}(t)$  [33]. In traditional optical Ramsey spectroscopy, only those mixing products  $\Omega \approx \omega_{ab}$  are kept, arguing that the other mixing products lead to faster oscillations that average out on the measurement's time scale, an approximation called rotating-wave approximation. However, in time-domain spectroscopies, characteristically down-converting optical frequencies, fast population oscillations can be mapped to measurable frequencies and therefore must be kept. Consequently, the complexity of theoretical analysis is greatly increased. Amongst the terms contributing to  $V_{ab}(t)$  there will be

$$\frac{V_{ab}(t)}{\hbar} \propto 1/2\epsilon_0 c_0 \mathcal{E}(t)^2 \exp(-i\Omega t). \quad (2.30)$$

When assuming, for conceptual simplicity, rectangular pulses of width  $2\Delta t$ , i.e. with  $\mathcal{E}(t)$  of

form

$$\mathcal{E}(t) = \begin{cases} \mathcal{E}_0, & t_0 - \Delta t \leq t \leq t_0 + \Delta t \\ \mathcal{E}_0, & t_0 + \tau - \Delta t \leq t \leq t_0 + \tau + \Delta t \\ 0, & \text{otherwise,} \end{cases} \quad (2.31)$$

inserting Eq. 2.30 and Eq. 2.31 into Eq. 2.29, neglecting the AC Stark shift, and averaging  $\rho_{aa}^{(2)}(t)$  over all times  $t > t_0 + \tau$  one obtains

$$\rho_{aa}^{(2)}(\tau) \propto 4I_0^2 \Delta t^2 \text{sinc}((\omega_{ab} - \Omega)\Delta t)^2 / \gamma (1 + \exp(-\gamma\tau) + 2 \exp(-\gamma/2\tau) \cos((\omega_{ab} - \Omega)\tau)), \quad (2.32)$$

with  $I_0 = 1/2\epsilon_0 c_0 \mathcal{E}_0^2$ . In case the delay  $\tau$  is introduced with the dual-comb technique, for  $\Omega = 0$ ,  $\omega_{ab}$  is directly mapped to the radio-frequency  $\eta\omega_{ab}$  when  $\rho_{aa}^{(2)}(\tau)$  is measured. For  $\Omega = 2\omega_c$ , it predicts beat notes close to DC. These results are in agreement with a theoretical study by R. Glenn and S. Mukamel [19], identifying resonances centered at beat-note frequencies  $\omega_s = \eta\omega_{fg}$  and  $\omega_s = \eta(\omega_{fg} - 2\omega_c)$  for a three-band model consisting of  $|g\rangle$  (ground state),  $|e\rangle$  (intermediate state), and  $|f\rangle$  (final state), under full consideration of the excitation sources' harmonic comb structures. In this comprehensive treatment of DC2pES by these two authors, many more such resonances, are identified, most notably  $\omega_s = \eta\omega_{eg}$ , implying that also one-photon resonances can be measured with DC2pES.

It might be instructive to see what the condition  $\omega_s = \eta\omega_{fg}$  means in the optical domain for the case of dual-comb excitation. This condition originates in the term (Eq. 29 and Eq. A3 in Ref. [19])

$$S_{t1122}^{(3)}(\omega_s; \omega_{\text{rep},1}, \omega_{\text{rep},2}) \propto \text{Im} \left( \frac{\delta((r+n)\omega_{\text{rep},1} - (p+m)\omega_{\text{rep},2} - \omega_s)}{(n+r)\omega_{\text{rep},1} - \omega_{fg} + i\Gamma_{fg}} \right) \quad (2.33)$$

contributing to the stimulated two-photon absorption-emission spectrum. In Eq. 2.33,  $S_{t1122}^{(3)}$  denotes the third-order transmission spectrum capturing the spectral signature of all  $\chi^{(3)}$  processes. The indices  $r$  and  $n$  correspond to the two interactions with Comb 1, and the indices  $p$  and  $m$  correspond to the two interactions with Comb 2. Equation 2.33 is derived by assuming third-order susceptibilities of the form given in Eq. 2.10 and then solving Eq. 2.2 for a dual-comb excitation source. The  $\delta$ -function in Eq. 2.33, identifies the possible beat-note frequencies as the beats between pairwise sums of comb modes from Comb 1 and pairwise sums of comb modes from Comb 2. Combining  $\omega_s = (r+n)\omega_{\text{rep},1} - (p+m)\omega_{\text{rep},2}$  with  $\omega_s = \eta\omega_{fg}$ , and assuming a dual-comb of type  $r+n = p+m$  directly leads to the condition

$$(n+r)\omega_{\text{rep},1} = \omega_{fg} \quad (2.34)$$



which corresponds to the resonance condition of the denominator in Eq. 2.33. This shows that the condition  $\omega_s = \eta\omega_{fg}$  translates into one comb being tuned in resonance while the other is tuned slightly out of resonance by  $(n + r)\Delta\omega_{\text{rep}}$ . The measurement of  $\rho_{aa}^{(2)}(\tau)$  is experimentally realized in this thesis by measuring the fluorescence emitted from the upper state. In the experiments reported here, RF combs appearing around DC are high-pass filtered, and only those resonances appearing at  $\eta\omega_{fg}$  and  $\eta\omega_{eg}$  are measured. The following chapter reports on Doppler-limited DC2pES measurements of natural rubidium vapor.



# 3 Doppler-Limited Dual-Comb Two-Photon Spectroscopy

Michelson-based two-photon Fourier-transform spectroscopy was first demonstrated by Bellini et al. in 1997 [34]. In their setup they use a mode-locked Ti:Sa laser with a repetition rate of 82 MHz. Characteristically for a Michelson spectrometer, the laser beam is separated into two beams by a beam splitter, the two beams are delayed relative to each other, and then collinearly recombined on a beam combiner. The recombined beam is subsequently used to induce two-photon excited fluorescence in Cs contained in a vapor cell. By measuring the fluorescence intensity with a photomultiplier tube (PMT) as a function of the moving-mirror-introduced delay, they are able to record interferograms encoding the two-photon spectrum of Cs. The finite travel range of the stage they used for delay introduction of only  $\sim 300$  ps corresponds to a spectral resolution of 3 GHz. In particular, this resolution is a factor of 37 larger than the excitation source's mode spacing of 82 MHz. Subsequent to this first demonstration, a few investigations in the liquid phase at low resolution ( $>2$  THz) took advantage [20, 35, 36] of Michelson-based two-photon Fourier-transform spectroscopy. However, besides Ref. [34], no further reports on high-resolution ( $\lesssim 1$  GHz) gas-phase experiments are published that make use of this technique. Given the inherent stage-travel-range-induced limitation on the resolution, this only seems consequential.

As will be experimentally shown in the following, also in the case of two-photon excitation, any potential resolution limit set by the moving mirror can be overcome by replacing it with a second mode-locked laser, i.e. by performing dual-comb spectroscopy (as introduced in Sec. 2.4). Dual-comb spectrometers (DCS) were already shown to enable the acquisition of linear spectra at high (Doppler-limited) resolution [37], as well as, high signal-to-noise ratio [38], high sensitivity [39], and extremely short measurement times in the few- $\mu$ s range [40]. DCS's suitability for nonlinear spectroscopy was, however, so far only harnessed for dual-comb Raman spectroscopy [9, 28]. In this chapter, the scope of DCS is further broadened by demonstrating its suitability for the acquisition of Doppler-limited two-photon spectra.

Section 3.1 gives a roundup of the relevant electronic properties of Rb, in particular part of its energy level structure. While the operation principle of DC2pES is mathematically investigated in Sec. 2.5, a presumably more intuitive picture of the technique's operating principle is provided in Sec. 3.2. The experimental setup, along with a brief description of the utilized phase-correction scheme, is described in Sec. 3.3. The results are finally shown and discussed in Sec. 3.4.

## 3.1 Electronic Properties of Rubidium

Rubidium (Rb) is an alkali metal with an atomic number of 37 and an atomic mass of 85.46776(26) u [41]. Its naturally occurring isotopes are the stable  $^{85}\text{Rb}$ , accounting for 72% of Rb's natural abundance, and  $^{87}\text{Rb}$ , which has a half-life of 49 billion years, and accounts for the remaining 28%. Rubidium has only a single electron in the outermost atomic orbital, i.e. the valence orbital, whereas all inner orbitals are fully occupied. As a result, the repulsion between this valence electron and the other electrons is low. This allows to describe Rb's spectroscopic properties in a mean-field theory where the valence electron "sees" an effective potential resulting from the core's attraction potential and the other electrons' screening thereof [42, Chap. 6]. Because of its comparably simple spectroscopic structure, sharing many similarities with the spectroscopically simplest chemical element, Hydrogen, Rb was used early on in spectroscopy experiments elucidating the general electronic structure of atoms [43].

Besides the rather easily interpretable spectra, Rb also offers the benefit of having transitions in energetic regions easily accessible with widespread mature laser systems. The energy levels and transitions of Rb relevant here are shown in Fig. 3.1. Rubidium has a one-photon resonance ( $5S_{1/2}$ - $5P_{3/2}$ ) at 384 THz and two two-photon resonances ( $5S_{1/2}$ - $5D_{3/2}$  and  $5S_{1/2}$ - $5D_{5/2}$ ) at  $2 \times 385$  THz which are strongly enhanced by the presence of the nearby  $5P_{3/2}$  state. From the  $5D$  states, Rb atoms can decay into the  $6P$  manifold, from where they can emit fluorescence at 711 and 713 THz to repopulate the ground state. The ground state of both isotopes is split by a few GHz due to hyperfine interaction. The hyperfine splitting of the  $5D$  states amounts to less than 3% of the Doppler-width of  $\sim 1$  GHz at temperatures  $T$  of 308-393 K chosen in the experiments. It can therefore not be resolved by the Doppler-limited technique introduced here. All two-photon transitions between any (initial) ground hyperfine state (label  $g$ ) and any final hyperfine state (label  $f$ ) from the  $5S$  to the  $5D$  manifold have quantum numbers  $J_f \geq 3/2$  and either  $F_g \geq 2$ , or  $F_g \geq 1$  and  $F_f \geq 1$ . Because of this property, polarization-dependent

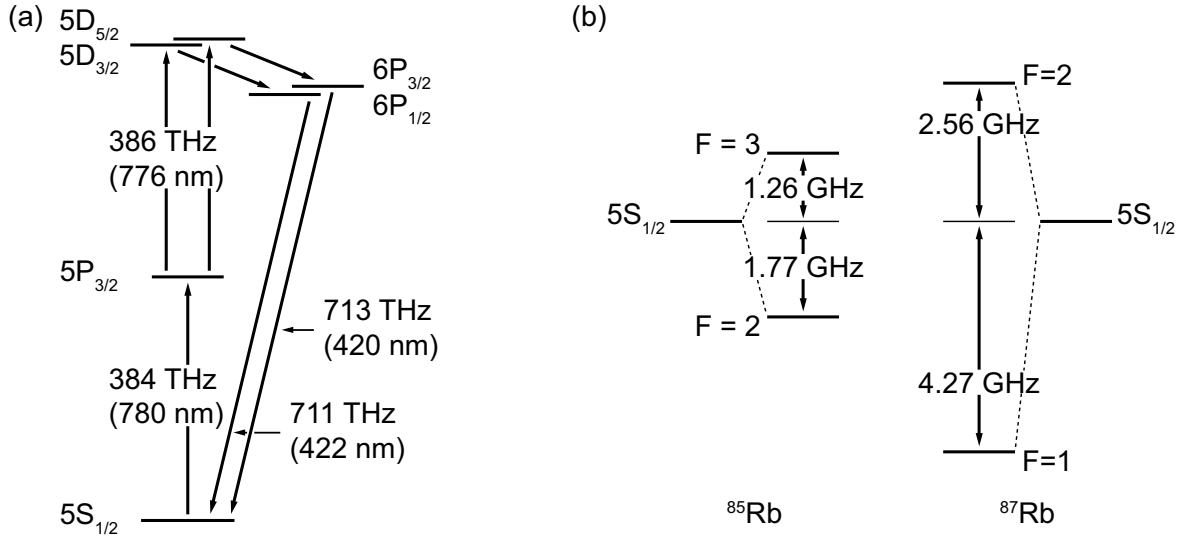


Figure 3.1: Experimentally relevant fine structure of rubidium (Panel (a)) and hyperfine structure of the  $5S$  ground state of  $^{85}\text{Rb}$  and  $^{87}\text{Rb}$  (Panel (b)).

two-photon absorption selection rules for photons of equal polarization do not cause transitions to be forbidden [44, Chap. 9]. An excitation source's polarization can therefore be chosen free of this consideration.

## 3.2 Operating Principle

The operating principle of dual-comb two-photon spectroscopy is sketched in Fig. 3.2. In the experiments presented here, mode-locked femtosecond lasers are used to drive two-photon transitions between a ground state  $|g\rangle$  and a final state  $|f\rangle$ . The population in the  $|f\rangle$  state is subsequently measured by recording the fluorescence emitted during decays back to the ground state. If there is an intermediate state  $|i\rangle$  roughly halfway between the  $|g\rangle$  and the  $|f\rangle$  states, the broadband lasers can also potentially drive one-photon transitions from  $|g\rangle$  to  $|i\rangle$  as well as transitions from  $|i\rangle$  to  $|f\rangle$ . One-photon transitions ( $|g\rangle$ - $|i\rangle$  and  $|i\rangle$ - $|f\rangle$ ) can be driven directly by comb lines within their resonance profile. For two-photon transitions ( $|g\rangle$ - $|f\rangle$ ), all pairs of comb lines from a single laser that add up to the resonant frequency can drive the transition. Because the comb lines are evenly spaced, the frequencies  $f_{\text{opt},2p}$  of all possible pairwise sums can be written as

$$f_{\text{opt},2p} = n' f_{\text{rep}} + 2f_{\text{ce}}, \quad (3.1)$$

where  $n'$  is integer-valued, and thus the excitation sources' effective two-photon spectra are themselves frequency combs.

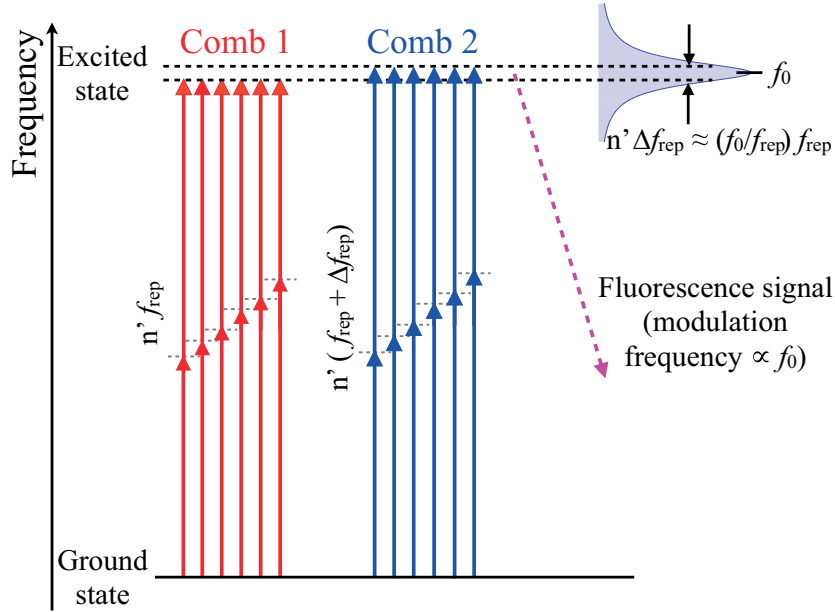


Figure 3.2: Frequency domain illustration of the principle of dual-comb two-photon spectroscopy. For simplicity, it is assumed in this figure that the carrier-envelope offset frequency of the two frequency combs is equal to zero. Pairs of comb modes with the same sum frequency ( $n'f_{\text{rep}}$  for Comb 1,  $n'(f_{\text{rep}} + \Delta f_{\text{rep}})$  for Comb 2) resonantly excite a two-photon transition at the optical frequency  $f_0$ . The excitation rate of the transition is modulated at the beat frequency  $n'\Delta f_{\text{rep}}$ , which is approximately equal to  $\frac{\Delta f_{\text{rep}}}{f_{\text{rep}}}f_0$ . An intensity modulation of frequency  $\frac{\Delta f_{\text{rep}}}{f_{\text{rep}}}f_0$  is thus observed in the fluorescence radiated during decays to lower states. As the frequency of the modulation is proportional to the transition frequency  $f_0$ , the two-photon excitation spectrum is revealed by Fourier transformation of the fluorescence intensity recorded versus time.

If the two lasers have slightly different repetition rates, a resonant excitation by a line from Comb 1 (either from the one-photon spectrum or the effective two-photon spectrum) can interfere with the excitation by the nearest (one- or two-photon) line from Comb 2, leading to a temporal modulation of the excitation probability. The frequency of the modulation is given by the frequency difference between the comb lines, i.e.,

$$f_{\text{RF},1\text{p}} = n\Delta f_{\text{rep}} + \Delta f_{\text{ce}} \quad (3.2)$$

$$f_{\text{RF},2\text{p}} = n'\Delta f_{\text{rep}} + 2\Delta f_{\text{ce}}, \quad (3.3)$$

where  $n$  is integer-valued,  $\Delta f_{\text{rep}} = f_{\text{rep},1} - f_{\text{rep},2}$  and  $\Delta f_{\text{ce}} = f_{\text{ce},1} - f_{\text{ce},2}$ . In effect, the optical frequencies of the comb lines are down-converted to the radio-frequency domain with a scaling factor  $\eta$  given by  $\eta = \Delta f_{\text{rep}}/f_{\text{rep}}$ . In the  $|g\rangle$ - $|f\rangle$  two-photon transition, the modulation of the excitation probability is directly transferred to the population of the  $|f\rangle$  state, and the amplitude of the modulation is directly proportional to the transition intensity. Modulations of the one-

photon transition can also modulate the population of the  $|f\rangle$  state, but because this requires a second transition either before (for  $|i\rangle\text{-}|f\rangle$ ) or after (for  $|g\rangle\text{-}|i\rangle$ ) the main transition, the amplitude of the modulation of the  $|f\rangle$ -state population measures a combination of the two one-photon transition intensities. In contrast to direct frequency-comb two-photon spectroscopy, a spectral feature can be uniquely assigned to a single comb line or groups of comb lines in the two-photon spectrum based on the frequency of the modulation.

### 3.3 Experimental Setup

For sample excitation, the outputs of two erbium comb generators (Menlo Systems, C-Comb + P100) are frequency doubled in magnesium-oxide-doped periodically poled lithium niobate (MgO:PPLN) crystals of a length of 0.3 mm (Covesion, MSHG1550), yielding spectra centered around 383 THz (783 nm), with a 10 dB spectral width of about 13 THz (27 nm). In the SHG, up to 300 mW of average input power are converted into an average SH power of up to 80 mW, corresponding to a conversion efficiency of 27%. For this  $f_{\text{rep}} = 100$  MHz laser system, these average power levels translate into peak powers of 3 nJ and 0.8 nJ, respectively. Supplementary information on spectral and temporal properties of the laser light before its conversion is compiled in Appx. A. The second-harmonic (SH) spectra of both combs are shown in Fig. 3.3. Both spectra show strong modulations with close-to-zero-intensity dips spaced at roughly 5 THz. Such modulations are a well-known phenomenon in SHG of broadband, high-peak-power pulses in PPLN crystals [45, 46]: In addition to the linear phases accumulation by the pump and the SHG beam—effectively matched by the poling-period of the PPLN—the phase can also be accumulated nonlinearly [47], being causative for spectral modulations and central-frequency shifts towards the blue or the red. The second-order interferometric auto-correlation traces associated with the discussed spectra are shown in the bottom panels of Fig. 3.3. No chirp-compensation is implemented to further reduce the measured temporal SH-pulse width of order 100 fs. LN crystals with apodized or chirped polings are currently being developed [48, 49] to minimize this effect, however, they were commercially unavailable at the time the experiments were carried out.

The full experimental setup is shown in Fig. 3.4. After the SHG, both beams are combined on a beam-splitter cube before the combined beam is focused into the sample. Each comb has an average power of  $\sim 20$  mW at the sample's position. The transmitted beam is recollimated and detected with a fast photodiode, while the sample's modulated fluorescence is detected with a

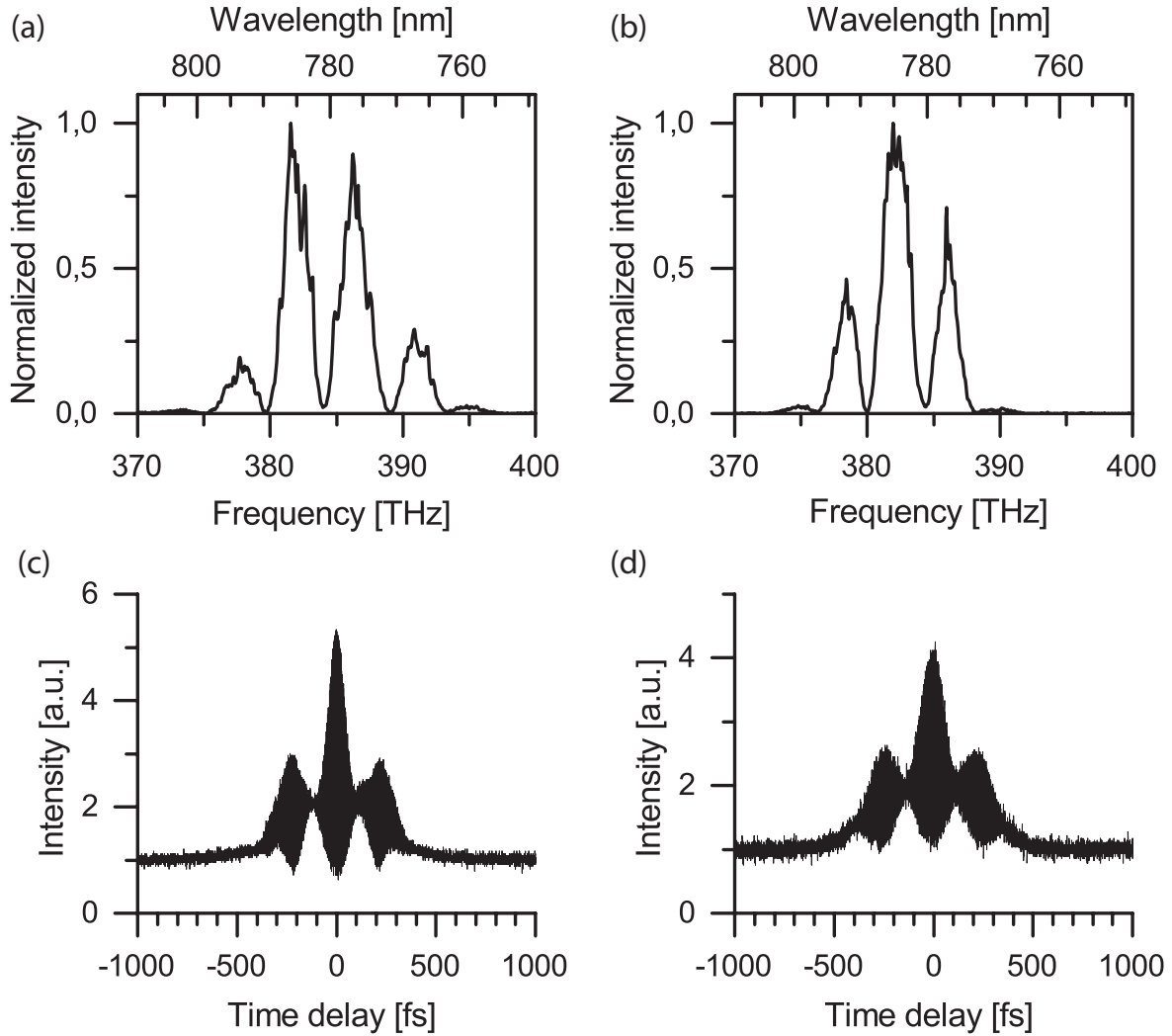


Figure 3.3: Spectrum and second-order interferometric autocorrelation trace of the SH light from Comb 1 (Panel (a) and (c)) and Comb 2 (Panel (b) and (d)). The pulse full width at half its maximum values (FWHM), corresponding to the widths of the central peaks of the autocorrelation traces, are 65 fs for Comb 1 and 98 fs for Comb 2. The widths of the pulse at the full width at half of the maximum values of the side lobes amounts to 374 fs and 416 fs, respectively.

photomultiplier tube. The detectors' outputs are digitized by a 14-bit analog-to-digital (AD) converter (AlazarTech, ATS9440) with a sampling rate of at most 125 MS/s.

The relatively long lifetime of the  $5D$  states  $\tau_{5D_{3/2}} = 246.3$  ns and  $\tau_{5D_{5/2}} = 238.5$  ns [50] acts as a low-pass filter on the modulated fluorescence signal in the radio-frequency domain, limiting the maximum modulation frequency to a few times the natural linewidth, i.e. 1–2 MHz. Such a filtering effect was already pointed out in frequency-modulation spectroscopy with an external modulator and is discussed in Ref. [51]. Therefore, a relatively low repetition-frequency



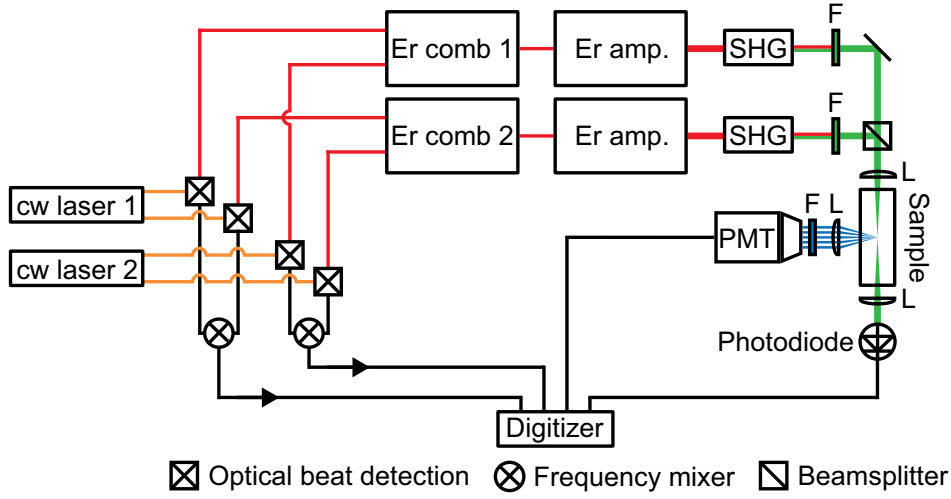


Figure 3.4: Experimental setup for Doppler-limited DC2pES of gas-phase rubidium. The beat-detection part to the left of this Fig., and the stabilization scheme that is left out here for clarity, is described in more detail in Fig. 3.5. SHG, second-harmonic generation; F, optical filter; L, plano-convex lens; PMT, photomultiplier tube.

difference of  $\Delta f_{\text{rep}} = 1$  Hz is chosen in the experiments reported in this chapter.

The so-recorded interferograms are, however, severely distorted by fluctuations of both the relative carrier-envelope phase and the repetition-rate difference. Distortion of the interferogram pattern can directly translate into distortions of the sample's absorption spectrum. Both, line shapes and line positions can be effected [52, 53, 54]. To reconstruct the unperturbed interferograms (and spectra), an *a posteriori* processing algorithm similar to what is reported in Ref. [55] is applied. The signals necessary for the correction are measured according to the schematic drawn in Fig. 3.5. They are derived from beating each Er oscillator individually with two free-running continuous-wave erbium-doped fiber laser (NKT Photonics, Koheras ADJUSTIK) emitting at 192 THz (1.56  $\mu\text{m}$ ) and 195 THz (1.53  $\mu\text{m}$ ), respectively. Electronically mixing the beating signals associated with the same CW laser leads to the isolation of a total of two lines of the RF comb with instantaneous frequencies<sup>1</sup>  $f_1(t)$  and  $f_2(t)$ . In the remainder of this section, it is described in detail how these two signals are generated and how they can be used to trace, and consequently correct, the fluctuations of both of the RF comb's degrees of freedom.

Panel (a) of Fig. 3.5 describes the generation of the correction signal  $f_1(t)$  derived from CW Laser 1 lasing at 192 THz. The beat notes with the two combs are detected in two separate beat

<sup>1</sup>The instantaneous frequencies  $f(t)$  of any time-dependent complex signal function  $s(t)$  can generally be defined as  $f(t) = \frac{1}{2\pi} \frac{d}{dt} \arg[s(t)]$ , where  $\arg[s(t)]$  yields the argument of  $s(t)$  [56].

### 3 Doppler-Limited Dual-Comb Two-Photon Spectroscopy

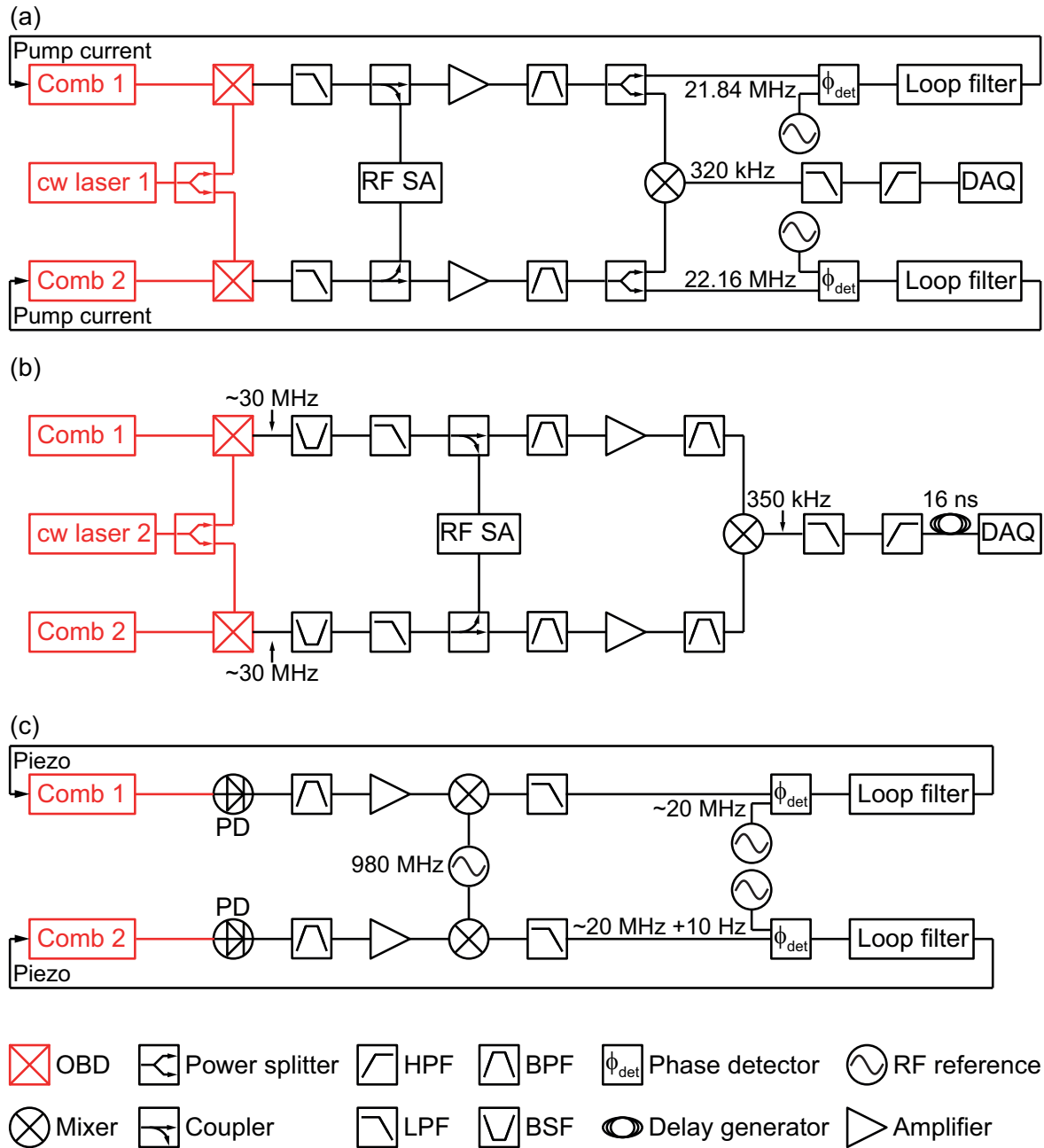


Figure 3.5: Frequency comb stabilization and phase-correction-signal generation. Primarily optical components are drawn in red, electrical components are drawn in black. OBD, optical beat detection; HPF, high-pass filter; LPF, low-pass filter; BPF, band-pass filter; BSF, band-stop filter; RF SA, radio-frequency spectrum analyzer; DAQ, data acquisition; PD, photo detector.

detection assemblies essentially consisting of waveplates for polarization control, polarizing beam splitters for intensity control, a non-polarizing beam combiner, optical filters, and a photo receiver. The so-detected beat signals are subsequently electronically filtered, amplified, and split by electronic splitters. Two of the outputs (one from each of the two electronic

splitters) are mixed by an electronic frequency mixer whose intermediate frequency output is then electronically filtered and digitized so serve as the first correction signal. The remaining outputs of the electronic splitters are used in a phase-locked loop (PLL) [57] to stabilize one comb line from Comb 1 and one comb line from Comb 2 to CW Laser 1 via feedback to the currents provided to the combs' pump diodes. Panel (b) of the same figure shows that—apart from using another CW laser now lasing at 195 THz—the second correction signal  $f_2(t)$  is generated in the same way as the first one. The only difference here is that the beat notes with CW Laser 2 are not used for frequency stabilization of the combs. Instead, the second comb-degree of freedom, the repetition rate  $f_{\text{rep}}$ , is stabilized to a radio-frequency reference via the scheme shown in Panel (c) of the same figure. In this scheme, the 10th harmonic of the repetition rate of each comb is detected on a photodiode (PD). The respective PD output is electronically filtered, amplified, and mixed with a 980 MHz RF synthesizer output to yield a 20 MHz signal which is then used in a PLL. The feedback signal thereof is applied to a piezoelectric transducer mounting one of the cavity end mirrors. This action adjusts the laser cavity length and is made possible by a small free-space section inside the cavity.

The frequency stabilization of the combs is primarily implemented to conveniently keep all beating signals within the passband of electronic filters and to ensure that the RF comb does not drift into a frequency region where the described natural-lifetime filtering effect becomes too impactful. These goals do not require well-tuned high performance PLLs and are even met with the rather broad beat signals shown in Fig. 3.6. In fact, it was shown in Ref. [37] that even completely free-running combs can be used to measure Doppler-limited spectra as long as a phase-correction scheme is simultaneously implemented.

The correction scheme implemented here works on the principle of correcting common-mode (label “cm”) fluctuations of the RF comb lines by multiplying the time-domain fluorescence signal by a time-varying phase factor  $e^{-i\phi_{\text{cm}}(t)}$  and subsequently correcting for differential (label “diff”) fluctuations by adjusting the sampling rate. If the phase is chosen to be either

$$\phi_{\text{cm}}(t) = 2\pi \int_{t-T/2}^{t+T/2} f_1(t') dt' \text{ or } \phi_{\text{cm}}(t) = 2\pi \int_{t-T/2}^{t+T/2} f_2(t') dt', \quad (3.4)$$

where  $T$  can e.g. be interpreted as the integration time of a sigma-delta type digitizer, either the first or the second RF comb line is shifted to zero frequency. In general, the correction phase can be derived from any affine combination of  $f_1$  and  $f_2$ , i.e.

$$\phi_{\text{cm}}(t) = 2\pi \int \alpha f_1(t') + (1 - \alpha) f_2(t') dt', \quad (3.5)$$

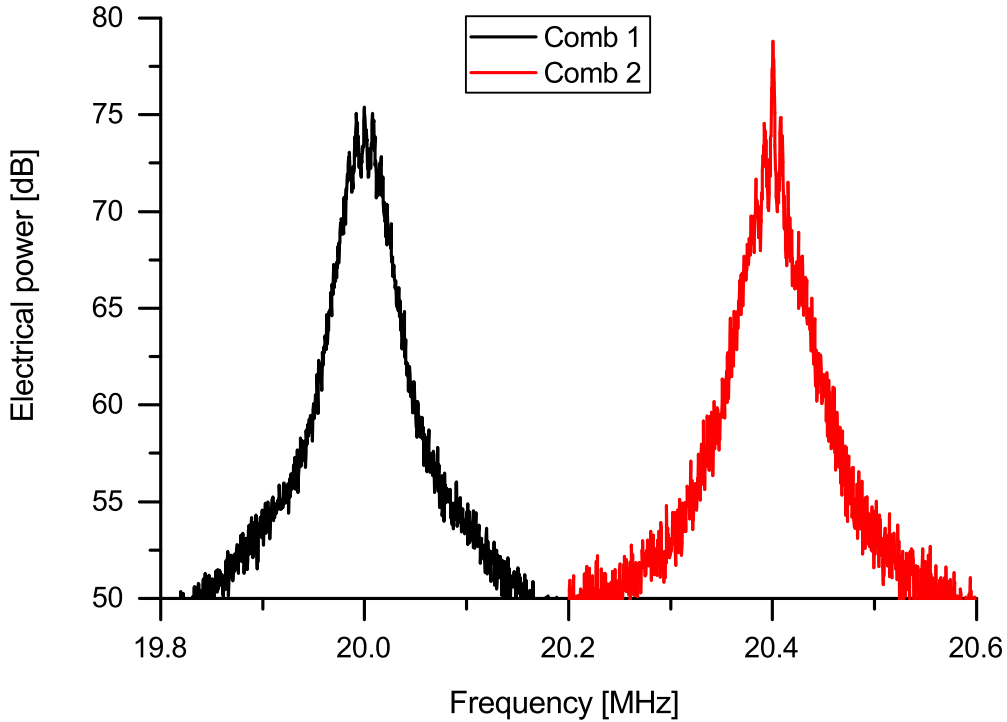


Figure 3.6: Beat-note measurement of Comb 1 (black) and Comb 2 (red) with CW Laser 1. Both combs are locked to this CW laser via the respective beat note. The central frequencies were changed slightly to the frequencies given in Panel (a) in Fig. 3.5 after this recording has been made. The spectra were recorded at a resolution bandwidth (RBW) of 3 kHz, a video bandwidth (VBW) of 3 kHz, and a sweep time (SWT) of 2 s.

where  $\alpha$  is an arbitrary real number. After the multiplication of the absorption interferogram with the phase factor of Eq. 3.5, the corresponding RF comb is corrected at zero frequency for any phase fluctuations. RF comb lines at other frequencies are corrected only for fluctuations they have in common with the zero-frequency RF comb line. To correct remaining differential fluctuations, the sampling rate must be adjusted such that the samples are separated by equal intervals in  $\phi_{\text{diff}}(t)$ , given by

$$\phi_{\text{diff}}(t) = 2\pi \int f_1(t') - f_2(t') dt'. \quad (3.6)$$

Note that the already corrected line at zero frequency is unaffected by changes to the sampling rate (since its frequency is zero). Using this scheme, when  $f_1(t) - f_2(t)$  increases, the time between samples becomes smaller, and in terms of the adjusted sampling intervals, the frequency difference  $f_1 - f_2$  remains constant (and hence free of any fluctuations). While, in other experiments, the sampling rate is adjusted by changing the clock rate of the AD converter [58],

here, the sampling rate is adjusted by calculating  $\phi_{\text{diff}}$  for each sample and interpolating the signal at points regularly spaced in  $\phi_{\text{diff}}$ . The two approaches are completely analogous in that they lead to the same corrected interferogram. For any adjustment of the sampling time interval by  $\delta t$ , the corresponding phase adjustment  $\delta\phi$  of an oscillation at frequency  $f$  is given by  $\delta\phi = 2\pi f\delta t$ . Because  $\delta\phi$  scales with  $f$ , in this step, all phase fluctuations are corrected that scale linearly with the RF-comb-mode number. In particular, as already noted, this step has no impact for  $f = 0$ . In other words, calculation of  $\phi_{\text{cm}}(t)$  allows to correct for fluctuations of  $\Delta f_{\text{ce}}$ , while calculating  $\phi_{\text{diff}}(t)$  allows to correct for fluctuations of  $\Delta f_{\text{rep}}$ . Obviously, fluctuations that scale nonlinearly with the comb-mode number cannot be corrected with this scheme.

This correction scheme only applies directly to linear spectra measured with the 192-THz fundamental spectrum: During the SHG process to produce 383-THz light, the frequencies of the RF comb lines (and any fluctuations of the frequencies) are effectively multiplied by a factor of 2, and during the conversion from the one-photon comb to the two-photon comb, by another factor of 2. To use the recorded error signals to correct the one- and two-photon spectra, the measured time-domain signal should instead be multiplied by a modified phase factor  $e^{-i\phi_{\text{cm}}^{(k)}(t)}$ , where

$$\phi_{\text{cm}}^{(k)}(t) = 2\pi \int \alpha' f_1(t') + (k - \alpha') f_2(t') dt', \quad (3.7)$$

$k$  is the net number of photons from the initial comb absorbed in the transition, and  $\alpha' = k\alpha$  is an arbitrary real number. For the one-photon transitions measured here near 385 THz,  $k = 2$ , and for the two-photon transitions driven by two 385-THz photons,  $k = 4$ . (If the scheme were used to study a coherent Raman process,  $k$  would be zero, since the number of photons absorbed is equal to the number of photons emitted; in this case,  $\phi_{\text{cm}}^{(0)}(t)$  could be set to zero, and only a correction to the repetition rate would be necessary.) Because one-photon transitions and two-photon transitions are corrected with different values of  $k$ , the order of each spectral feature can be uniquely identified, assuming the initial interferogram is sufficiently distorted.

## 3.4 Results and Discussion

To demonstrate the technique's capability to acquire high-resolution, broadband linear and two-photon spectra, a heated cell filled with  $^{85}\text{Rb}$  and  $^{87}\text{Rb}$  in its natural abundance is probed. When exciting Rb into the  $5D$  states by means of a dual-comb spectrometer, all resonance frequencies that lie within the combs' spectral overlap region are modulated onto the fluorescence intensity.

Figure 3.7 shows a time trace of dual-comb induced  $6P$ - $5S$  fluorescence corrected for relative-phase errors. The contribution of the two-photon transitions to the intensity time trace is also shown. The interferogram exhibits modulations on all timescales and fringes are clearly visible over the full range of the recording. The origin of this modulation is better explored in the frequency domain. Figures 3.8 and 3.9 show the spectral magnitudes resulting from Fourier transformation of the acquired time-domain interferograms.

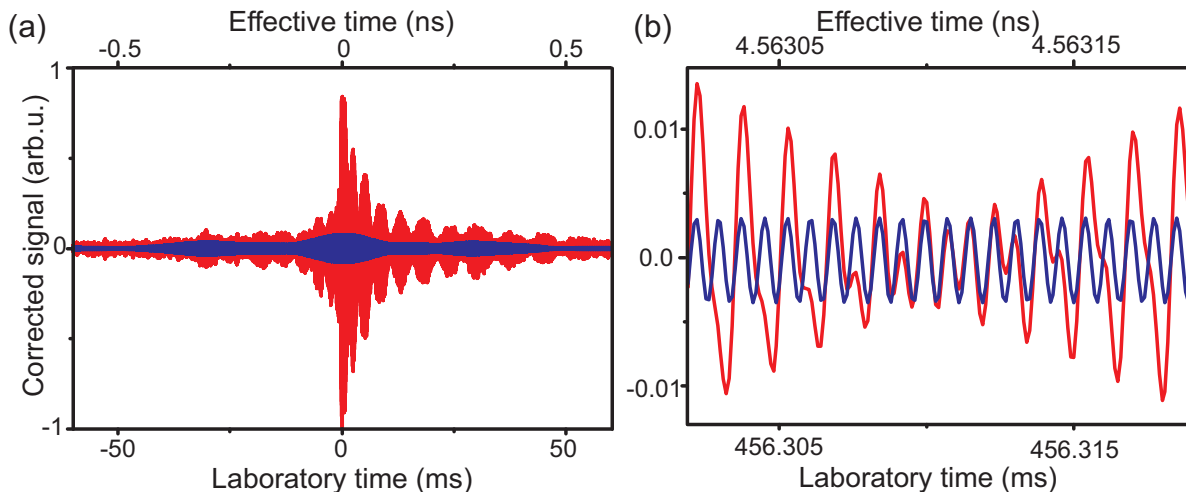


Figure 3.7: Two portions of an unaveraged, corrected interferogram recorded at  $T = 393$  K with  $\Delta f_{\text{rep}} = 1$  Hz (red) and contributions to that interferogram from two-photon transitions (blue). Two time scales are displayed. The laboratory time is the actual measurement time which accounts for the down-sampling nature of the technique. The effective time is the time delay in a pair of pulses, one from each comb.

The full relevant spectral range spans over four frequency segments in Fig. 3.8. These, respectively, show the  $5S_{1/2}$ - $5P_{3/2}$  transitions with the resolved hyperfine ground-state splitting (low-frequency segment), the  $5P_{3/2}$ - $5D_{3/2}$  transitions (low-frequency central segment), the  $5P_{3/2}$ - $5D_{5/2}$  transitions (high-frequency central segment), and the  $5S_{1/2}$ - $5D_{5/2}$  transitions with an again clearly visible hyperfine ground-state splitting (high-frequency segment). All fluorescence-derived spectra were calibrated using the measured repetition rates and one of the resonance lines. For the spectrum recorded at 308 K shown in Fig. 3.8 that line was the  $^{85}\text{Rb}$   $5S_{1/2}, F_g=2$ - $5P_{3/2}$  transition at 384.2321237 THz. For both other two-photon spectra (solid orange and cyan) shown in Fig. 3.9 recorded at  $T = 393$  K, that line was the  $^{85}\text{Rb}$   $5S_{1/2}, F_g=2$ - $5D_{5/2}$  transition at 770.5732553 THz. Line-position parameters are taken from Refs. [59, 60, 61]. At high instrumental resolution (orange trace), the excitation spectrum is found to be composed of individual comb lines, showing that the coherence between the two mode-locked lasers is maintained for the duration of the 54-second measurement. To my

knowledge, this is the first demonstration of both, dual-comb-based two-photon spectroscopy and fluorescence-based dual-comb spectroscopy.

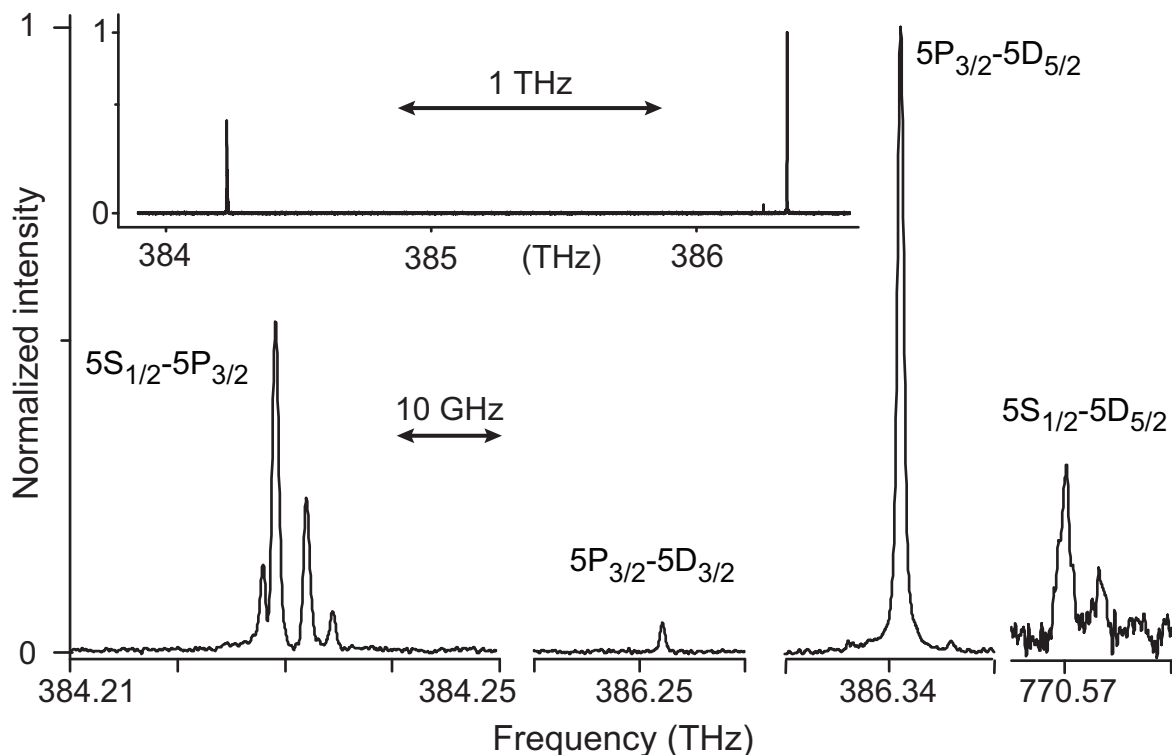


Figure 3.8: Portions of the one- and two-photon excitation spectra of Rb. The full range of the one-photon excitation lines is shown in the top inset, while the main part zooms into the individual one- and two-photon transitions (tick increment: 10 GHz). The spectrum, displayed at an unapodized resolution of 300 MHz, is recorded at  $T = 308$  K within 18-s measurement time.

Since the shown spectra are normalized to 1, the signal-to-noise ratio can sensibly be defined as  $1/\sigma$ , where  $\sigma$  is the standard deviation of the spectral data measured in a region without noticeable signals. The resulting SNR values are 546 for the spectrum shown in Fig. 3.8, 102 for the cyan spectrum shown in Fig. 3.9, and 40 for the orange spectrum of the same figure. The measurements are correctly reproduced by theoretical calculations that incorporate all allowed hyperfine transitions and assume Gaussian lineshapes. The natural linewidths of  $\lesssim 6$  MHz [62, 50] are small compared to the Doppler broadening (FWHM) of 523 MHz (one-photon-transition lines,  $T = 308$  K) and 1.18 GHz (two-photon-transition lines,  $T = 393$  K). The experimental widths are 644 MHz ( $5S_{1/2}, F_g=2-5P_{3/2}$ ), 702 MHz ( $5P_{3/2}-5D_{5/2}$ ), and 876 MHz ( $5S_{1/2}, F_g=2-5D_{5/2}$ ) for the highest-intensity unblended lines. The origin of the deviations between these values and the Doppler widths is yet to be explored.

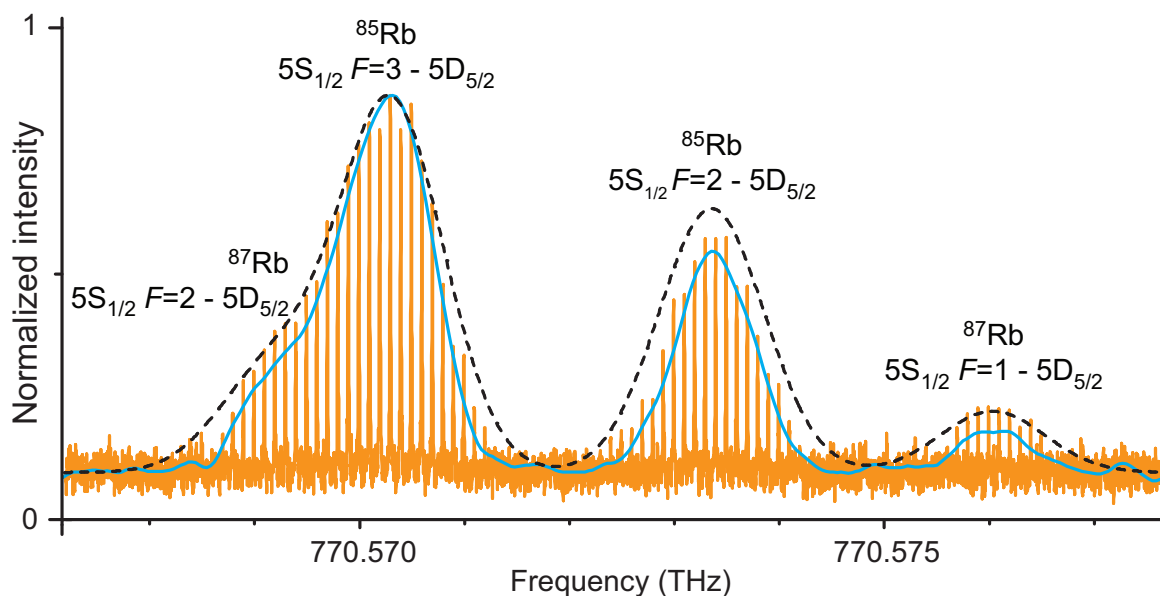


Figure 3.9: Experimentally recorded Doppler-limited DC2pES spectrum: the  $5S_{1/2} - 5D_{5/2}$  transitions. The spectrum is recorded at a cell temperature of  $T = 393$  K (solid cyan: 18-s measurement time, unapodized resolution of 300 MHz; solid orange: 54-s measurement time, unapodized transform-limited comb-line linewidth of 4.4 MHz; dashed black: computed).

Simultaneously to the fluorescence interferogram, the linear-absorption interferogram can be acquired. A portion of the resulting spectrum (at 308 K) is shown in Fig. 3.10. This adds an additional diagnostic tool to the technique, which might prove useful if the sample is not spectroscopically well known.

The above two-photon spectra cannot be measured with the traditional direct frequency-comb spectroscopy technique [63, 64], where only a single comb is scanned through the excitation profiles of the sample. In this type of direct frequency-comb spectroscopy, any transition frequency can only be measured modulo the line spacing of the frequency comb. When scanning a single frequency comb through profiles much broader than its mode spacing, any change in excitation probability due to the frequency shift of one resonant comb line can be offset by the change in excitation probability due to the frequency shift of another, also resonant comb line. The result is an almost uniform intensity distribution across the entire scan-frequency range [64, 65]. As already noted by its pioneer developers [66], the traditional technique is only suitable for very simple spectra with sharp transitions and is not appropriate for broad and crowded spectra or for transitions with a linewidth broader than the comb-line spacing, as often encountered with Doppler-broadened profiles.

When compared to CW-laser-based two-photon spectroscopy, DC2pES has the multiplexing



advantage of improved consistency of spectral data: Measured spectra can be well-interpreted as the sample's excitation spectrum averaged over the recording's measurement time. Any transient process, e.g. temperature-fluctuation-induced vapor-pressure fluctuations, chemical reactions, or nuclear decay, occurring on time-scales shorter than the measurement time can impact all frequencies covered by the comb. In contrast, when using a CW laser, any transient process occurring after the frequency scan is initiated will only effect subsequent scan frequencies, potentially resulting in spectra that are difficult to interpret.

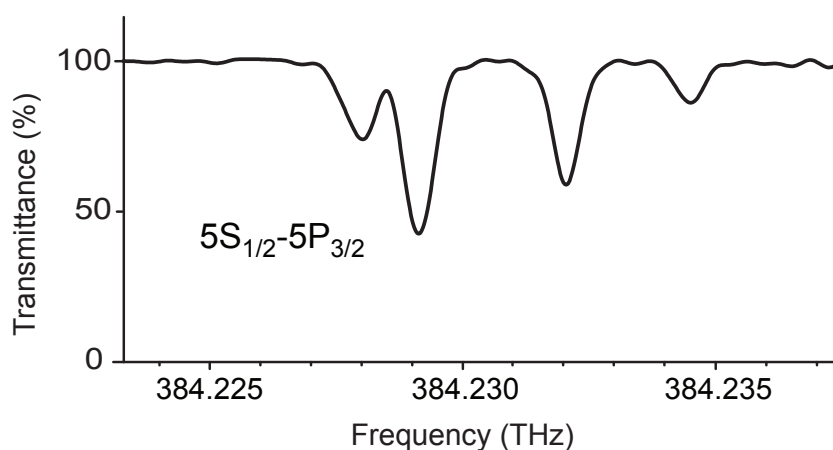


Figure 3.10: Portion of the absorption dual-comb spectrum of Rb at  $T = 308$  K and 300 MHz unapodized resolution.

The above proof-of-principle demonstration shows the potential of dual-comb spectroscopy for the measurement of broad-spectral-bandwidth Doppler-limited two-photon excitation spectra. The technique applies to any sample that fluoresces under two-photon excitation and could be extended to higher-order multiphoton excitation and ionization detection. It permits highly multiplexed measurements since all one- and two-photon transitions within the excitation bandwidth of the femtosecond lasers are simultaneously observed within a short measurement time. Background-free fluorescence detection allows for higher sensitivity than absorption measurements. The experiments presented in this chapter pave the way for the application of DC2pES to spatially selective real-time spectroscopy of liquid samples (see Chap. 5). Moreover, if the two laser combs both counterpropagate in the sample, the technique can be extended to sub-Doppler resolution and hence to the field of precision spectroscopy. As is shown in the following chapter, Doppler-free spectroscopy of highly crowded molecular spectra becomes feasible.



# 4 Sub-Doppler Dual-Comb Two-Photon Spectroscopy

Under some “real world” experimental conditions, e.g. high-altitude atmospheric conditions [67, Chap. 1], Doppler-broadening is the dominant broadening mechanism for atomic and molecular gases. Elimination of this broadening mechanism can drastically reduce the width of spectroscopic lines and correspondingly facilitate discrimination of separate species or precise frequency determination. This is particularly true for molecules, which have the additional internal degrees of freedom of vibration and rotation, leading to a forest of narrow closely spaced lines spanning over 10s to 100s of GHz [68, 69], that can only be resolved when Doppler-broadening is absent. Moreover, since electronic states can also be closely spaced in molecules [70], a literal smorgasbord of transition lines spanning over many THz can be expected. To demonstrate the potential of DC2pES to be extended and applied to Doppler-free spectroscopy, rubidium in its natural abundance is chosen as the sample.

The choice of rubidium is motivated by its strong, closely-spaced two-photon transitions at an experimentally easy-to-access wavelength of around 778 nm. The frequency-spacing between the lines covers all scales from 3 MHz to 100 GHz at a natural linewidth of 667 kHz [50], enabling a precise experimental quantification of the resolution of the Doppler-free DC2pES setup. The setup’s accuracy can likewise be assessed since the relevant absolute transition frequencies are known to an uncertainty of better than 52 kHz<sup>1</sup> [61].

One of the standard methods to cancel the Doppler-effect is the standing-wave two-photon excitation technique, where the sample is simultaneously irradiated by a laser beam and another counter-propagating laser beam. The mathematical basis for this conceptually simple experimental scheme is explored in the following section. The same section also provides a detailed overview of Rb’s energy levels, in particular the hyperfine states of the  $5D$  manifold.

---

<sup>1</sup>The  $5S_{1/2}$ - $5D_{5/2}$  transition has been suggested by the International Committee for Weights and Measures as an optical frequency standard to realize the unit of length [71].

The experimental setup is discussed thereafter in Sec. 4.2. Both, electronic and optical hardware components are introduced here. It also details on how the optical frequency axis for DC2pES spectral data is determined. This provides a sound basis to understand how the spectral data shown in Sec. 4.3 is measured and calibrated. Statistical and systematic error sources are discussed in Sec. 4.4, also providing a comparison with high-precision data from the literature.

## 4.1 Background

### 4.1.1 General Principle of Doppler-Free Spectroscopy

The distribution of velocities  $v$  of low-pressure-gas particles of mass  $m$  is generally well-approximated by the Maxwell-Boltzmann distribution

$$f_{\text{MB}}(v) = 4\pi \left( \frac{m}{2\pi k_{\text{B}} T} \right)^{\frac{3}{2}} v^2 \exp\left(-\frac{mv^2}{2k_{\text{B}} T}\right), \quad (4.1)$$

where  $k_{\text{B}}$  denotes the Boltzmann constant and  $T$  is the absolute temperature in units of Kelvin. The resulting Gaussian distribution of kinetic energies causes the distribution of apparent transition frequencies, commonly referred to as the Doppler distribution, to be also Gaussian. The effect of the velocities of the absorbers on resonance terms can be accounted for by replacing the excitation light's emitter-rest-frame frequency  $\omega$  by the frequency as observed in the frame of the absorber  $\omega + \mathbf{k} \cdot \mathbf{v}$  (Galilean transformation). Here,  $\mathbf{k}$  denotes the photon's wave vector and  $\mathbf{v}$  denotes the particle's velocity vector. The probability for excitation of a transition from the lower state  $o$  to the upper state  $t$  via two-photon absorption is proportional to (compare Eq. 2.10)

$$\text{Im}\left(\chi^{(3)}(-\omega_1; -\omega_2, \omega_1, \omega_2)\right) \propto \frac{\Gamma}{(\omega_{to} - (\omega_1 + \omega_2) + (\mathbf{k}_1 + \mathbf{k}_2) \cdot \mathbf{v})^2 + \Gamma^2}, \quad (4.2)$$

where  $\mathbf{k}_1$  and  $\mathbf{k}_2$  ( $\omega_1$  and  $\omega_2$ ) are the wave vectors (angular frequencies) of the first and second absorbed photon, respectively, and  $\Gamma$  is the relaxation rate of state  $t$ . Assume now that two collinear counter-propagating beams are used and that the absorber has a positive velocity

component  $v_{\parallel}$  along the propagation direction of Beam 1. Equation 4.2 then becomes

$$\text{Im}\left(\chi^{(3)}(-\omega_1; -\omega_2, \omega_1, \omega_2)\right) \propto \frac{\Gamma}{(\omega_{i0} - (\omega_1 + \omega_2) - ((\omega_1 + \omega_2)v_{\parallel}/c))^2 + \Gamma^2}, \quad (4.3)$$

for the (red-shifted) absorption of two photons from Beam 1,

$$\text{Im}\left(\chi^{(3)}(-\omega_1; -\omega_2, \omega_1, \omega_2)\right) \propto \frac{\Gamma}{(\omega_{i0} - (\omega_1 + \omega_2) + ((\omega_1 + \omega_2)v_{\parallel}/c))^2 + \Gamma^2}, \quad (4.4)$$

for the (blue-shifted) absorption of two photons from Beam 2, and

$$\text{Im}\left(\chi^{(3)}(-\omega_1; -\omega_2, \omega_1, \omega_2)\right) \propto \frac{\Gamma}{(\omega_{i0} - (\omega_1 + \omega_2) + (\Delta\omega v_{\parallel}/c))^2 + \Gamma^2}, \quad (4.5)$$

with  $\Delta\omega = \omega_2 - \omega_1$ , for the absorption of one photon from each beam. A comparison of Eq. 4.5 with the two preceding equations directly reveals that the Doppler-broadening reduces by a factor of  $\Delta\omega/\omega_{i0}$  for excitation by counter-propagating beams. The presence of an intermediate state within the excitation bandwidth of the laser source strongly enhances the two-photon excitation by those laser modes that are in resonance with the intermediate state. For the  $5S_{1/2}$ - $5P_{3/2}$ - $5D_{5/2}$  transition in Rb that is relevant here,  $\Delta\omega/(2\pi)$  amounts to 2.1 THz, corresponding to a Doppler-broadening reduction by a factor of 365 to 2.9 MHz (in ordinary frequencies). Without the excitation of an intermediate state in the two-photon-absorption process,  $\Delta\omega$  and therefore the Doppler-reduction is determined by the spectral width of the excitation source.

Doppler-free two-photon absorption spectroscopy was first suggested by Vasilenko et al. in 1970 [72], followed by experimental demonstrations in 1974 [73, 74, 75]. The combination of this method with a frequency comb excitation source was demonstrated in 1977 by Teets et al. [76]. Subsequently, numerous groups made use of Doppler-free direct comb spectroscopy [77], mainly for high-precision metrological applications. However, it was already realized by its pioneer developers that ‘‘Of course this technique will be useful only for sufficiently simple spectra,’’ [66] and this intrinsic restriction of the technique’s inability to identify the comb line responsible for the excitation has not yet been overcome. The remainder of this chapter is dedicated to the description of an experimental demonstration where this is finally achieved.

### 4.1.2 Hyperfine Energy Levels of Rubidium

The left panel of Fig. 4.1 shows the general excitation/decay paths experimentally exploited in this chapter. As in Chap. 3, Rb is excited via dual-comb excitation into its  $5D$  manifold, a two-photon transition that is enhanced by the presence of the  $5P_{3/2}$  states near the halfway point of the two-photon transition. The cascaded  $5D$ - $6P$ - $5S$  fluorescence decay channel is used as a probe of the  $5D$  excitation probability.

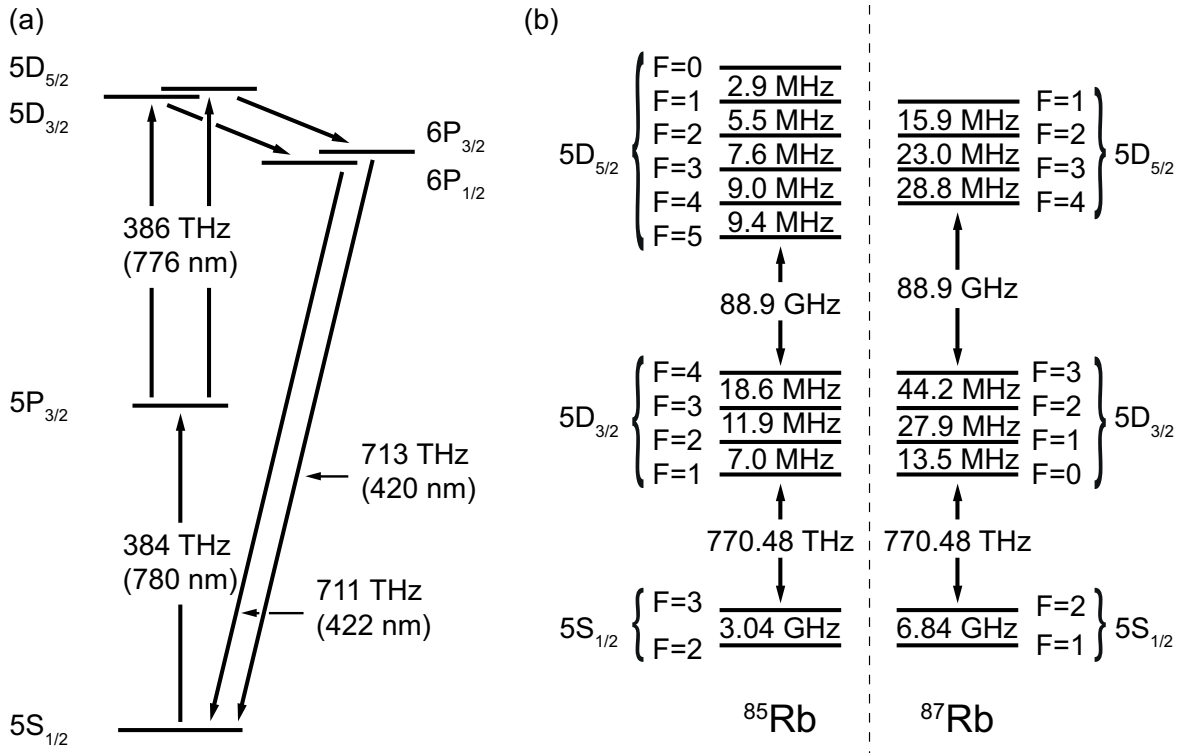


Figure 4.1: Experimentally relevant fine structure of rubidium (Panel (a)) and hyperfine structure of the  $5S$  and  $5D$  states of  $^{85}\text{Rb}$  and  $^{87}\text{Rb}$  (Panel (b)).

Taken together, the two naturally occurring Rb isotopes  $^{85}\text{Rb}$ , with a nuclear spin quantum number  $I = 5/2$  and  $^{87}\text{Rb}$ , with  $I = 3/2$ , have a total of 33 allowed two-photon transitions ( $5S$  to  $5D$ ) around 778 nm. The hyperfine  $5D$  states of  $^{85}\text{Rb}$  are split by 2.9–18.6 MHz, while the hyperfine splittings of the  $5D$  states of  $^{87}\text{Rb}$  have larger splittings of 15.9–44.2 MHz, owing to the larger nuclear spin of this isotope. All relevant hyperfine states are plotted in Panel (b) of Fig. 4.1.

## 4.2 Experimental Setup

This section is structured in the following way: Sec. 4.2.1 provides a broad, but rather undetailed overview over the experimental setup used. Detailed descriptions of the various aspects of the setup are provided subsequently. Section 4.2.2 provides a detailed account on the beams' polarizations. Sec. 4.2.3 details on the phase-stabilization aspects of all used lasers. The implemented laser-stabilization scheme cannot fully avoid phase-fluctuations, and an *a posteriori* phase-correction scheme is implemented to correct any remaining phase-distortions. The generation of these (two) phase-correction signals is also described in Sec. 4.2.3. Their utilization is then detailed in Sec. 4.2.4. Both of the two correction signals are derived from separately beating each of the two combs used for sample excitation with two CW lasers. These two CW lasers simultaneously serve as anchor points for the optical-frequency calibration of the excitation spectra. Sec. 4.2.4 therefore also details on the calibration of the acquired excitation spectra. Finally, Sec. 4.2.5 describes how multiple optical-frequency-calibrated excitation spectra can be combined into a single excitation spectrum with a much higher resolution. This combination procedure is introduced in Sec. 2.4 and commonly referred to as interleaving. It is made necessary because the line-widths of the probed Doppler-free transitions are expected to be much smaller than the combs' mode spacings.

### 4.2.1 Setup Overview

An overview of the experimental setup is given in Fig. 4.2. On the right side of the figure, it is shown that the outputs of two Er comb generators (Menlo Systems, C-Comb + P100) are frequency doubled using a MgO:PPLN crystal (Covesion, MSHG1550), yielding  $\sim 10$ -THz-wide spectra centered around  $\sim 383$  THz at power levels of up to 160 mW per comb when the SHG is optimized to maximal power output. The two beams are then combined before entering an anti-resonant ring containing the vapor-phase-rubidium cell heated to 323 K. The cell is placed into the center of three Helmholtz coils on mutually perpendicular axes used to cancel the Earth's and any stray magnetic fields. The two counter-propagating beams are focused at the same position of the cell with two  $f = 150$  mm lenses. The two-photon excitation induced fluorescence is collected in sideways geometry with a photomultiplier tube (PMT). The time-domain interference pattern originating from the dual-comb excitation is recorded on a fast 14-bit digitizer (AlazarTech, ATS9440).

All the excitation spectra shown in this chapter have been recorded with average laser powers measured right before the focusing lenses of  $P_{\text{Comb 1,l}} = 2.6$  mW,  $P_{\text{Comb 2,l}} = 10.2$  mW,  $P_{\text{Comb 1,r}} = 2.5$  mW,  $P_{\text{Comb 2,r}} = 9.4$  mW. Here, the labels “l” (“r”) refer to the beams reaching the cell from the top left (bottom right) in Fig. 4.2. The unbalance in the given power levels between the two combs is a direct consequence of optimizing the SHG for maximum fluorescence yield, e.g. by adjusting the crystal temperature, rather than maximizing or balancing the power outputs.

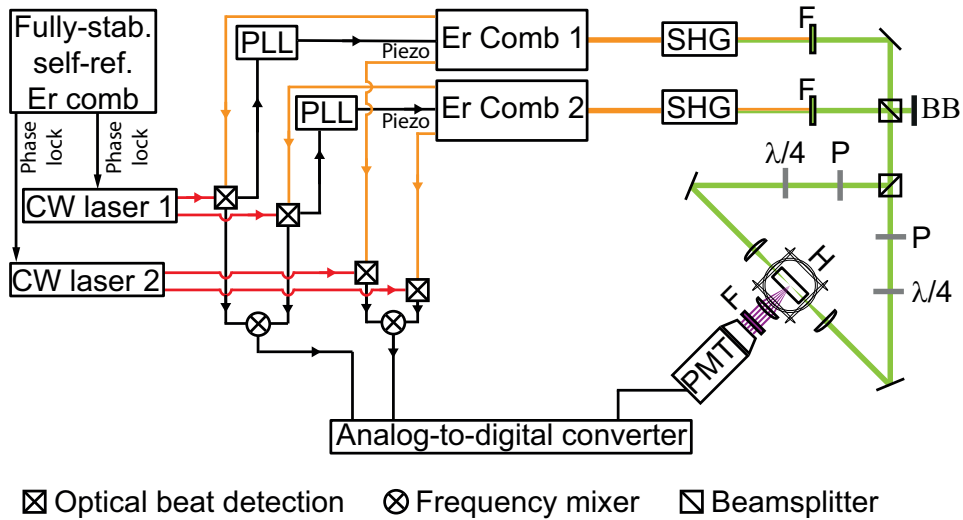


Figure 4.2: Experimental setup for Doppler-free DC2pES of gas-phase rubidium. The beat-detection part and the stabilization scheme outlined on the left of this figure is described in more detail in Fig. 4.3. SHG, second-harmonic generation; F, optical filter; BB, beam block; P, polarizer;  $\lambda/4$ ,  $\lambda/4$  wave plate; PMT, photomultiplier tube; H, Helmholtz coils.

The left side of the figure shows how the two excitation-source combs are stabilized and how signals used to correct their relative-phase fluctuations are generated. A third, self referenced, Er frequency comb, in the following referred to as the “metrology comb”, is used to define a common optical frequency scale for the two excitation combs. The latter two combs are stabilized and referenced against the metrology comb via two intermediate CW lasers transferring the metrology comb’s stability to the excitation combs. Simultaneously, each of the two CW lasers serves to effectively isolate the beat note between the longitudinal mode of Comb 1 and the longitudinal mode of Comb 2 closest in frequency to the CW laser. These two isolated inter-comb beat notes contain relative-phase fluctuations that can be extracted and used in a post-correction scheme to phase-correct the dual-comb interferogram as recorded by the PMT. Care is taken to ensure equal electronic delays between the two correction-signal channels and the PMT channel by measuring the respective signal delay and adding appropriate electronic delay lines.



### 4.2.2 Polarization of the Excitation Beams

The polarizations of the two counter-propagating beams, both carrying the pulse trains of Comb 1 and Comb 2, were both adjusted to be circular (equal polarization spin projection) for maximal fluorescence yield [78]. This adjustment was carried out by insertion of a Glan-Thompson polarizer (B. Halle) followed by a broadband (500–900 nm)  $\lambda/4$  wave plate (B. Halle) into each of the two outputs of the second beam splitter. The only role of the polarizers, with extinction ratios specified as  $10^{-8}$ , is to further increase the polarization extinction ratio of the already linearly polarized incoming beams. The angle of each  $\lambda/4$  wave plate is determined coarsely by surrounding it with two cross-polarized polarizers and tuning the wave plate angle to yield maximal output power after the second, additional polarizer. The angle was then fine tuned to equalize this output when the second polarizer is cross polarized and when it is parallel polarized with respect to the first polarizer. The measured difference in power levels between these two rotation positions was about 2% of the total measured power. The added polarizer after the  $\lambda/4$  wave plate was then removed from the setup before performing the DC2pES measurements. When tuning one or both of the so-adjusted  $\lambda/4$  wave plates in the DC2pES measurements, the fluorescence yield could only be lowered, thus showing that the maximum-fluorescence-yield state is indeed found with the described polarization-control scheme.

### 4.2.3 Frequency-Comb Stabilization and Phase-Correction-Signal Generation

Figure 4.3 provides a detailed description of the hardware part of the stabilization and correction scheme. The metrology comb and all electronic components used for its stabilization are purchased from Menlo Systems (FC1500-250-WG). The comb's frequency offset is measured by the  $f-2f$  technique and directly stabilized to an active hydrogen maser at a frequency of 20 MHz via feedback onto the pump-diode current. The comb's repetition rate is effectively stabilized by beating the comb with an external-cavity-stabilized narrow-linewidth CW laser [79] and locking the beat frequency to a 20 MHz reference signal (H-maser) via feedback on a piezoelectric transducer mounting one of the comb's laser-cavity mirrors. The stability, in terms of the Allan deviation of the two comb parameters  $f_{\text{rep}}$  and  $f_{\text{ce}}$ , was measured by a frequency counter with an observation time set to 1 s, resulting in values ranging from 3 to 9 mHz and from 0.7 to 1.7 Hz, respectively.

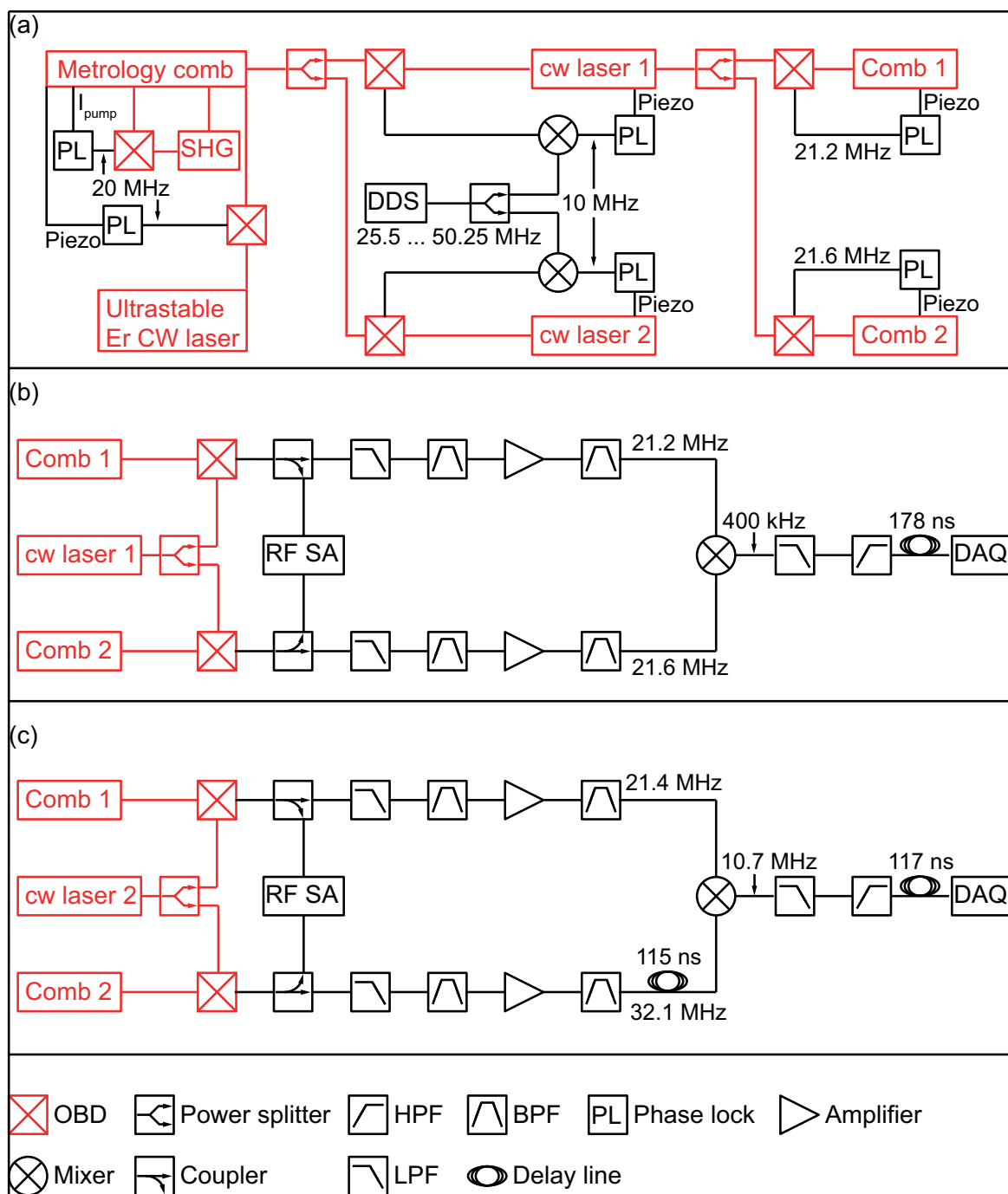


Figure 4.3: Frequency comb stabilization and phase-correction-signal generation. Primarily optical components are drawn in red, electrical components are drawn in black. OBD, optical beat detection; HPF, high-pass filter; LPF, low-pass filter; BPF, band-pass filter; RF SA, radio-frequency spectrum analyzer; DAQ, data acquisition; the PL instrumentation encompasses a loop filter, a phase comparator, a signal generator, and possibly filters to reduce noise on the beat notes (compare Fig. 3.5 Panel (c)).

Two CW lasers (NKT Photonics, Koheras ADJUSTIK), one lasing at 192 THz (1557 nm), the other lasing at 195 THz (1534 nm), are both stabilized to the metrology comb. This is done by separately beating them with the comb, mixing the respective beat signal with the output of a home-built RF-frequency direct digital synthesizer (DDS), and locking the mixing product to the H-maser's 10 MHz output. The lock is implemented by feeding back a voltage proportional to the phase difference between the mixing product and the H-maser's output to a piezoelectric transducer serving as a mount for one of the respective CW laser's internal cavity mirrors. Making use of the mixing process is necessary because of the limited bandwidth of the phase comparator used in all laser-stabilization PLLs. The 20th harmonic of the H-maser output at 10 MHz is used as the reference oscillator for the DDS. The DDS output frequency  $f_{\text{DDS}}$  can be phase-coherently varied over a broad frequency range, in particular covering the range 26.5–51.25 MHz.

The 195 THz CW laser is separately beaten against both of the two combs used for two-photon excitation of Rb. The two beat notes are then mixed to produce one of the two phase-correction signals. The second phase-correction signal is produced in the same way using the 192 THz CW laser. In addition to this correction-signal generation, this CW laser is also used to stabilize the two excitation combs. The beat note with Comb 1 (Comb 2) is stabilized to the 21.2 MHz (21.6 MHz) output of a PLL RF synthesizer (SRS, DS345) via feedback on a piezoelectric transducer mounting one of the combs' laser-cavity mirrors. Consequently, the correction signal derived from the 192 THz CW laser is centered around 400 kHz. As only one of the two comb-degrees-of-freedom is stabilized, the correction signal derived from the 195 THz CW laser is not centered around a fixed frequency. Experimentally, however, it is found that the fiber comb's inherent relative stability is high enough to restrict frequency drifts of the latter correction signal to less than 100 kHz even over the course of hours.

#### **4.2.4 Computation of a Single Interleaving-Step Spectrum**

The two following sections describe how a single interleaving-step spectrum is computed. In a first step, described in Sec. 4.2.4.1, the intensity of the RF beat notes is determined. If phase distortions of the excitation combs' comb lines were negligible on the scale of the repetition-rate difference, this step would only consist of Fourier transformation of the digitized PMT voltage output. However, with the optical frequency combs and the associate stabilization scheme used here, no comb structure can be identified in the Fourier transform of the fluorescence signal. Section 4.2.4.1 therefore is mainly concerned with the application of the post-correction

scheme, i.e. the utilization of the signals generated with the scheme described in the preceding section Sec. 4.2.3. Section 4.2.4.2 thereafter details on how these intensity values are assigned to absolute optical frequencies.

### 4.2.4.1 Correction of Inter-Comb Phase Instabilities

The phase-correction scheme employed to cancel relative-phase fluctuations between the two excitation combs consists of two stages. The first stage is exactly the same as the scheme detailed in Sec. 3.2. The Fourier transforms of the two correction signals used in this stage are shown in Fig. 4.4. A carrier peak can be seen in the correction signal involving the 192 THz CW laser. Its width is measurement-time limited to 28 mHz. A comparably narrow, though much weaker, peak on top of a broad pedestal is also observable on the correction signal involving the 195 THz CW laser. Its width (FWHM) is  $\sim 500$  Hz. After the first stage of post correction, the linewidth after the measurement time is 3 Hz in the RF domain. This value of 3 Hz is independent of the down conversion factor  $\eta$  (it does not change when  $\Delta f_{\text{rep}}$  is changed). The origin of this lower limit on the RF-domain linewidth is currently unclear. Some of this seems to be electronic, since harmonics of 50 Hz can be seen. Further candidates are differential acoustics pick-up by fibers, influence of the finite SNR on the correction signals, and influence of the finite coherence length of the intermediate CW lasers. In the second stage the interferogram is corrected using the phase extracted from the comb line of largest amplitude. Since it is the highest-amplitude comb line, the phase extracted from it has a higher SNR than phases that could be extracted from the other comb lines. As this correction is again carried out in the time-domain, affecting all comb modes in concert, all modes benefit from the high-SNR phase-noise cancellation. The linewidths after the second stage of post correction are measurement-time limited. These comb lines are the ones shown later in Fig. 4.6.

Post-correcting the spectrum fixes the effective RF position of the two comb-line pairs that contributed to the beat notes with the two CW lasers. Each comb is locked to a beat note with the 192-THz CW laser, with a line of Comb 1 21.2 MHz above the CW laser, and a line of Comb 2 21.6 MHz above the CW laser. In the post-correction scheme implemented here, this RF-comb line is defined to have a frequency of -400 kHz (or -1.6 MHz for the 4th harmonic used for the two-photon transitions). The beat notes against the 195-THz CW laser are not locked, but Comb 1 has a line about 32.11 MHz above the CW laser, and Comb 2 has a line roughly 21.37 MHz above the CW laser. This RF-comb line is fixed to +10.743047 MHz (or +42.97219 MHz on the 4th harmonic) to best match the average observed frequency over all

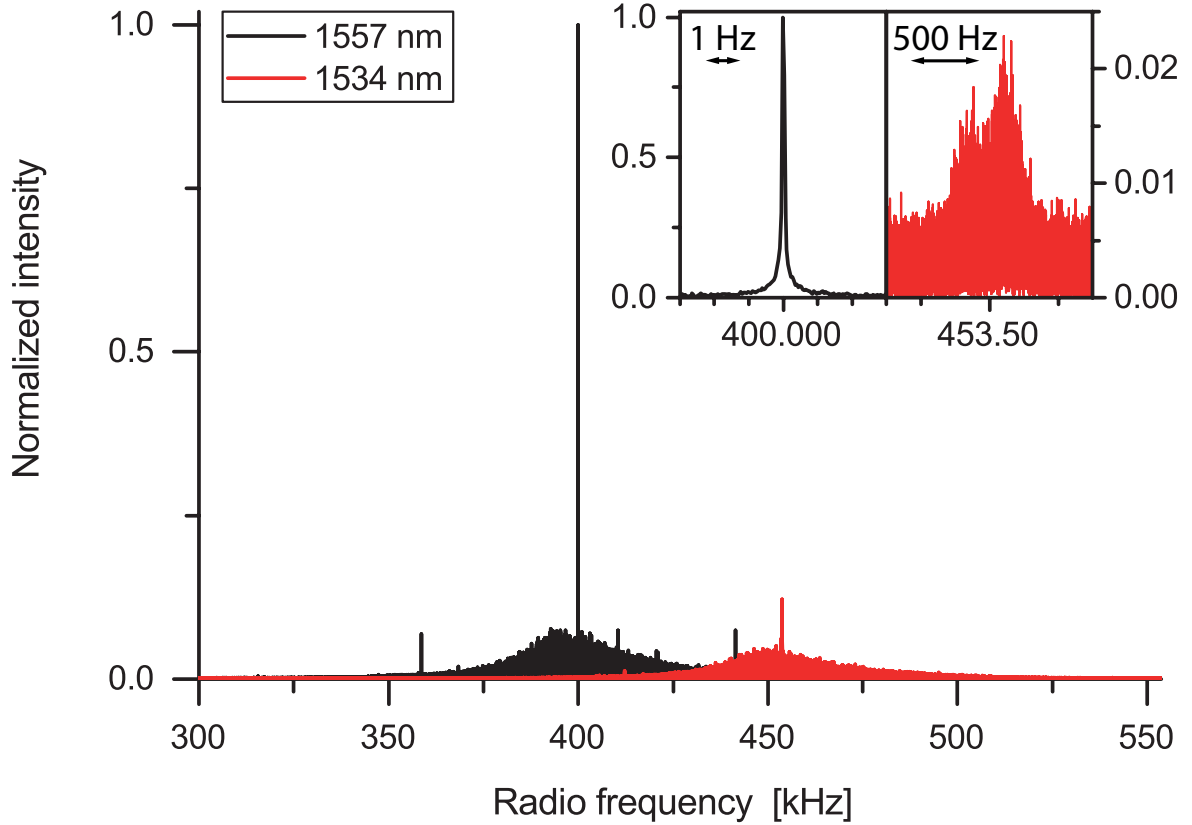


Figure 4.4: Fourier spectra of both phase-correction signals for the  $f_{\text{DDS}} = 30.75$  MHz interleaving-step measurement. The main panel shows the result of Fourier-transforming  $2^{21}$  unapodized sample points, corresponding to a point spacing of 0.89 Hz. The insets show the result of Fourier-transforming  $2^{26}$  unapodized sample points, corresponding to a point spacing of 28 mHz. The black traces are derived from beat notes of the combs with the 192 THz CW laser, whereas the red traces are derived from beat notes of the combs with the 195 THz CW laser. Note that the latter correction signal is aliased from 10.74 MHz to 453 kHz because of the Nyquist frequency of 933 kHz, corresponding to half the sampling rate of the digitizer card.

spectra. Note that relative positions of the comb lines and the sign of the RF-comb line changes between the two CW lasers, but this change is self-consistent. For all spectra in the interleaved data set, there are exactly 29101 mode spacings between the modes involved in the 192-THz beat note and the modes involved in the 195-THz beat note (or 116404 on the 4th harmonic). Knowing this enables the determination of the exact position of each RF-comb mode, which helps in finding the largest comb mode for the extra correction step described in the previous paragraph. Once the extra correction step is applied, the peak height of each RF-comb mode is extracted.

#### 4.2.4.2 Calibration of the Frequency Scale

At this point, the intensity of each RF-comb mode in the spectrum is determined and now needs to be correlated to the absolute optical position of the center of each comb-line pair. This can be done by determining the absolute position of one comb-line pair and using the average of the repetition rates of the two combs, which is the optical spacing between the modes, to determine the position of all other lines. Since Comb 1 is locked with a comb line 21.2 MHz above the 192-THz CW laser and Comb 2 is locked with a comb line 21.6 MHz above, the center of this comb-line pair is 21.4 MHz above this CW laser.

To determine and stabilize the position of the 192-THz laser, the fully-self-referenced metrology comb is used. The carrier-envelope offset frequency  $f_{ce}$  is stabilized to 20 MHz and mode number 777413 of the comb is stabilized 20 MHz above an ultrastable CW laser near 194 THz. Although this laser drifts slowly over time, the drift is measured to roughly equal 20 mHz/s and is thus negligible on the timescale of the measurement. During the DC2pES measurement, the repetition rate of the comb was 250 MHz + 53.579 Hz, and thus the frequency of the ultrastable CW laser was 194353291.653 MHz. The 192-THz CW laser is stabilized to comb mode number 770023 at a variable offset ranging from -41.25 MHz to -16.5 MHz. To accomplish this lock, the beat-note signal is mixed with the output of a direct digital synthesis (DDS) module generating a variable frequency from 26.5 MHz to 51.25 MHz. The beat-note signal is thus down-mixed to 10 MHz where it is filtered and stabilized against a constant-frequency reference. Using a DDS frequency synthesizer instead of a more traditional phase-locked-loop (PLL) synthesizer avoids phase jumps when changing the frequency. These jumps would normally cause the laser to lose lock.

Since the excitation combs are locked to the 192-THz laser, changing the position of this CW laser will also move these comb lines. To keep the beat notes between the excitation combs and the 195-THz laser roughly fixed as the frequency of 192-THz laser is adjusted, the 195-THz laser is stabilized using its beat note with the mode number 781663 of the self-referenced frequency comb. As with the 192-THz laser, the 195-THz laser is stabilized below the comb mode and at the same variable frequency offset.

The optical frequency of the 192-THz laser can now be written as:

$$f_{CW192} = 20 \text{ MHz} + 770023 \cdot 250.000053579 \text{ MHz} - (f_{\text{DDS}} - 10 \text{ MHz}) \quad (4.6)$$

$$= 192505821.257 \text{ MHz} - f_{\text{DDS}}, \quad (4.7)$$

where  $f_{\text{DDS}}$  is the output frequency of the DDS module. Eq. 4.7 associates the interleaving parameter directly controlled by the experimentalist,  $f_{\text{DDS}}$ , to the optical frequency  $f_{\text{CW192}}$  of the CW laser, which serves as the lock point for both excitation combs. The central position of the corresponding comb-line pair from the excitation combs is 21.4 MHz higher at 192505842.657 MHz -  $f_{\text{DDS}}$ . A formula for converting from the radio frequency  $f_{\text{RF}}$  to optical frequencies  $f_{\text{opt}}$  can now be written as:

$$f_{\text{opt}} = f_{\text{rep}} \cdot (f_{\text{RF}} - k(-0.4 \text{ MHz}))/((10.743047 \text{ MHz} - (-0.4 \text{ MHz}))/29101) \quad (4.8)$$

$$+ k * (192505842.657 \text{ MHz} - f_{\text{DDS}}). \quad (4.9)$$

Here,  $f_{\text{rep}} = (f_{\text{rep},1} + f_{\text{rep},2})/2$  and  $k$  is the transition order, i.e.  $k = 4$  for the two-photon transition. The expression

$$(f_{\text{RF}} - k(-0.4 \text{ MHz}))/((10.743047 \text{ MHz} - (-0.4 \text{ MHz}))/29101) \quad (4.10)$$

must be an integer for each comb line, corresponding to the number of mode spacings from the comb lines next to the 192-THz laser. The excitation combs repetition rates  $f_{\text{rep},1/2}$  were logged during the measurement. For the spectra shown in Sec. 4.3, the repetition rates at the beginning and the end of the scan range were

$$f_{\text{rep},1}(f_{\text{DDS}} = 26.5 \text{ MHz}) = 99996966.478 \text{ Hz}, \quad (4.11)$$

$$f_{\text{rep},2}(f_{\text{DDS}} = 26.5 \text{ MHz}) = 99996583.921 \text{ Hz}, \quad (4.12)$$

$$f_{\text{rep},1}(f_{\text{DDS}} = 51.5 \text{ MHz}) = 99996953.272 \text{ Hz}, \text{ and} \quad (4.13)$$

$$f_{\text{rep},2}(f_{\text{DDS}} = 51.5 \text{ MHz}) = 99996570.393 \text{ Hz}. \quad (4.14)$$

### 4.2.5 Stitching of the Interleaved Spectra

At this point, the absolute optical frequency and intensity of each comb line in the spectrum has been determined. Spectra are measured for 100 different values of  $f_{\text{DDS}}$  ranging from 26.5 MHz to 51.25 MHz at 0.25 MHz steps. To stitch these 100 spectra together, the tables of comb line intensity versus comb line optical frequency from each spectrum are concatenated and subsequently sorted using the optical frequencies. This results in a two-photon spectrum with a point spacing of approximately 1 MHz. The factor of 4 in difference between the two step sizes (0.25 MHz vs. 1 MHz) stems from the SHG (factor of 2) and the interrogation of two-photon transitions (factor of 2). Due to the slight change of repetition rate between

spectra, the frequency spacing between adjacent points is not perfectly uniform over the entire interleaved spectrum. Near the transitions to the  $5D_{5/2}$  state, most adjacent points are actually 1.001 MHz apart, and the points from the  $f_{\text{DDS}} = 26.5$  MHz interleaving-step spectrum are only 0.93 MHz from the points from the  $f_{\text{DDS}} = 51.25$  MHz interleaving-step spectrum.

### 4.3 Results

As described in the preceding sections, the scanning of both excitation combs is achieved by phase-continuously shifting  $f_{\text{DDS}}$ , which defines the lock point for both combs, in steps of 0.25 MHz, corresponding to steps of  $\sim 1$  MHz in terms of transition frequencies. Part of a phase-corrected time-domain interferogram corresponding to the randomly chosen  $f_{\text{DDS}} = 30.75$  MHz-step is shown in Fig. 4.5. It clearly shows pronounced interference fringes over the entire displayed time range. The full interferogram for each interleaving step consists of  $2^{26}$  samples recorded at a sampling rate of  $f_s = 1.866$  MS/s with a bit depth of 14 bit. Therefore, the total measurement time for each such interferogram is 36 s and the recording time for all 100 interleaving interferograms is 1 h. The data size of these 100 recordings and the simultaneously recorded two correction signals (parallel three-channel acquisition), amounts to 40 GB in binary format.

The result of the Fourier transform of the fully phase-corrected  $f_{\text{DDS}} = 34.0$  MHz-interferogram (i.e. the time-domain fluorescence trace recorded at the interleaving position  $f_{\text{DDS}} = 34.0$  MHz), zero-padded to  $2^{28}$  samples, is shown in the top panel of Fig. 4.6. The full figure illustrates how the individual spectra, one per interleaving step, are combined to produce interleaved spectra. It can be seen in Panel (a) that one of the comb lines is strongly enhanced over the others. Panel (b) shows a spectrum interleaved at 10 MHz steps on a 10 times smaller frequency scale. The green and the red trace correspond to the  $f_{\text{DDS}} = 31.5$  MHz,  $f_{\text{DDS}} = 29.0$  MHz interleaving-step measurement, respectively. Each of these two measurements exhibits comb lines that are stronger than the strongest displayed line of the measurement in Panel (a), i.e. these lines are closer to a two-photon resonance. The situation repeats when going to Panel (c), which shows a spectrum interleaved at 1 MHz. The profile of a sampled transition line is finally taking its shape as the interleaving steps are now fine enough to resolve it. The transition line is sampled in sufficiently fine steps to allow for a determination of its shape and the associated parameters such as its width and its center. While in going from Panel (a) to Panel (c) the zoom level is successively increased, Panel (d) has the same frequency scale as Panel (a). The shown



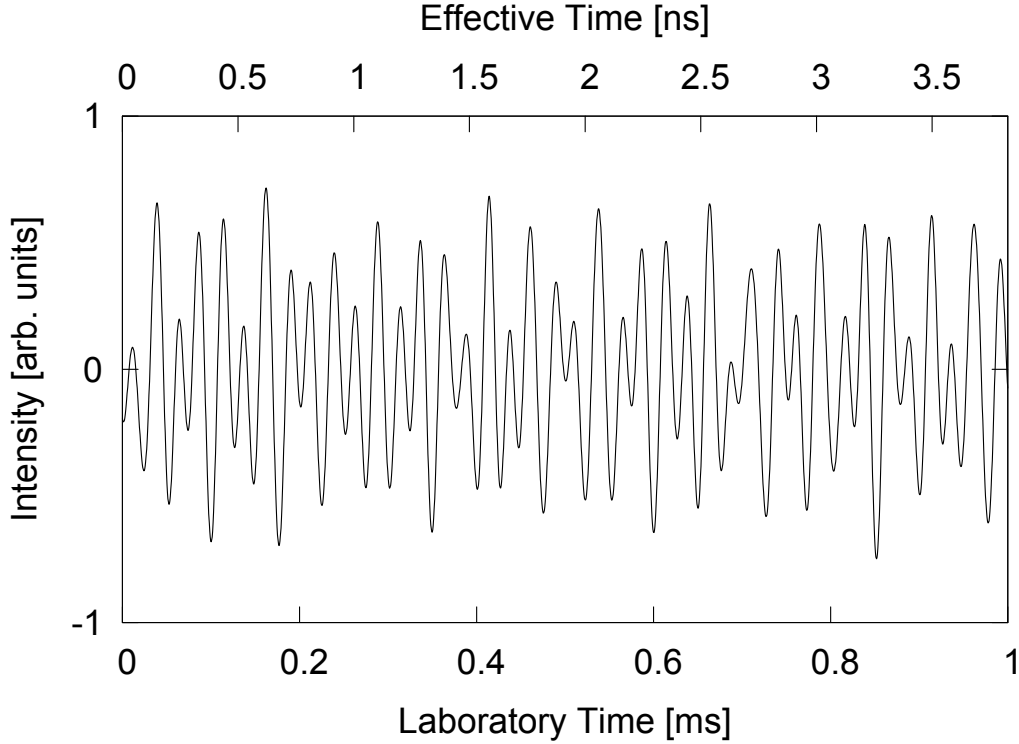


Figure 4.5: Measured, phase-corrected DC2pES time-domain fluorescence signal at excitation-comb positions given by  $f_{\text{DDS}} = 30.75$  MHz.

region contains the complete set of  $^{87}\text{Rb } 5S_{1/2}, F_g = 2-5D_{5/2}$  hyperfine transitions.

Taking advantage of the comb structure of the spectral data, the data size can be significantly reduced without any loss of relevant information in regards to the probed absorption profile by only keeping the maximum values of the comb lines and removing all other data points. This makes it possible to plot the spectrum shown in Fig. 4.7. The displayed spectral span amounts to 100 GHz and shows the  $5S_{1/2}-5D_{3/2}$  transitions at its low-frequency side (left) and the  $5S_{1/2}-5D_{5/2}$  transition at its high-frequency side (right).

Since the spectrum shown is normalized to 1, the SNR can sensibly be defined as  $1/\sigma$ , where  $\sigma$  is the standard deviation of the spectral data measured in a region without transition lines. The resulting SNR value is 11750. The excitation sources allow for probing a spectral span of  $\sim 10$  THz, however, all Rb resonances within this excitation bandwidth are located within a single spectral span of only 90 GHz. The repetition-rate difference  $\Delta f_{\text{rep}} = 383$  Hz was chosen here such that the experimental optical free spectral range of  $f_s/(2\eta) = 240$  GHz fully accommodates this 90 GHz span. Obviously, the experimental optical free spectral span could easily be adjusted to other experimental requirements by changing  $f_s$  or  $\eta = \Delta f_{\text{rep}}/f_{\text{rep}}$ . The

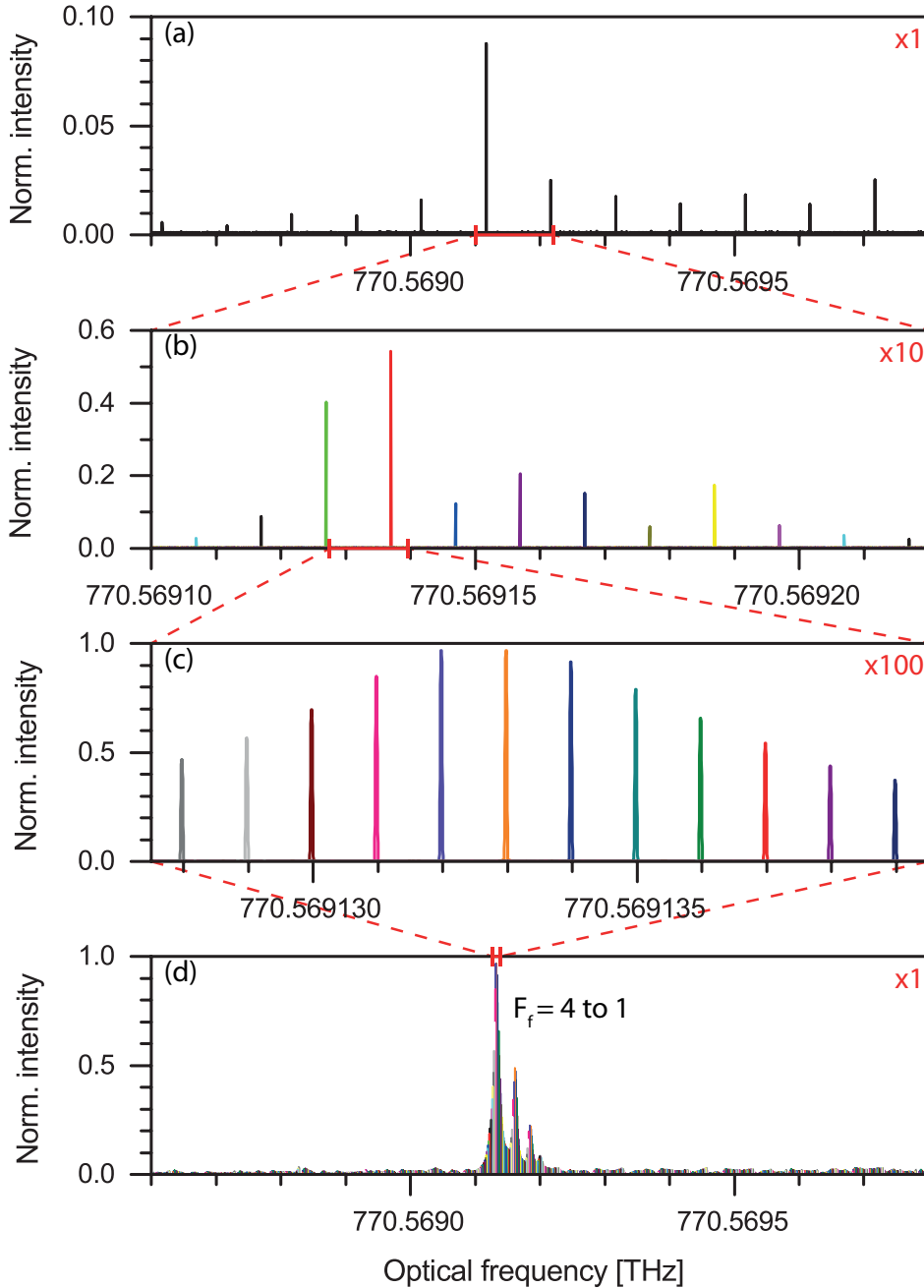


Figure 4.6: Illustration of the creation process of an interleaved spectrum. Panel (a) shows part of the Fourier spectrum of a single phase-corrected measured interferogram ( $f_{\text{DDS}} = 34.0$  MHz). The spacing between comb modes is 100 MHz. 10% of the frequency span (indicated by the red bar on the frequency scale) is expanded and shown in Panel (b). This panel now shows the Fourier spectra of ten phase-corrected measured interferograms spaced by ( $\Delta f_{\text{DDS}} = 2.5$  MHz), leading to a 10 MHz spacing between neighboring comb lines. 10% of the frequency span is again expanded and shown in Panel (c). This panel now shows the spectrum at interleaving steps of 1 MHz. Panel (d) uses the same frequency scale as Panel (a), however, all 100 Fourier spectra are plotted now. The four  $5S_{1/2}, F_g = 2-5D_{5/2}$  transitions of  $^{87}\text{Rb}$  appear well-resolved.

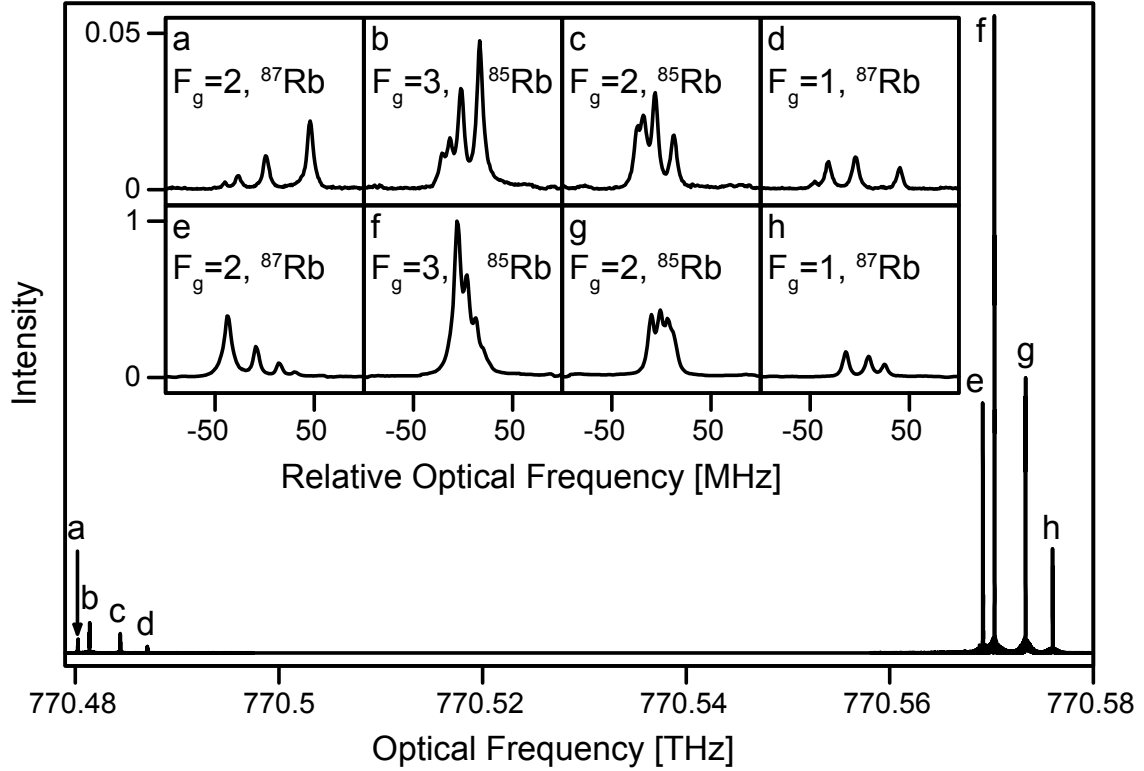


Figure 4.7: Doppler-free DC2pES spectrum of  $^{85}\text{Rb}$  and  $^{87}\text{Rb}$  interleaved at 1 MHz spacings. The insets show zooms into the respective transition regions. The spectrum was recorded at a vapor-cell temperature of 323 K. The top row of the insets (a-d) shows the  $5D_{3/2}$  transitions, the bottom row (e-h) shows the  $5D_{5/2}$  transitions.

RF-comb mode spacing  $\Delta f_{\text{rep}}$  has not been reduced further (which would further increase the optical free spectral range) in order to minimize the overlap of RF-comb modes with sidebands from other, neighboring RF-comb modes (see Sec. 4.2.4.1).

The insets highlight the achieved resolution by showing zooms into the data of the main panel. The hyperfine transitions labeled “e” are the same ones shown in Fig. 4.6. Like the other transitions of  $^{87}\text{Rb}$ , they are well-resolved. In contrast, the  $^{85}\text{Rb}$  transitions are often blended since the measured line width is of order of the line spacing. If all of these transitions were probed with the traditional direct-comb-spectroscopy scheme only employing a single comb, the covered spectral span would be folded into a comparably tiny spectral domain of 100 MHz. The result of this folding process can be calculated based on the DC2pES data of Fig. 4.6. The result is shown in the top half of Fig. 4.8.

The bottom part of the same figure shows the constituent transitions of the top part, i.e. the

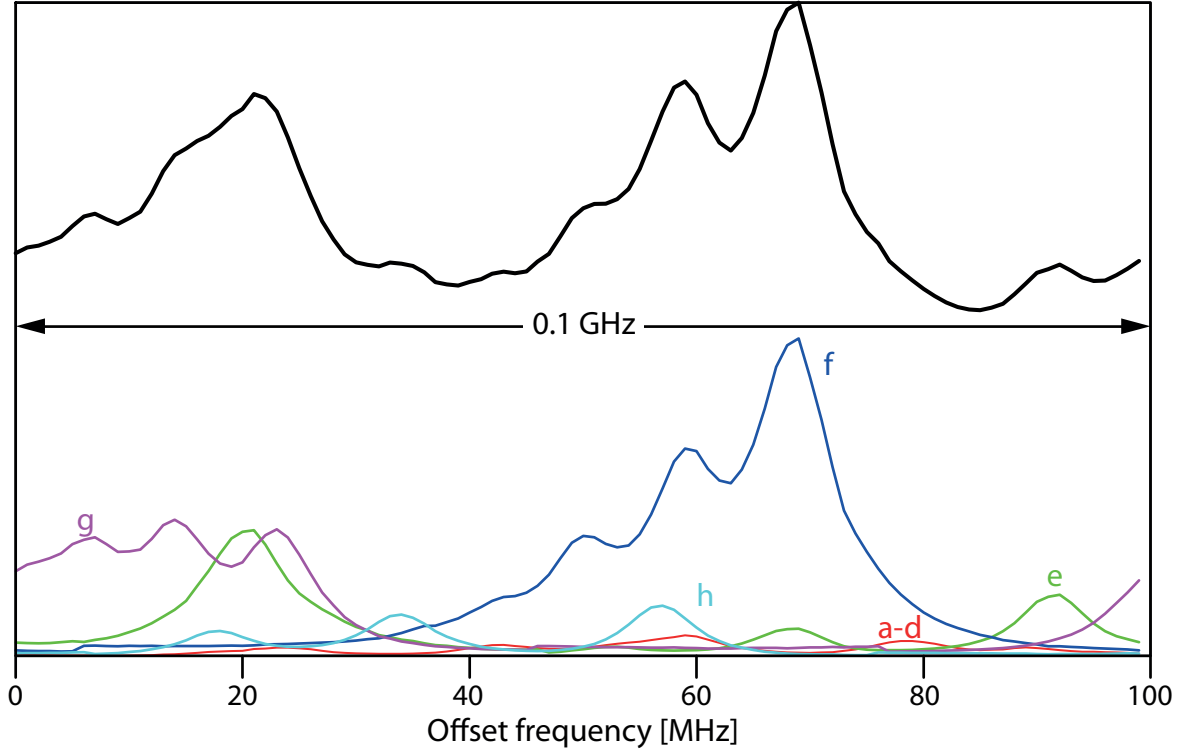
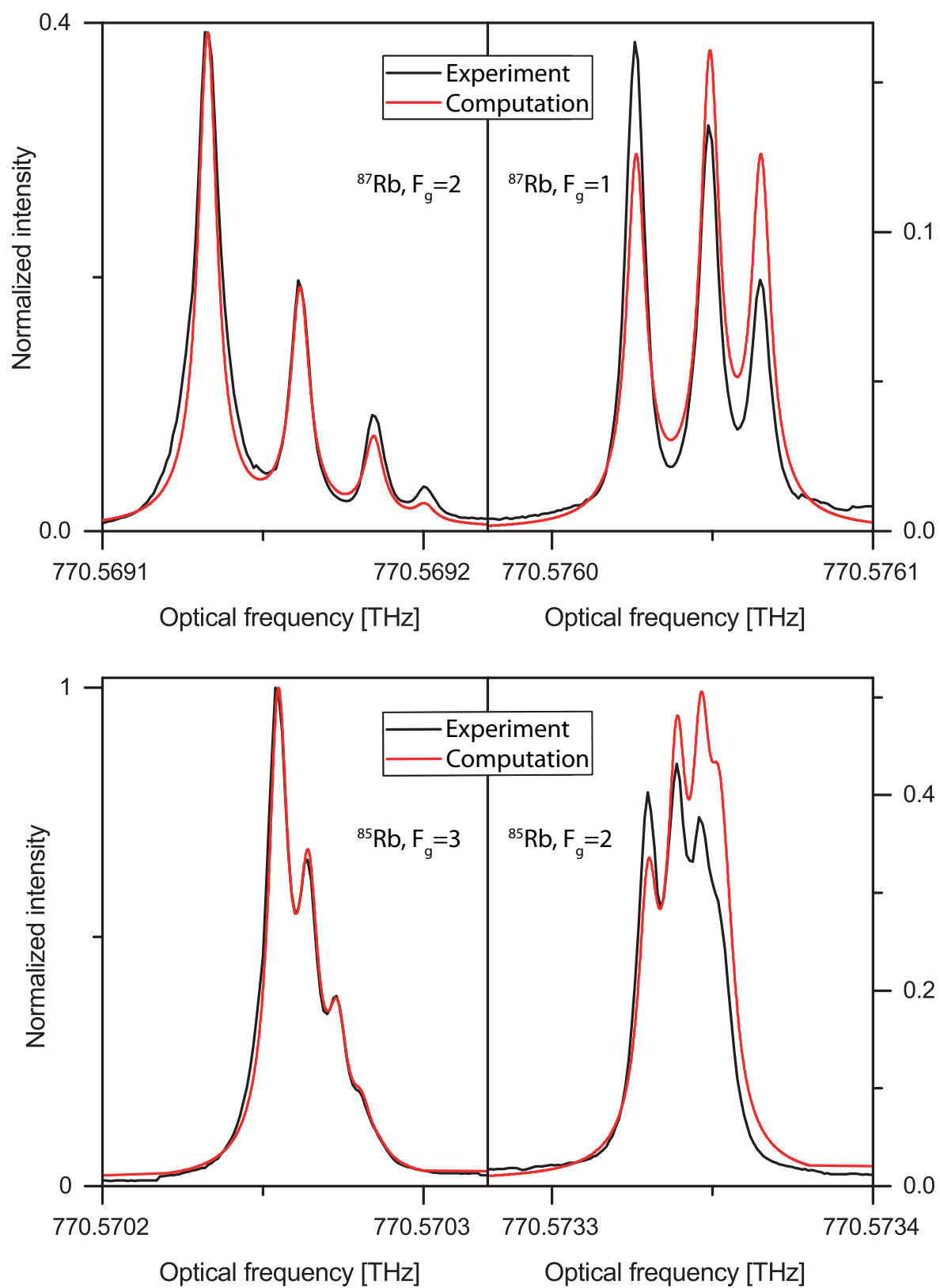


Figure 4.8: Direct single-comb spectrum equivalent to and derived from the fully interleaved DC2pES spectrum shown in Fig. 4.7. The labeling of transition sets is equal for the two figures. It is assumed that the comb is scanned by shifting the offset frequency  $f_{ce}$ . The  $5D_{3/2}$  transition profiles (a-d), represented by the red trace, are combined because of their relatively weak strengths.

experimentally measurable black trace is the sum of all colored traces. It should be obvious that only the strongest lines can be assigned with high confidence. Moreover, even that is only possible if the transitions are already well-known from other preceding experiments or calculations. Identification of  $J_f = 3/2$  transition lines with high confidence appears hardly possible, even when good estimates of their centers and shapes were to exist *a priori*. In contrast, the transition assignment for the DC2pES measurement is completely seamless and straight forward.

Figure 4.9 compares the experimental DC2pES data for the  $5S_{1/2}$ - $5D_{5/2}$  transition with computations incorporating residual-Doppler (Gaussian) broadening, transit-time (Laplacian) broadening, and natural-lifetime (Lorentzian) broadening. The resulting line shape, essentially a convolution of these three shapes, was first described by C. J. Bordé in Ref. [80]. Central line positions are taken from [61] and lifetimes are taken from [62, 50]. The calculations of the relative transition strengths are based on a standard calculus that can e.g. be found in classic textbooks like Ref. [81, Chap. 13, App. C.II]. The application of this calculus to the excitation

Figure 4.9: Experimental and computed  $5S_{1/2}-5D_{5/2}$ -transition spectrum.

of Rb under the given experimental conditions (circular polarization, counter-propagating beams) results in a 3rd-order nonlinear susceptibility proportional to the product [82]

$$\text{Im}(\chi^{(3)}) \propto \left( \sqrt{(2F_f + 1)(2F_g + 1)(2J_f + 1)(2J_g + 1)} \cdot \begin{Bmatrix} 0 & 1 & 1 \\ 3/2 & J_g & 1/2 \end{Bmatrix} \begin{Bmatrix} 1 & 2 & 1 \\ J_f & 3/2 & 1/2 \end{Bmatrix} \begin{Bmatrix} 1 & 1 & 2 \\ J_f & J_g & 3/2 \end{Bmatrix} \begin{Bmatrix} J_g & J_f & 2 \\ F_f & F_g & I \end{Bmatrix} \right)^2 \quad (4.15)$$

near resonance. This product, with  $\begin{Bmatrix} j_1 & j_2 & j_3 \\ j_4 & j_5 & j_6 \end{Bmatrix}$  denoting the Wigner 6- $j$  symbol, captures the influence of the transition-specific angular momentum quantum numbers on the transition rate. Details of the derivation of Eq. 4.15 are given in Appx. B.2. It can be seen that the experiment agrees decently well with theory. Deviations can be seen at the low-intensity parts of the lines, however, as potential influences of the intermediate states on the line shapes are not taken into account (see discussion in Sec. 4.4), no perfect match should be expected. For the same reason, the multiplicative normalization factor was chosen independently for the computed spectra of the two isotopes. This factor was chosen such that the largest value of the two spectra (computation and experiment) are equal for the respective isotope spectrum. It was by a factor of 1.35 larger for  $^{85}\text{Rb}$  than for  $^{87}\text{Rb}$ .

## 4.4 Analysis of Systematic and Statistical Errors

### 4.4.1 Accuracy of the Frequency Scale

The accuracy of the frequency scale in the DC2pES measurements naturally depends on the accuracy of the frequency references used, namely the H maser and the ultrastable CW laser, and the transfer of their accuracy to the excitation combs. The maser's fractional accuracy is specified as  $\pm 5 \cdot 10^{-13}/\text{year}$  [83]. This specification is confirmed by checking the maser's output against GPS [84]. A PLL should in principle always ensure that a reference's accuracy is transferred without degradation, since the error signal would else not be centered around zero. This assumption is, however, not experimentally verified for the six implemented PLLs, and as noted in Ref. [85], the transferred frequency could be subject to a systematic and stable offset. In this article by coworkers of mine, no such effect is found for PLL hardware identical to that used in the current experiments, and this source of inaccuracy is disregarded based on this finding.

The maser's fractional instability, quantified in terms of its Allan deviation, is also of order  $10^{-13}$  at 1 s, and averages further down to  $10^{-14}$  for observation times of 36 s [83] corresponding to the measurement time of a single spectrum. PLLs, including the behavior of the voltage-controlled oscillator, can easily have an influence on the transfer of this stability. However, since the maser is used to only lock frequency differences between optical lines, the maser's fractional instability would have to be degraded by an unrealistic  $\sim 9$  orders of magnitude to become as significant, in absolute terms, as the instabilities of the used optical reference (the ultrastable CW laser).

The reason why the ultrastable CW laser is the lynchpin for the instability of the measured optical transition frequencies is its use as the reference in locking the metrology comb's repetition rate. This rate enables the scaling from the RF to the optical domain; it is multiplied by the mode number ( $n \approx 7.7 \cdot 10^5$ ) of the mode which is locked to the ultrastable CW laser in the scaling process. Measuring the Allan deviation (at 1s) at the fourth harmonic of this repetition rate yields values ranging from 3 to 9 mHz (no averaging of the measurement results was implemented). This corresponds to a fractional instability of better than  $10^{-11}$  and to less than 8 kHz in the optical domain (two-photon transition frequencies). The repetition rate's stability could be limited by the CW laser's stability or the PLL. If it were the PLL, averaging the phase noise over longer periods should lead to smaller Allan deviations. If it were the CW laser, a possible drift could lead to Allan deviations that increase with observation time [79, Sec. 4.3.1]. That drift is characterized to 82 mHz/s (in the two-photon-transition-frequency domain). This amounts to a 3 Hz shift for the measurement time of 36 s for a single interleaving-step spectrum and a 410 Hz shift for the experimental measurement duration of 5040 s, which includes the time spent shifting  $f_{\text{DDS}}$  and triggering/saving the recordings.

In summary: The determined optical frequencies are very unlikely to be limited by the accuracy or instability of the H maser. Instead, the optical frequency determination is limited by frequency instability of the repetition rate of the metrology comb. This instability limits the uncertainty of the measured optical frequencies in each spectrum (interleaving step) to  $\sim 9$  kHz.

### 4.4.2 Determination of the Transition Frequencies

The nonlinear curve-fitting software “fityk” [86] is used to fit a mathematical model function to the measured, unweighted data employing the Levenberg-Marquardt algorithm. The fit function

is constituted of a sum of Gaussians and Voigt functions. It is given by

$$\text{Fit model} = \sum_{i=1}^{17} \frac{a_{i,0} \int_{-\infty}^{+\infty} \frac{\exp(-\tau^2)}{a_{i,3}^2 + \left(\frac{f-a_{i,1}}{a_{i,2}} - \tau\right)^2} d\tau}{\int_{-\infty}^{+\infty} \frac{\exp(-\tau^2)}{a_{i,3}^2 + \tau^2} d\tau} + \sum_{g=1}^4 a_{g,0} \exp\left(-\ln(2) \left(\frac{f-a_{g,1}}{a_{g,2}}\right)^2\right), \quad (4.16)$$

where the subscript  $i$  denotes the  $i$ -th Voigt function with height  $a_{i,0}$ , center  $a_{i,1}$ , Gaussian width proportional to  $a_{i,2}$ , and the ratio of Lorentzian and Gaussian widths proportional to  $a_{i,3}$ . The subscript  $g$  denotes the  $g$ -th Gauss function with height  $a_{g,0}$ , center  $a_{g,1}$ , and half-width at half maximum  $a_{g,2}$ . The fitted model therefore is a sum of 17 Voigt functions (one per hyperfine transition) and 4 Gaussian functions modeling the Doppler-broadened co-propagation background.

The fitting parameters  $a_{i,0}$ ,  $a_{i,1}$ ,  $a_{i,2}$ , and  $a_{i,3}$  were independent, unconstrained, and free. Likewise, the fitting parameters  $a_{g,0}$  and  $a_{g,1}$  were also independent, unconstrained, and free. In contrast, the fitting parameters  $a_{g,2}$  were set (i.e. fixed/locked) to the theoretical Doppler-width as determined by the cell's temperature. These four Gaussian widths  $a_{g,2}$  were the only parameters of the above model that were not fitted. The result of this fit is shown in Fig. 4.10, which includes the fit residuals below the spectral plots. It can be seen that the chosen fit model leads to an adequate fit of the experimental data. For the sake of completeness, additional statistical data on the fit result is compiled in Appx. B.

As is detailed in the following sections, the actual measured line profile is a combination of many things, not only including a Gaussian profile from residual Doppler effects, Lorentzian from lifetime effects, Laplacian from transit-time effects, but also some profile from frequency-pulling effects, some contribution from co-propagating background, some distortion from comb-line sidebands, and possibly some other yet unexplored effects. The choice of the above fit function is motivated by its very good convergence properties. A convolution of a Laplacian with a Gaussian as a fit model, thereby neglecting the atoms' natural linewidth was also implemented. The difference between the so determined line centers and the centers determined using Voigt functions were at most of the order of the standard error of the line centers of the Voigt functions. However, using the convolution of a Laplacian and a Gaussian as the fit model turns out to be extremely cumbersome. It very often results in diverging fit parameters and it never works for all transitions at once, but only for a single hyperfine-ground-state set at a time. This fit model is therefore discarded.



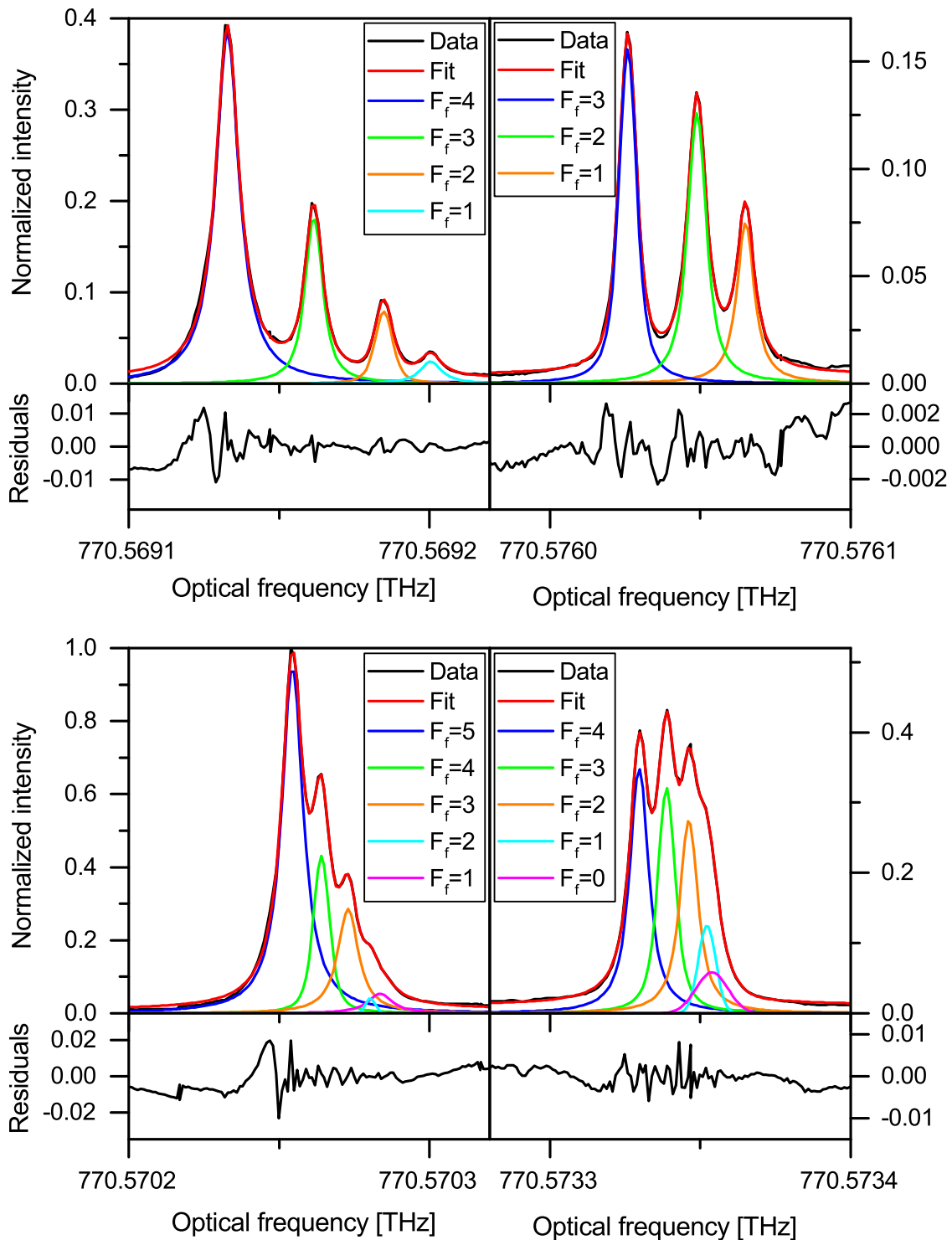


Figure 4.10: Comparison of the experimental  $5S_{1/2}-5D_{5/2}$ -transition spectrum with the fitted model function. The measured data is plotted in black, the full fit model is plotted in red, and individual fit components (i.e. individual Voigt functions) are plotted in blue, green, orange, cyan, or magenta. The fit residuals are plotted in separate panels below the respective spectrum.

### 4.4.3 Transit-Time Broadening

Using a Voigt function to model a hyperfine line in the measured spectrum is an approximation that, in particular, neglects the effect of transit-time broadening. Transit-time broadening results in a double-exponential shape, also known as Laplace distribution, or Laplacian, mathematically described by

$$L(f) = \exp\left(-\frac{|f - f_{\text{center}}|}{\delta}\right),$$

with the peak position given by  $f_{\text{center}}$ . A beam profiler (Spiricon, BM-USB-SP620) is used to determine the beam's  $4\sigma$  width right before the  $f = 150$  mm lens (focusing into the Rb cell). The measurement result was  $4\sigma = 3.0$  mm. From this, the Gaussian focal waist (FWHM) was determined to  $w_0 = 29.2$   $\mu\text{m}$ . Using this experimental focal beam waist, the calculated Laplacian width  $\delta = \sqrt{2k_B T / (\pi m w_0)}$  [87] in the experiment amounts to 3.2 MHz (FWHM  $\approx 4.5$  MHz). For comparison, the residual Gaussian FWHM can be calculated to be  $\approx 2.9$  MHz, and the natural line width (FWHM) is  $1/(2\pi \cdot \tau_{5D_{5/2}}) = 1/(2\pi \cdot 238.5 \text{ ns}) \approx 667$  kHz [50]. In the experiment the FWHMs of the fitted Voigt functions range from 7 to 10 MHz, seemingly not dependent (in a simple way) on the intensity of the line, nor the overlap with neighboring lines. E.g., the fitted FWHMs for the relatively isolated  $5S_{1/2}, F_g = 2-5D_{5/2}$  transitions of  $^{87}\text{Rb}$  are 9.4 MHz ( $F_f = 4$ ), 7.1 MHz ( $F_f = 3$ ), 7.0 MHz ( $F_f = 2$ ), and 8.8 MHz ( $F_f = 1$ ).

### 4.4.4 Magnetic-Field-Induced (Zeeman) Shifts

To determine the magnetic field along the beam axis, a direct single-comb spectrum was measured with two different circular polarizations. The field along the axis is assumed to be zero when the peak position of a line that is sensitive to magnetic fields was the same in both spectra. Specifically, the studied hyperfine transition line was the  $5S_{1/2}, F_g = 3-5D_{5/2}, F_f = 5$  transition of  $^{85}\text{Rb}$ . The uncertainty in the peak position after this nulling procedure was about 8 kHz (in transition frequency, not laser frequency). This value corresponds to the remaining shift of the observed line when changing from one circular polarization to the other after the nulling procedure was performed. The origin of this residual shift is yet unexplored.

For the magnetic field perpendicular to the beam axis, the zero field position is expected where the peak transition intensity of the same line was highest. This made the nulling procedure somewhat less precise, with an uncertainty of about  $\pm 0.15$  Gauss. This uncertainty corresponds to the range of current levels, provided to the Helmholtz coils, that are found to lead to the

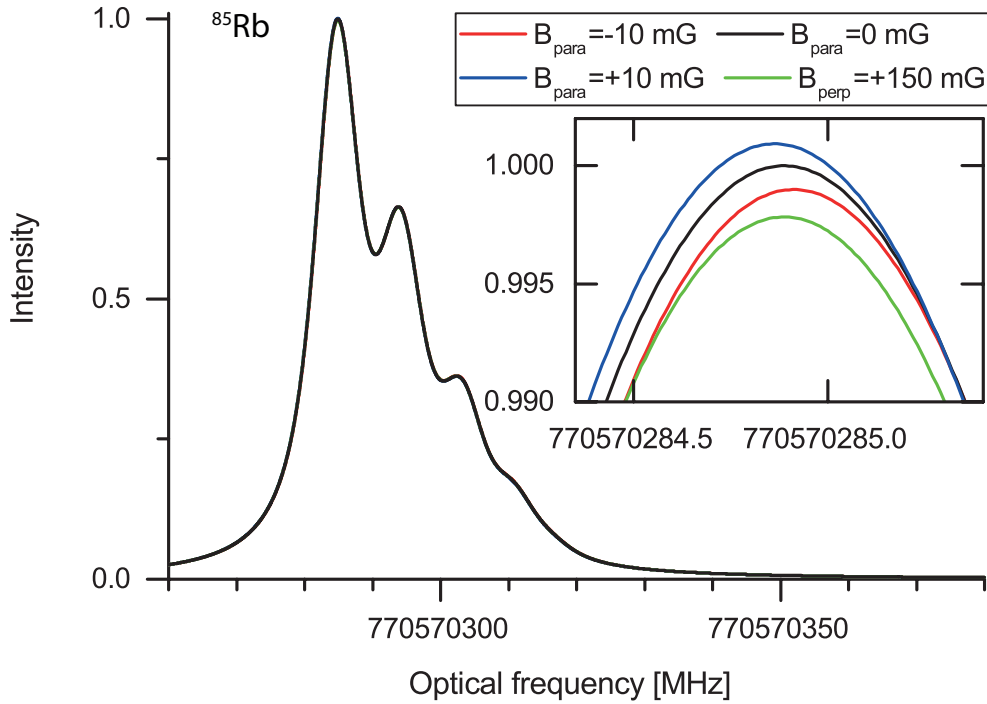


Figure 4.11: Simulation of the effect of the estimated residual fields on the  $5S_{1/2}, F_g = 3-5D_{5/2}, F_f = 5, 4, 3, 2, 1$  transition lines of  $^{85}\text{Rb}$ . The inset shows a zoom into the peak of the  $5S_{1/2}, F_g = 3-5D_{5/2}, F_f = 5$  transition line.  $B_{\text{para}}$  indicates a field applied parallel to the beam axis, whereas  $B_{\text{perp}}$  indicates a field applied perpendicular to the beam axis.

same, highest peak transition intensity. At a perpendicular field of  $\pm 0.15$  Gauss, the Zeeman shift is about 2.9 kHz towards lower transition frequencies, regardless of the sign of the field. Combining the uncertainty for the parallel direction and each of the two perpendicular directions results in an uncertainty of about 11 kHz. This uncertainty is similar to the value of  $\pm 20$  kHz given in Ref. [88] for the same transitions and with the same field-compensation scheme employing three mutually perpendicular Helmholtz coils.

Figure 4.11 shows simulations of the effect of the residual magnetic fields on the  $5S_{1/2}, F_g = 3-5D_{5/2}$  transitions. The shifts and intensity changes are so small that all lines seem to perfectly overlap and only a zoom into the peaks of the lines, as done for the  $5S_{1/2}, F_g = 3-5D_{5/2}, F_f = 5$  transition in the inset of the same figure, reveals the differences in peak intensities and peak frequencies. The simulations leading to the results visualized in Fig. 4.11 assume Voigt line shapes with a FWHM of 7.8 MHz, corresponding to the average of the fitted FWHMs of the three strongest  $5S_{1/2}, F_g = 3-5D_{5/2}$  lines. They furthermore incorporate all allowed transitions between Zeeman sub levels. The intensity  $I_{gf}$  of the lines associated with transitions between

these sub levels is determined by calculating

$$I_{gf} \propto |\langle \Psi_g | T_2^2(\mu^2) | \Psi_f \rangle|^2, \quad (4.17)$$

where  $|\Psi_g\rangle$  is the  $5S$  eigenstate,  $|\Psi_f\rangle$  is the  $5D$  eigenstate, and  $T_2^2(\mu^2)$  is a spherical tensor operator involving the transition dipole moment operator  $\mu$  [89, Sec. 4.3]. In general, each  $|\Psi\rangle$  is a sum over multiple  $F$  and magnetic quantum numbers, denoted by  $M_F$ . Equation 4.15 covers most of the calculation of  $I_{gf}$ : apart from some phase factors, the main factor that is missing is the Wigner 3- $j$  symbol  $\begin{pmatrix} F_g & 2 & F_f \\ -M_{F_g} & 2 & M_{F_f} \end{pmatrix}$  and a sum over all  $M_F$ 's. The details of the calculation are compiled in Appx. B.2.

### 4.4.5 Collisions and Impurities

The pressure shift for the  $5S$ - $7S$  transition is given in Ref. [90] for Rb as  $-100$  kHz (transition frequency) / mTorr ( $\approx -0.75$  kHz/mPa). In Ref. [91], B. P. Stoicheff and E. Weinberger measured pressure-induced frequency shifts for the  $n^2S$  and the  $n^2D$  series in natural rubidium via by Doppler-free two-photon spectroscopy. They obtain that both series yield similar pressure shifts and that both series are monotonically decreasing with decreasing  $n$  for  $n \leq 25$ . Based on these measurements, it can be concluded that the shift for the  $5S$ - $5D$  transition should not be much different from the shift of the  $5S$ - $7S$  transition. Using the vapor pressure formula from Ref. [92], the pressure shifts at the experimental pressure level of  $4 \cdot 10^{-3}$  mTorr ( $\approx 0.5$  mPa) [93] can be estimated as  $-0.5$  kHz.

The Rb container, a 30-mm-long, 10-mm-high, and 10-mm-wide quartz cell, neither has Brewster windows nor any coatings and is purchased from Ophos Instruments. Rubidium is brought into the cell by zone melting [94] and the cell is thereafter pumped for a period of time. According to the manufacturer [95], the pressure in the cell is generally about  $5 \cdot 10^{-6}$  Torr before the seal-off is performed. Reference [96] estimates an extra 5 kHz to the expected shift for impurities for a vapor cell likely to be similar to the one used here.

### 4.4.6 AC Stark Shift

According to Ref. [97], the AC Stark shift amounts to  $-422$  Hz/mW. Given the total power of about 25 mW, this corresponds to a shift of roughly  $-10$  kHz. This result is experimentally tested by reducing the power by up to 70% of the total laser power while measuring a direct single-comb spectrum. In this experiment, no shifting of lines was observable at a level of 10–20 kHz or higher, limited primarily by low SNR for low powers and the MHz-level linewidths.

### 4.4.7 Frequency Pulling

Driving a two-photon transition with two lasers that are only slightly detuned from an intermediate state can slightly shift the measured two-photon transition energy. If the spectral intensity above and below the intermediate state were equal, this effect would cancel out, but as some of the light is absorbed by the rubidium vapor, this can lead to an asymmetry of the spectrum.

	$F_i$	Shift [kHz]	Amplitude
$^{87}\text{Rb}, F_g = 2$	1	+82	0.96
	2	+85	0.91
	3	-45	0.88
$^{85}\text{Rb}, F_g = 3$	2	+300	0.73
	3	+220	0.69
	4	-160	0.68
$^{85}\text{Rb}, F_g = 2$	1	+90	0.76
	2	+30	0.75
	3	-110	0.76
$^{87}\text{Rb}, F_g = 1$	0	+50	0.94
	1	+25	0.93
	2	-45	0.94

Table 4.1: Frequency-pulling-induced shifts.

Reference [98, Eq. 10] gives a relatively detailed expression for calculating the pulling effect, though it is only for one detuning. To capture the specifics of DC2pES, an integration over all detunings has to be carried out and a weighting factor that incorporates the absorption by the rubidium vapor before the center of the cell has to be added. To keep the calculation complexity manageable, only a single intermediate state is assumed, though in reality, many of the transitions can have multiple intermediate states. Table 4.1 details the expected pulling

at 323 K for each ground hyperfine state  $F_g$  and each intermediate hyperfine state  $F_i$ . The amplitude is the transition strength relative to the case where there is no absorption by the rubidium before the interaction region.

While the numbers above do not provide an exact estimate of the expected shift for each transition, they at least provide an order-of-magnitude estimate for the effect.

#### 4.4.8 Systematic Effects Induced by the Dual-Comb Technique

As described already in Sec. 2.2, a beat note between two neighboring comb modes (one from each comb), both probing a given absorption/excitation profile, is detected in dual-comb spectroscopy. The fact that the two comb lines probe the profile at different frequency positions, spaced by the RF frequency at which the beat note can be observed, could potentially have an influence on the line shape and even its central position. Figure 4.12 shows the results of a test of this hypothesis. The black trace shows a line profile resulting from a convolution of a Gaussian of FWHM 2.9 MHz and a Laplacian of FWHM 2.2 MHz, yielding a total FWHM of 4.64 MHz. These values were chosen similar to the expected broadening contributions from residual Doppler-broadening and transit-time broadening, respectively.

The black trace can be regarded as the resonance-profile that would be measured with a stable CW laser. To test the numerical accuracy of the employed fitting routines, this line is sampled at intervals of 1.28 MHz and fitted with the “real” line-shape function, i.e. a convolution of a Gaussian and a Laplacian. The value of 1.28 MHz corresponds to the experimental central RF frequency at which the DC2pES beat notes (i.e. the DC2pES RF spectral lines) of Sec. 4.3 are observed. The deviation of the true line center from the fitted line center amounts to -0.15 nHz. Fitting the same data points with a Voigt function results in a deviation of the true line center from the fitted line center of 41 Hz.

The real line profile is then sampled in a dual-comb scheme resulting in the data points marked by black crosses. Fitting of these data points with the real line-shape function results in a deviation of the true line center from the fitted line center of -0.37 Hz. Fitting the same data points with a Voigt function results in a deviation of the true line center from the fitted line center of 40 Hz. The linewidths of the measured lines were broader than 4.64 MHz, however, the influence of the inter-comb mode spacing can be expected to increase with decreasing absorption-resonance widths. The above values can therefore be regarded as upper limits for

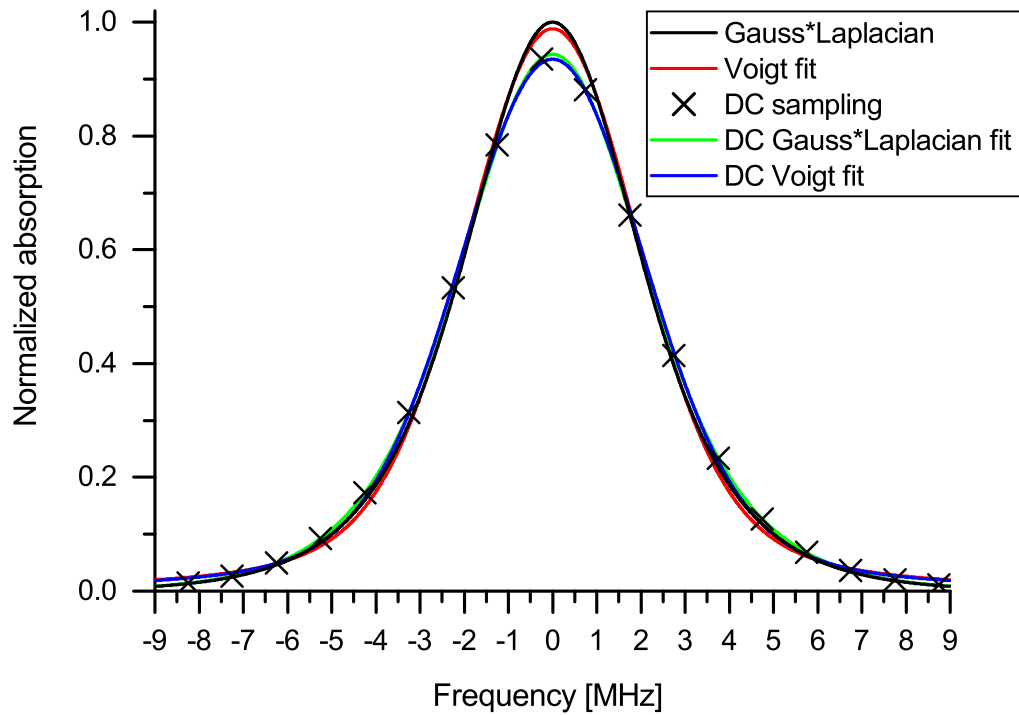


Figure 4.12: Investigation of the effect of dual-comb (abbreviated as “DC” in the plot legend only) sampling of a resonance profile. The sampled, “real” profile is assumed to be a convolution of a Gaussian with a Laplacian (black line). A fit of this line with a Voigt function is shown in red. The result of dual-comb sampling of the black line is marked by black crosses (the sampling interval equals 1.28 MHz). The fit of these data points with a convolution of a Gaussian with a Laplacian is shown in green and the fit of these data points with a Voigt function is shown in blue.

the experimental configuration. From these results it can be concluded that the dual-comb approach of sampling a resonance line has negligible influence on the measured line center.

#### 4.4.9 Errors from the Fit and Deviations from Literature Values

Summing up the various error sources discussed above, a difference of a few 100 kHz between the transition frequencies measured in the present work and literature values can be anticipated. All discussed systematic errors and the sum thereof are compiled in Table 4.2.

The transition frequency and the statistical and systematic error of each  $5S_{1/2}-5D_{5/2}$ -transition line are summarized in Table 4.3. The statistical errors are the standard errors computed by

Inaccuracy of the frequency scale (Sec. 4.4.1)	9 kHz
Zeeman shift (Sec. 4.4.4)	11 kHz
Pressure shift (Sec. 4.4.5)	0.5 kHz
Impurity shift (Sec. 4.4.5)	5 kHz
AC Stark shift (Sec. 4.4.6)	10 kHz
Frequency pulling (Sec. 4.4.7)	300 kHz
Dual-comb-specific shift (Sec. 4.4.8)	40 Hz
Sum of all systematics	340 kHz

Table 4.2: Summary of systematic shifts.

the fitting software “fityk” [86]. The standard error provides a measure for the precision with which the respective parameter is estimated by the regression in much the same way as the standard error of the mean does for a group of measurements [99, Sec. 6.6.3]. It is calculated from the sum of squared residuals and the Hessian matrix, the calculation of which are intrinsic to the Levenberg-Marquardt routine [100, Chap. 2].

Table 4.3 also compares the results with literature values from Ref. [61], that were obtained by scanning a CW Ti:Sa laser through the two-photon transitions and measuring the induced  $6P$ - $5S$  fluorescence with a PMT as a function of the CW-laser frequency. The authors claim a total uncertainty of 16–52 kHz, the concrete value depending on the strength and blendedness of the respective transition, without specifying exactly how the influence of blendedness is estimated. For comparably isolated lines (claimed uncertainty of 16 kHz), the uncertainty is mainly due to the uncertainties in their optical frequency references. All deviations between the transition frequencies measured in the present work and the quoted reference values are consistent with either the statistical error or shifts that can be expected from the systematic effects discussed above.

## 4.5 Summary

In the experiments discussed above, two atomic species ( $^{85}\text{Rb}$  and  $^{87}\text{Rb}$ ) exhibiting a total of 33 hyperfine transitions are simultaneously probed. The shown measured spectra demonstrate the capability of DC2pES to acquire broad (>100 GHz), highly resolved (1 MHz), narrow transition-linewidth (7 MHz), accurate (systematic uncertainty of  $\sim 340$  kHz), high-SNR ( $10^4$ ) spectral data that is consistent with basic computational predictions and free of back-folding issues. As the spectral span is, in principle, only limited by the bandwidths of the excitation



	$F_f$	Transition Frequencies [kHz] This Work	Trans. Freq. [kHz] From Ref. [61]	This Work – Ref.[61][kHz]
$^{87}\text{Rb}$ $F_g=2$	4	$770569132807 \pm (15)_{\text{stat}} \pm (340)_{\text{syst}}$	$770569132733 \pm 16$	75
	3	$770569161538 \pm (27)_{\text{stat}} \pm (340)_{\text{syst}}$	$770569161556 \pm 16$	-18
	2	$770569184795 \pm (61)_{\text{stat}} \pm (340)_{\text{syst}}$	$770569184510 \pm 16$	284
	1	$770569200426 \pm (254)_{\text{stat}} \pm (340)_{\text{syst}}$	$770569200450 \pm 16$	-24
$^{85}\text{Rb}$ $F_g=3$	5	$770570284435 \pm (16)_{\text{stat}} \pm (340)_{\text{syst}}$	$770570284734 \pm 16$	-299
	4	$770570294045 \pm (27)_{\text{stat}} \pm (340)_{\text{syst}}$	$770570294170 \pm 16$	-124
	3	$770570302905 \pm (127)_{\text{stat}} \pm (340)_{\text{syst}}$	$770570303190 \pm 16$	-285
	2	$770570310317 \pm (966)_{\text{stat}} \pm (340)_{\text{syst}}$	$770570310795 \pm 16$	-478
	1	$770570313534 \pm (7378)_{\text{stat}} \pm (340)_{\text{syst}}$	$770570316276 \pm 26$	-2742
$^{85}\text{Rb}$ $F_g=2$	4	$770573329707 \pm (50)_{\text{stat}} \pm (340)_{\text{syst}}$	$770573329924 \pm 16$	-216
	3	$770573338776 \pm (97)_{\text{stat}} \pm (340)_{\text{syst}}$	$770573338922 \pm 16$	-146
	2	$770573346186 \pm (114)_{\text{stat}} \pm (340)_{\text{syst}}$	$770573346509 \pm 16$	-323
	1	$770573352233 \pm (905)_{\text{stat}} \pm (340)_{\text{syst}}$	$770573351996 \pm 20$	237
	0	$770573353865 \pm (12517)_{\text{stat}} \pm (340)_{\text{syst}}$	$770573354902 \pm 52$	-1037
$^{87}\text{Rb}$ $F_g=1$	3	$770575995886 \pm (31)_{\text{stat}} \pm (340)_{\text{syst}}$	$770575996244 \pm 16$	-359
	2	$770576018874 \pm (41)_{\text{stat}} \pm (340)_{\text{syst}}$	$770576019200 \pm 16$	-326
	1	$770576035050 \pm (69)_{\text{stat}} \pm (340)_{\text{syst}}$	$770576035134 \pm 16$	-84

Table 4.3: Summary of measured transition frequencies and comparison with literature data.

sources, the acquisition of Doppler-free spectra spanning 10s of THz appears feasible.

The prospects for DC2pES in precision spectroscopy are intriguing: Essentially, this technique combines the advantages of CW-laser-based spectroscopy (no back-folding) with advantages of direct-comb spectroscopy (availability in virtually all spectral regions, high excitation efficiency, mode-hopping free). To give but one example: As of this writing, experiments are underway at the Max Planck Institute of Quantum Optics to measure the  $1S_{1/2}, F_g = 1$ - $3S_{1/2}, F_f = 1$  transition of hydrogen at  $2 \times 205$  nm via conventional direct frequency-comb spectroscopy [101, 102]. Due to the small energy difference between the  $3S_{1/2}$  and the  $3D_{3/2}(3D_{5/2})$  state of merely 3 GHz(4 GHz), and due to hyperfine splitting of all of the involved states, a total of 8 states need to be considered when exciting with even a relatively narrowband ps laser. Both,  $f_{ce}$  and  $f_{rep}$  need to be chosen very carefully to isolate the transition of interest, however, even then, neighboring lines appear folded back to frequencies as close as 3-4 linewidths away from the  $1S_{1/2}, F_g = 1$ - $3S_{1/2}, F_f = 1$  transition. Such close-proximity lines can easily cause systematic shifts and need to be carefully investigated. Applying DC2pES to such a system could eliminate such concerns.



# 5 Towards Liquid-Phase Dual-Comb Two-Photon Spectroscopy

While the spectral analysis of gases is used in countless fields of application, spectral analysis of liquid solutions is often in greater demand in biological and chemical sciences. Because of its inability to measure spectral lines that are significantly broader than the comb's mode spacing, this domain has so far completely gone unexplored by conventional direct frequency-comb spectroscopy (DFCS) as implemented in e.g. Refs. [63, 64]. The disjointedness of the scientific communities of metrologists and biochemical spectroscopists adds its part to the nonexistent dissemination of conventional DFCS to low-resolution ( $\gg 1$  GHz) experiments. The development of dual-comb spectroscopy allows to access this application-rich phase space by direct frequency comb spectroscopy. This chapter, for the first time, explores the feasibility of dual-comb spectroscopy on electronic states in the condensed phase.

Section 5.1 describes the main experimental challenges of liquid-phase DC2pES compared to the preceding DC2pES gas-phase experiments. It also provides an overview over the few existing FTS two-photon spectroscopy studies. Section 5.2 details on the setup used for liquid-phase DC2pES. Finally, the first obtained results are shown and discussed in Sec. 5.3.

## 5.1 Background

The feasibility of Fourier-transform-based two-photon excitation spectroscopy in the condensed phase has so far been demonstrated for Michelson-based [20, 36] and pulse-shaper-based FTS [103]. In the case of the former method, minimum acquisition times are generally limited to the  $\sim$ ms timescale for resolutions of order 100 GHz by the travel speed of the mechanical delay-introducing component. In contrast, the pulse-shaper technique is free of any mechanical

moving part. However, both of its most widespread realizations, utilizing a liquid-crystal-spatial-light-modulator (LC-SLM) or an acousto-optic programmable dispersive filter (Dazzler), have bandwidth-limiting properties: The response time of a typical LC-SLM is typically limited to a few 10's of ms<sup>1</sup> [105], whereas the modulation bandwidth of the Dazzler is limited to 10 kHz [106]. The suitability of Dazzlers is additionally compromised because it only allows to shape a fraction of high-repetition-rate broadband pulses in the desired way. In Ref. [106], this fractional factor is 6%. These limits compare to a minimal, Niquist-limited measurement time of below 1  $\mu$ s for the same lasing frequencies as in Ref. [36], but with a higher repetition rate of 1 GHz, corresponding to the repetition rate of the combs used in the following experiments of this thesis. Since standard pixel rates of multiphoton microscopes are  $\sim$ 1 MHz or below [107], dual-comb multiphoton microscopy seems possible without a penalty on imaging speed. As measurement times also generally depend on signal-to-noise and sensitivity considerations, it is the goal of this chapter to determine to what extent this potential can be tapped.

The main feature of the experiment reported in this chapter that sets it apart from the experiments reported in Chap. 3 and 4, is the broadness of the studied spectral lines associated with electronic transitions in liquids. While the spectral lines in Chap. 4 have a width of  $\sim$ 7 MHz and those in Chap. 3 have a width of  $\sim$ 1 GHz, the spectral lines of liquids often spread over tens of THz. The dominant broadening mechanism of liquid solutions is local-field broadening<sup>2</sup> due to spatially varying solute-solvent interaction potentials [110, Sec. 2.5.3]. The very broad line profiles impose a series of requirements not as strictly existent with gas-phase samples: (i) Trivially, broad resonance bands ask for excitation sources with an even broader, ideally flat bandwidth. Achieving a very broad flat source spectrum is technologically very demanding, and alternatively one can resort to measuring the light sources (two-photon) spectrum and referencing the measured molecular (two-photon) spectrum against this source spectrum. (ii) The phase-stability of comb modes is to be maintained over large parts of the excitation spectrum as e.g. in Ref. [111], rather than just locally around the comparably narrow lines of interest as e.g. in Ref. [58]. (iii) While resolution goals are easily met, acquisition rates should be as high as possible. The mentioned local-field broadening is an inhomogeneous effect, and as such leaves the population relaxation dynamics of the solute molecules largely unaffected, e.g.

---

<sup>1</sup>For example, the rise time, defined as the “time required to change from 10% to 90% for  $2\pi$  modulation”, of the X10468/X13267/X13138 series LC-SLMs from Hamamatsu Photonics K.K. is specified as 5-30 ms [104].

<sup>2</sup>In addition to the inhomogeneous broadening mechanism of local-field broadening, typically smaller contributions from homogeneous broadening mechanisms such as collisional broadening can arise [108, Sec. 3.7]. However, as a homogeneous broadening mechanism, the associated exponential coherence decay (with the “homogeneous dephasing time”  $T_2$ ) is typically much slower than the approximate Gaussian inhomogeneous dephasing [109, Sec. 9.7.1].

making it still possible to measure excited-state relaxation dynamics on fs-ms time scales [112]. Consequently excited-state-lifetime effects can have similar acquisition-rate-limiting effects as in the experiments of Chap. 3, and need to be accounted for in DC2pES. (iv) As touched on in Sec. 2.3, the temporal (near-) coincidence of the phases of all modes of a phase-locked laser is a necessary condition for the formation of short pulses. After the coincidence time point, the modes dephase, and rephase again after the laser's round-trip time. Based on this observation, it can be expected that the DC2pES signal from molecular bands, which are as broad or even broader than the sources' excitation bandwidths, will exhibit the same dephasing characteristic [113]. Due to finite detector/ADC dynamic range, the region where spectroscopic information can be gathered, i.e. interferometric modulations are visible, is constrained to the pulse overlap region. This situation is completely analogous to interferometric second-order autocorrelation measurements, where information is also gathered from the pulse-overlap region only (see Sec. 2.2, or Ref. [114]). A marked difference, however, can be found in the implications for the duty cycle of Michelson-based interferometers and DC2pES, respectively: While the duty cycle can be chosen close to 1 by only measuring in the pulse-overlap region in the former case, the duty cycle is approximately given by  $\Delta t f_{\text{rep}} \sim 10^{-5}$ , where  $\Delta t$  is the pulse width of the excitation source, in DC2pES.

The fluorophores of choice for demonstrating the feasibility of DC2pES are Alexa Fluor® 488, Alexa Fluor® 568, Coumarin 480, and Rhodamine B. Owing to their large two-photon-absorption cross-sections and fluorescent quantum yield, all of them are common fluorescent probes in biomedical microscopy. Their two-photon cross sections, as taken from Refs. [115, 116], are reproduced in Fig. 5.1.

## 5.2 Experimental Setup

The experimental setup used for DC2pES in the liquid phase is shown in Fig. 5.2. Because the resolution goal is much less demanding, no *a posteriori* phase-correction scheme is implemented, making the setup considerably simpler than the setups described in the previous two chapters. The generators of the optical frequency combs are commercially available Kerr-lens-mode-locked Ti:Sa fs-oscillators (Laser Quantum, Taccor ultra). They deliver pulses of ~15 fs duration (transform-limited FWHM) and a pulse energy of 1.6 nJ at a repetition rate of 1 GHz. The output pulses of the oscillators are chirped with +450 fs<sup>2</sup>. This chirp, as well as second-order dispersion due to optics in the beam path, is measured with a commercially avail-

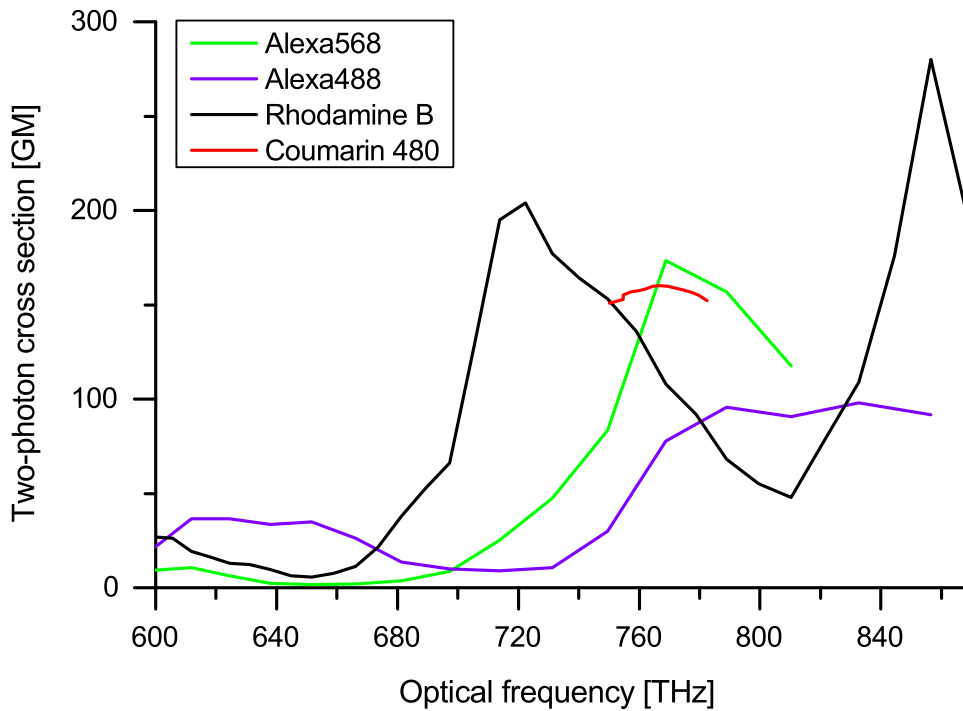


Figure 5.1: Absolute two-photon cross sections of the investigated fluorophores reproduced from Refs. [115, 116]. The frequencies on the abscissa are transition frequencies. The bandwidth covered with the laser system described in the next section roughly ranges from 740 THz to 800 THz.

able SPIDER interferometer (Venteon SPIDER) and compensated by chirped mirrors (CMs). Because of its transmission through the plate beam combiner, when compared to the output of Comb 2, the output of Comb 1 is chirp-compensated by an extra  $4 \cdot (-40) \text{ fs}^2$  from an extra pair of CMs. The alternative solution of using a pellicle beam combiner is discarding based on its highly chromatic transmission and reflectance properties. The amount of chirp compensation common to both outputs is  $10 \cdot (-80) \text{ fs}^2$  for the reference measurements and  $14 \cdot (-80) \text{ fs}^2$  for the fluorophore measurements. This difference in chirp-compensation is necessary because of the rather thick standard fluorometer quartz cell with an optical path length of 2 mm and a wall thickness of 1.25 mm used as the solution container in the experiments. This complication could be avoided in future experiments by using thinner cells (sheet thicknesses of 10  $\mu\text{m}$  are commercially available e.g. from Starna GmbH) or liquid sample jets [117].

Following the chirp compensation, the combined beam is focused by an achromatic doublet of focal length  $f = 19 \text{ mm}$  into the nonlinear medium. The origin region of the detected fluorescence, i.e. the focal spot, was visibly much shorter than the cuvette's 2 mm path length.

Contributions from a nonlinear response of the cell walls to the light pulses can therefore be regarded as highly unlikely. This is particularly true if one additionally takes the sideways detection geometry and the narrow-optical-band (10 nm FWHM) detection into account.

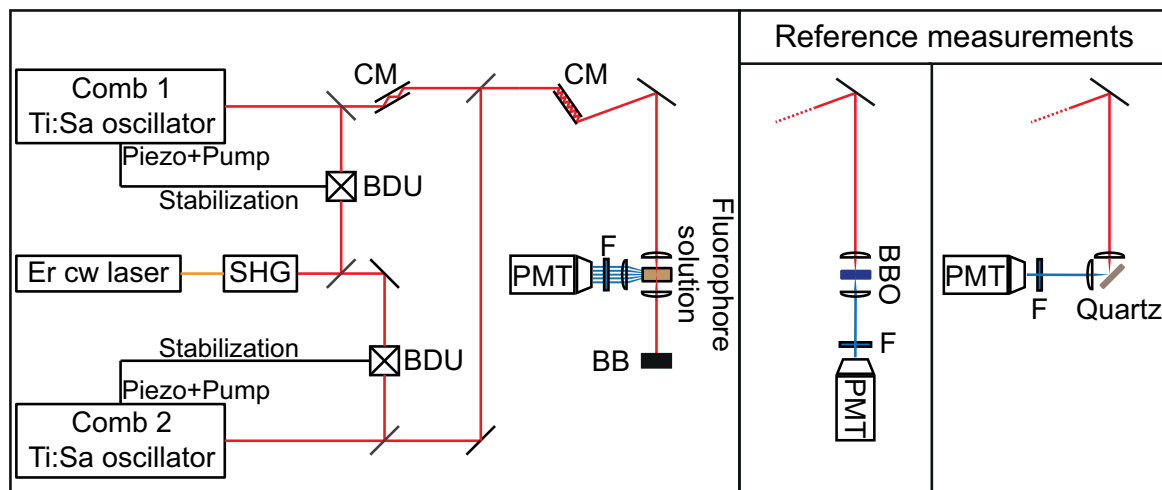


Figure 5.2: Setup of condensed-phase DC2pES. Both combs are stabilized to the same frequency-doubled Er CW laser at  $f_{\text{CW}} = 378$  THz (793 nm). Chirp-compensation is achieved with chirped mirror pairs. The overlapped, collinearly propagating light from both combs is focused into either a liquid fluorophore-solvent solution to measure the fluorophore response, or into crystals for reference measurements. CM: chirped mirrors, BDU: beat-detection unit, PMT: photomultiplier tube, F: optical filters, BB: beam block.

As already indicated in Sec. 2.2, the laser's inherent two-photon spectrum is given by the  $2\omega_0$  component (or equivalently the  $2f_0$  component with  $f_0 = \omega_0/(2\pi)$ ) of its quadratic interferometric autocorrelation (Eq. 2.17). This spectrum can be measured by using a nonlinear medium whose two-photon response is spectrally flat within the bandwidth of the lasers. Typical choices of such media are photodiodes with a bandgap that can be bridged by absorption of a minimum of two photons, thin nonlinear crystals, and surface SHG [118, 119]. Hashimoto et al. [36] found that SHG at the surface of a z-cut quartz crystal has the broadest spectrally flat two-photon response of all the mentioned candidates. z-cut polished quartz crystals were purchased from IMPEX HighTech and the two-photon spectrum is measured in the geometry shown in the rightmost panel of Fig. 5.2. For comparison purposes the two-photon spectrum is also measured by using a 20  $\mu\text{m}$  thick beta-barium-borate (BBO) crystal from Newlight Photonics. These measurements are referred to as reference measurements since they serve the purpose of correcting the two-photon excitation spectrum of any fluorophore of interest for the spectral profile of the excitation source. This is fully analogous to linear spectroscopy, where knowledge of the laser's fundamental, i.e. its one-photon spectrum, is necessary to correctly determine a sample's linear spectrum. Also fully analogously with linear

spectroscopy, in principle, any deviation from the lasers' two-photon spectrum is due to the sample's characteristic response to two-photon excitation and can therefore be identified as its two-photon excitation spectrum [20].

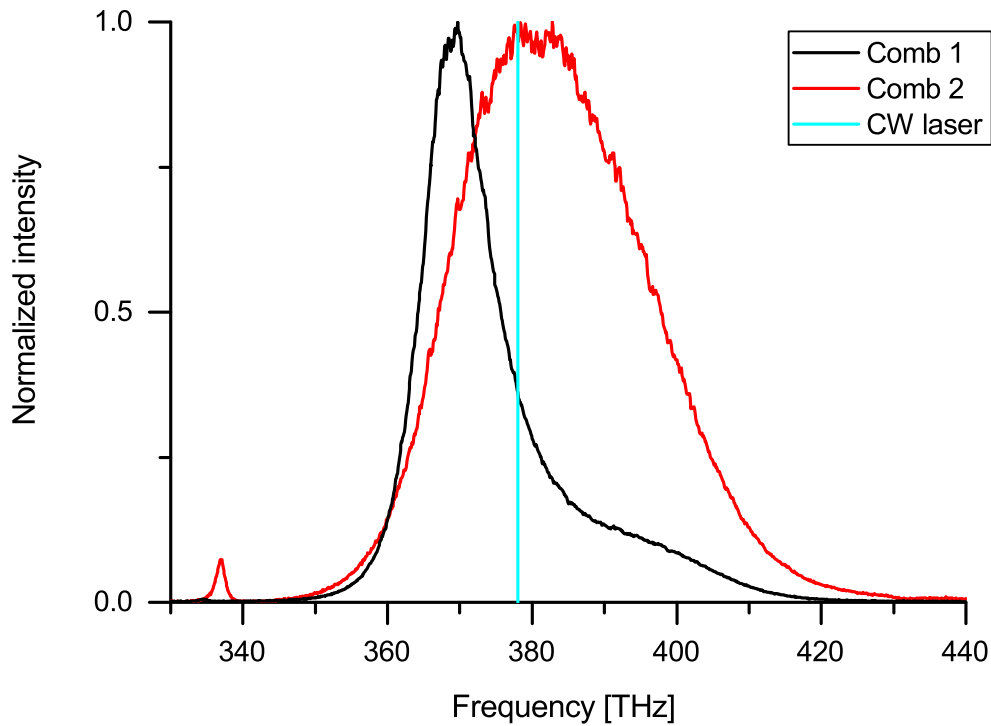


Figure 5.3: Spectra of the Laser Quantum Taccor lasers used for the experiments reported in this chapter. These spectra were measured with a grating spectrometer (US4000, Ocean Optics).

In both, the fluorophore and the reference measurements, the emitted light is spectrally filtered by appropriate optical filters and detected with a PMT (Hamamatsu H10721-210). The PMT's current output is amplified with a transimpedance amplifier (DHPCA-100) with a gain of  $10^3$  V/A to match the fixed voltage range of the ADC. The amplifier's -3 dB bandwidth is specified as 175 MHz, making it the measurement-bandwidth-limiting electronic device. The amplifier's voltage output is digitized at 12 bit resolution with a sampling rate of up to 1.8 GHz (AlazarTech ATS9360).

The combs' spectra are shown in Fig. 5.3. Also indicated in the same figure is the frequency of the free-running frequency-doubled Er CW laser at  $f_{CW} = 378$  THz (793 nm) (Laser: NKT Photonics, Koheras ADJUSTIK; frequency-doubling waveguide: NTT Group) to which both combs are stabilized. Comb 1 is stabilized by locking one of its comb lines via a phase locked



loop (PLL) to the frequency  $f_{\text{CW}} + 185$  MHz. The same is true for Comb 2, except that its lock frequency is set to  $f_{\text{CW}} + 105$  MHz, leading to a frequency difference, i.e. a beat frequency, of 80 MHz between the two locked comb modes (one from each comb). The feedback of the PLL is split into a slow part with a bandwidth of  $\sim 6$  Hz responsible for long-term stability, and a fast part with a bandwidth of about 300 kHz for comb-line-linewidth minimization. The performance of the PLL is displayed in Fig. 5.4. The ratio between the analyzer-radio-bandwidth-limited carrier peak and residual noise or signals is larger than 30 dB for both combs. The figure shows symmetric sidebands appearing at a frequency-displacement of  $\sim 100$  kHz relative to the carrier peak. This frequency corresponds to the instruction execution rate of a microcontroller in the Taccor laser driver. These sidebands could therefore be associated with a parasitic electric signal feeding through to the PLL electric circuitry [120]. The shown traces also exhibit servo bumps at displacements of  $\sim 300$ -400 kHz around the carrier.

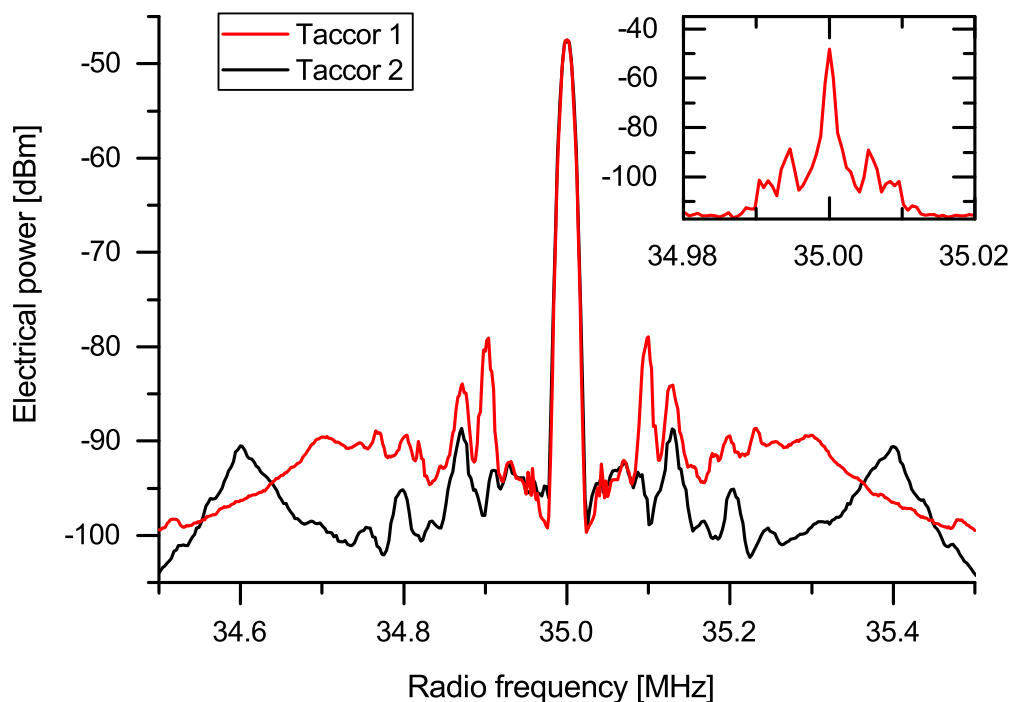


Figure 5.4: Beat-note measurement of the respective comb (Comb 1 in red, Comb 2 in black) and a free-running frequency-doubled 1586 nm CW Er fiber laser. The CW laser's linewidth is specified as  $< 0.1$  kHz at  $120 \mu\text{s}$  measurement time. Both combs are locked to this CW laser via its respective beat note. The spectra were recorded at a resolution bandwidth (RBW) of 1 kHz, a video bandwidth (VBW) of 3 Hz, and a sweep time (SWT) of 330 s. The inset shows a zoom into the central peak of the Comb 1 spectrum. The measurement parameters of this measurement are: RBW = 300 Hz, VBW = 3 Hz, SWT = 330 s.

All samples and solvents are commercially acquired and used as delivered without any further purification. Alexa Fluor® 488 and Alexa Fluor® 568 are purchased from Thermo Fisher Scientific, Rhodamine B is purchased from Sigma-Aldrich, and Coumarin 480 is purchased from Sirah Lasertechnik. Both Alexa fluorophores are dissolved in water (Sigma-Aldrich, ACS grade), Coumarin 480 and Rhodamine B are dissolved in ethanol (Sigma-Aldrich, SPECTRAL grade). The concentration is adjusted to yield a fluorescence output covering the dynamic range of the digitizer in the DC2pES experiment. No effort is devoted to the measurement of that concentration.

### 5.3 Results and Discussion

Example interferograms acquired with the setup described in the previous section are shown in Fig. 5.5 for Alexa Fluor® 488 and Rhodamine B. While the overall signal amplitude is comparable between the two measurements, the fringes, clearly visible in the Rhodamine B measurement, are near absent in the Alexa Fluor® 488 measurement. This smearing out of any fringes in the later measurement is likely to be caused by its significantly longer fluorescence lifetime of 4.1 ns (corresponding to a -6 dB bandwidth of 39 MHz) compared to Rhodamine B's fluorescence lifetime of 1.7 ns (corresponding to a -6 dB bandwidth of 94 MHz) [121]. Both of these values are smaller than the RF measurement frequency of  $2\eta f_0 \approx 160$  MHz, indicating that the fringe contrast, and hence the spectral signal-to-noise ratio (SNR) are reduced by the lifetime-low-pass-filter effect. The above value of 160 MHz is close to the -3 dB value of 175 MHz of the used current amplifier. However, no smaller values of  $2\eta f_0$  and  $\Delta f_{\text{rep}}$  were achievable due to the limited capability of the employed stabilization scheme to independently adjust these two degrees of freedom. A straight forward solution to this issue is to use a higher-bandwidth amplifier such as the variable-gain amplifier DUPVA-1-60 with a -3 dB cut-off of 1.2 GHz commercially available from FEMTO Messtechnik GmbH.

The interferograms in Fig. 5.5 are averages over 256 individual interferograms since the SNR of the Fourier transform of individual interferograms is not sufficient to yield any visible  $2f_0$  component. No special care could be taken to ensure that the averaged interferograms have an identical carrier-envelope phase. Therefore, it could not be excluded that the time-domain averaging would lead to distortions of interferograms with different phases of the RF carrier wave (see carrier-envelope description in Sec. 2.3 and 2.4). To still get a qualitative estimate on the potential magnitude of such distortions, the time-averaged interferograms (coherent

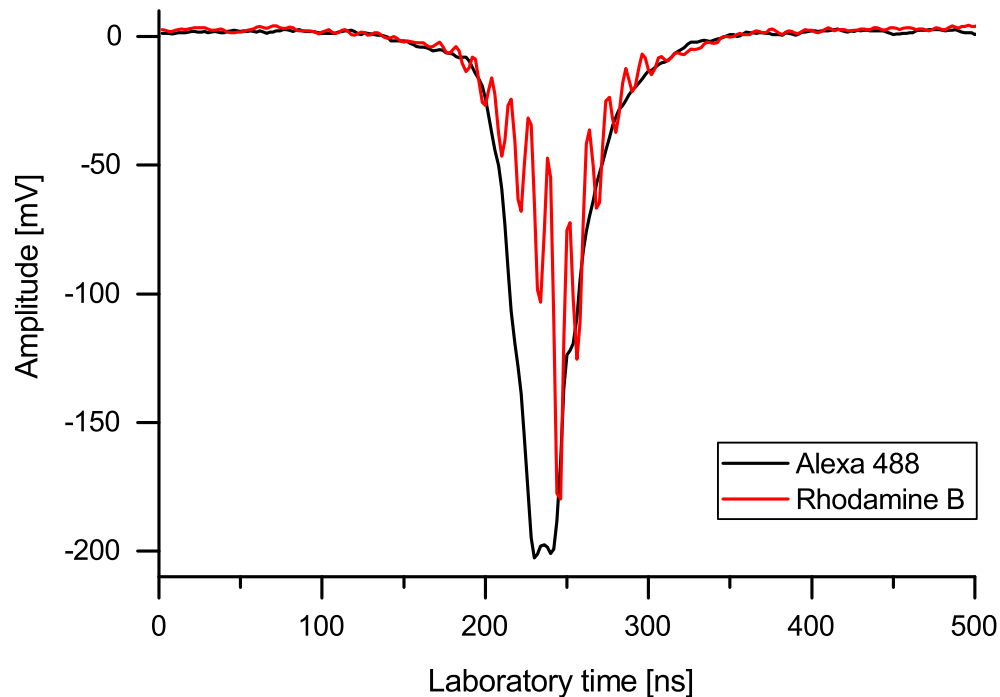


Figure 5.5: Comparison of the averaged interferograms of Alexa Fluor® 488 ( $\tau = 4.1$  ns) and Rhodamine B ( $\tau = 1.7$  ns). The averaging is performed in the time-domain with triggering of the acquisition on the interferogram itself. Apart from the sample exchange, the experimental configuration remained unchanged between the two acquisitions. The measurements were made with average laser powers (as measured in front of the focusing lens) of  $P_1 \approx 0.5$  W from Comb 1 and  $P_2 \approx 0.5$  W from Comb 2. The difference in repetition rate amounts to  $\Delta f_{\text{rep}} \approx 850$  Hz.

averaging) are compared with the phase-insensitive frequency-domain-averaging (incoherent averaging) of amplitude<sup>3</sup> spectra in Fig. 5.6.

Generally speaking, incoherent averaging does not affect the mean level of the noise floor, but only reduces its standard deviation. It can therefore be thought of as a way to determine the (average) amplitude spectrum of a single interferogram. In contrast, coherent averaging reduces the level of the noise floor, generally considered a good measure for the smallest detectable signal strength. Further details on these two averaging techniques can e.g. be found in Ref. [125, Appx. A]. In Fig. 5.6, the result of incoherent averaging is represented by the red trace and the

<sup>3</sup>No distinction between “amplitude” and “magnitude” is made here because: 1. All displayed spectra are normalized to a maximum value of 1 for better comparability between spectra. 2. Following common definitions [122, 123, 124, p.128], both of these quantities are only different by a scaling factor equaling the time-domain-trace length, which is the same within any given set of spectra displayed in the same figure.

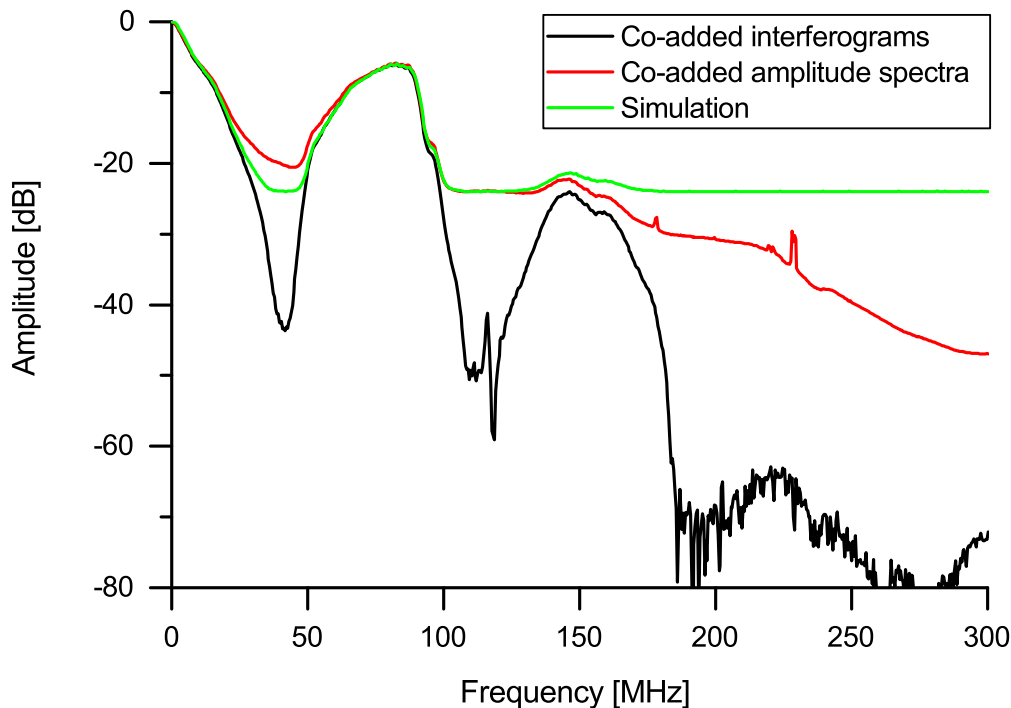


Figure 5.6: Averaging of condensed-phase DC2pES spectra. A total of 65536 traces were co-added in the time-domain to yield the black trace. The same 65536 interferograms were individually Fourier-transformed and the resulting amplitude spectra were co-added to yield the red trace. The result of a simulation of the phase-insensitive spectral amplitude average from the time-averaged interferogram associated with the black trace is shown in green. White noise is assumed for this simulation. Note that the spectra were acquired using a BBO crystal, so that lifetime-related filtering effects do not come into play. The measurement parameters are:  $P_1 \approx P_2 \approx 0.02$  W,  $\Delta f_{\text{rep}} \approx 900$  Hz. The shown data is plotted on a linear scale in Fig. C.3.

result of coherent averaging is represented by the black trace. A quantitative comparison is complicated by only having few regions where only noise and no signal is present (the peak in the 200–240 MHz range is suspiciously close to  $3\eta f_0$ ). Comparing the amplitude levels in the range of 186–201 MHz, which is chosen since there is no obvious signal present there and since the noise amplitude is comparably weakly effected by the limited amplifier bandwidth, yields a mean difference of  $42 \pm 5$  dB. This value is close to the SNR improvement of 48 dB that would be expected for averaging 65536 traces under the assumption of  $\sqrt{T}$  scaling, where  $T$  denotes the measurement time. Such a scaling of the SNR is generally found when white noise, in the form of photon noise prevalent in many fluorescence measurements [126], is the dominant noise type of a measurement apparatus.

When taking the coherently averaged interferogram and adding white noise of such an amplitude that the noise amplitude found in the 186-201 MHz range is reproduced after coherently averaging the resulting interferograms, the incoherently averaged purely white-noise limited spectrum can be simulated. The result of this simulation is represented by the green trace in Fig. 5.6. A comparison of the green and the red trace reveals a good agreement in central peak regions and comparably poor agreement at the flanks of the peaks, possibly attributable to phase distortions. Interestingly, though, the noise-dominated region between 110 and 130 MHz is in excellent agreement, supporting the assumption of white noise being dominant in the DC2pES measurements.

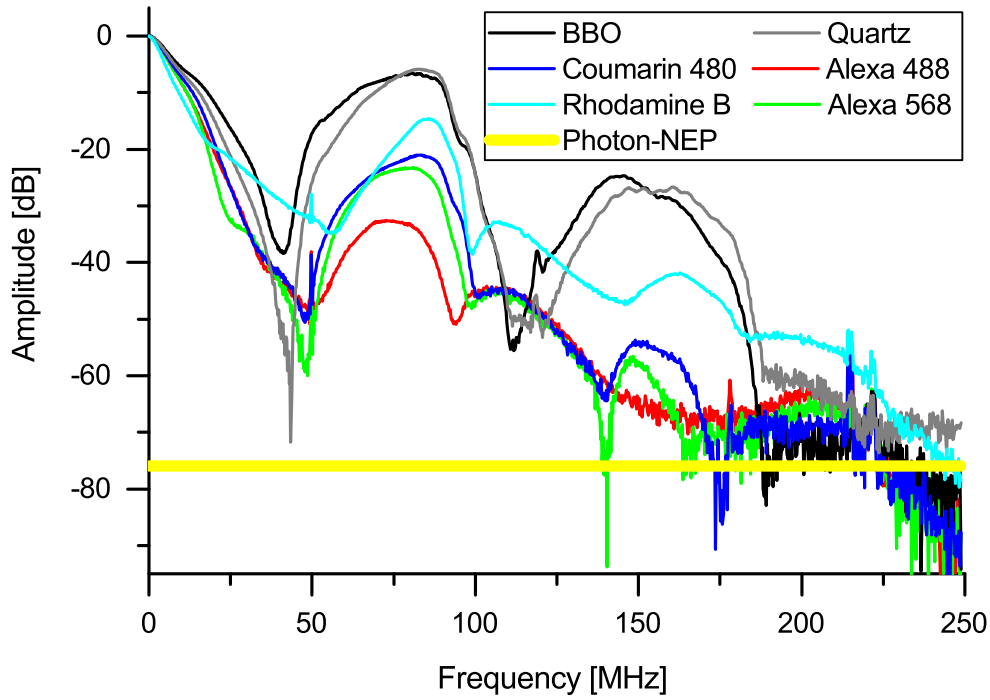


Figure 5.7: DC2pES spectra of fluorophores in liquid solution, as well as spectra of collinear quadratic interferometric cross-correlation measurements of quartz and BBO. All spectra were obtained by Fourier transformation of interferograms averaged over 262144 traces. The measurement parameters are:  $P_1 \approx P_2 \approx 0.5$  W,  $\Delta f_{\text{rep}} \approx 850$  Hz for all measurements except for the BBO measurement where only  $P_1 \approx P_2 \approx 0.02$  W are used. The yellow line indicates the estimated SNR limit set by photon noise. The shown experimental data is plotted on a linear scale in Fig. C.4.

The measured DC2pES spectra of all four fluorophores as well as of quartz and BBO are displayed on a logarithmic scale in Fig. 5.7. All spectra are multiplicatively normalized such that their respective largest value equals 1. The signals of all fluorophores at  $\eta f_0$  as well as  $2\eta f_0$

are significantly weaker than the reference signals (BBO/quartz). This is likely to be caused by the aforementioned lifetime-related filtering effect. The signal level of the  $2f_0$  component of Alexa Fluor® 488 is even too poor to be observable. In addition to the  $f_0$  (at ~50-100 MHz) and  $2f_0$  peaks (centered around ~160 MHz), signals at ~100-130 MHz appear in the fluorophore spectra. Such signals are also observed in Ref. [36] and assigned there to the  $f_{\text{FWM}} = 2f_1 - f_2$  four-wave mixing (FWM) process, where  $f_1$  and  $f_2$  the frequencies of participating excitation-laser photons. Here, values of  $f_1 \approx 400$  THz,  $f_2 \approx 360$  THz are well within the excitation bandwidths of the used excitation sources, leading to  $f_{\text{FWM}} = 440$  THz, which should appear close to the high-frequency side of the  $f_0$  peak, in agreement with observation. These two effects in conjunction with the necessary, but potentially distortion-causing averaging, however, render retrieval of source-spectrum-corrected two-photon fluorophore spectra insensible. This conclusion is also obvious from Fig. 5.8, where the isolated  $2f_0$  component is plotted on a linear scale. These spectra are normalized such that the largest value of their respective  $2f_0$  component equals 1.

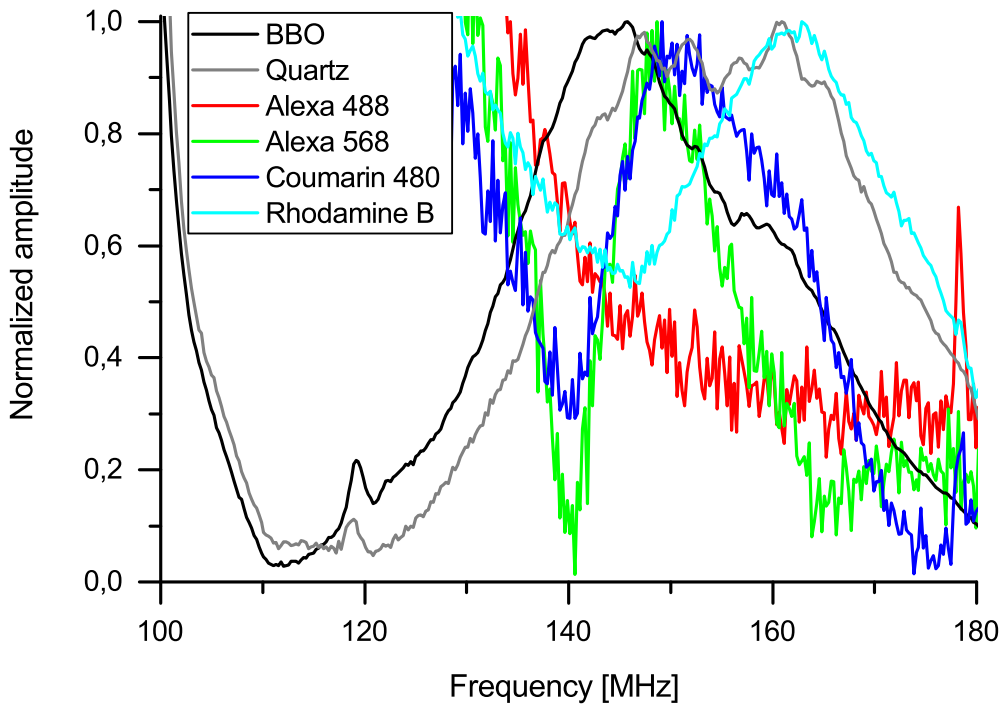


Figure 5.8: Expanded view of the DC2pES spectra shown in Fig. 5.7, isolating the  $2f_0$  component.

The measurement-time-limiting lifetime-lowpassing effect could be overcome by reducing  $\Delta f_{\text{rep}}$  by a factor of ten. This would limit the signal bandwidth to ~20 MHz, corresponding to

the lifetime-caused -3 dB value of Alexa Fluor® 488, and allow the measurement time for a single unaveraged interferogram to still stay within ~1-2  $\mu$ s. Alternatively, fluorophores with a shorter fluorescence lifetime can be chosen. An easily available fluorophore with strong two-photon absorption [127] in readily accessible wavelength regions ( $\lambda_{\text{abs. max}} = 780$  nm) would be Indocyanine Green, having a fluorescence lifetime of only 0.52 ns.

The SNR characteristics of the presented DC2pES spectra cannot be explained only based on photon-noise due to fluorescence photons: The photon-noise-limited SNR, plotted in yellow in Fig. 5.7, is significantly lower than the achieved SNR for all spectra. This is especially true for the case of Rhodamine B, where the signal levels are much larger than the noise-equivalent levels. The photon-noise-limited SNR estimate is based on calculating the shot-noise-equivalent-power (*NEP*) using [128]

$$NEP = \sqrt{P\hbar\omega B}, \quad (5.1)$$

where  $P$  is the average power of detected fluorescence,  $\omega$  is the fluorescence photons' angular frequency, and  $B$  is the measurement bandwidth, i.e.  $B = 1/T_{\text{FFT window}}$  for a single spectral FFT bin. A detailed description of the *NEP* calculation is provided in Sec. C.2. It is likely that the measured amplitude values do not reach the calculated noise-floor limit within the detection bandwidth because of competing FWM processes or, purely speculatively, higher-order nonlinear processes, re-absorption, or even chemical processes like aggregation. The probability of competing FWM processes to occur could be shifted in favor of two-photon absorption by making use of coherent control techniques [129]. This would not effect the measurement times, but it would counteract the prospective cost-reduction and miniaturization benefits of DC2pES when compared to Michelson-based techniques.

While the measurements in this chapter cannot be considered as a sufficient demonstration of the ability of DC2pES to produce two-photon spectra of condensed-phase molecules, it identifies a number of key steps that ought to be taken in the further development of the technique. Most importantly these include:

1. Improvement of the control over both comb-related degrees of freedom to allow for distortion-free phase-coherent averaging [130].
2. Choice of fluorophores with a shorter fluorescence lifetime such as Indocyanine Green and/or reduction of  $\Delta f_{\text{rep}}$  [127].
3. Utilization of coherent control techniques [129].
4. Improvement of the duty cycle [9].

The results presented here should therefore be seen as the first step towards the extension of direct-frequency comb spectroscopy to the realm of nonlinear electronic spectroscopy in the condensed phase.



## 6 Summary and Outlook

This thesis reports on first demonstrations of dual-comb two-photon–excitation spectroscopy (DC2pES). The described experiments fulfill a wide range of resolution requirements, ranging from a few MHz (Doppler free, Chap. 4), a few 100 MHz (Doppler limited, Chap. 3), to the THz range (condensed phase, Chap. 5). Only slight changes to the spectroscopic part of the setup need to be put into place to cover the respective range, thus highlighting the technique’s high degree of flexibility.

The experiments of Chap. 3 constitute the first proofs of the feasibility of DC2pES. One- and two-photon excitation spectra agreeing well with simulated spectra are simultaneously measured for both stable Rb isotopes within 18 s measurement time. Chapter 4 demonstrates the technique’s potential for precision spectroscopy by implementing a Doppler-cancellation scheme. A large number of hyperfine transitions of Rb are simultaneously excited and resolved at interleaving steps of 1 MHz. The spectral line shapes are again found to agree well with predictions and the achieved accuracy is consistent with explored systematic effects. Chapter 5 studies the possibility of applying DC2pES to high-speed, low-resolution ( $\gg 1$  GHz) experiments. First experiments allow to identify stability requirements and constraints due to the limited dynamic range of highly multiplexed DC2pES.

Looking at the road ahead, one can think of many ways how the presented experiments could evolve: Temporal chirp is known to potentially have a large impact on two-photon-excitation efficiency [131]. Its influence on DC2pES spectra was so far not carefully investigated and could lead to an increased excitation efficiency. On the other hand, it should also be checked for being a source of systematic frequency shifts. The excitation efficiency could also be increased by utilizing a higher-power laser system such as the widely used Ti:Sa frequency combs. Similarly, the fluorescence signal level could be increased by replacing the quartz glass of the Rb vapor cell, which is found to react with Rb at temperatures larger than 393 K, with Pyrex glass allowing for temperature beyond 423 K. The current geometrical photon collection

efficiency of about 1% can also be considerably increased by at least one order of magnitude by utilization of an integrating sphere.

The necessity of scanning the combs for high-resolution spectroscopy could be relaxed by making use of low-repetition-rate combs [132]. Such systems imply a reduced free spectral range in traditional DCS, limiting their utility for measuring many or broad transition lines with this scheme. This potential drawback is nonexistent in DC2pES. According to preliminary experiments in agreement with Ref. [133], the excitation combs spectral span can be increased by a factor of  $\sim 3$  by means of normal-dispersion photonic-crystal fibers. In regards of high-resolution experiments, this would allow to simultaneously measure the  $5S_{1/2}$ - $5P_{1/2}$  (at 795 nm) and  $5S$ - $7S$  (at  $2\times 760$  nm) transitions of Rb and the  $6S$ - $8S$  (at  $2\times 822$  nm) of Cs. A pulse shaper (readily available in the MPQ Laser Spectroscopy Division) could be inserted in the beam path to mitigate the different excitation and fluorescence efficiencies of Rb and Cs. In regards of condensed-phase experiments, it would allow to probe a full spectral fluorophore band. Lastly the implementation of new experiments would be greatly facilitated by implementing a hardware-based (FPGA) correction scheme allowing for on-the-fly visibility of high resolution spectra [134].

The true strength of DC2pES clearly lies in simultaneous high-resolution spectroscopy of a large number of transitions. Simultaneous interrogation of multiple molecular species in the gas-phase and acquisition of their densely covered narrow-linewidth broadband spectra [68, 69] is therefore a clear future goal of this technique. So is the extension to higher-order multi-photon processes, such as three-photon absorption, that could relax requirements on short-wavelength laser sources often arduously generated by high-harmonic generation. One could also think of a three-photon excitation scheme where the first photon is provided by a CW laser that promotes the sample into an excited (intermediate) state. The two remaining photons would then be provided by the dual comb and they would only resonantly interact with the velocity class selected by the cw laser, thus effectively canceling the Doppler broadening for one-photon-allowed transitions.

At this point it is safe to say that much developmental work and research is still required to convert DC2pES into a mature technology exploiting its full potential. However, as the technique holds much promise to constitute a meaningful advancement for an array of fields of applications this seems just too warranted.

# Appendix

## A Supplementary Information on Doppler-Limited Dual-Comb Two-Photon Spectroscopy on Rb

Some figures, associated with the experiments reported in Chap. 3, that are likely to be of much interest to only very few readers of this thesis are provided here.

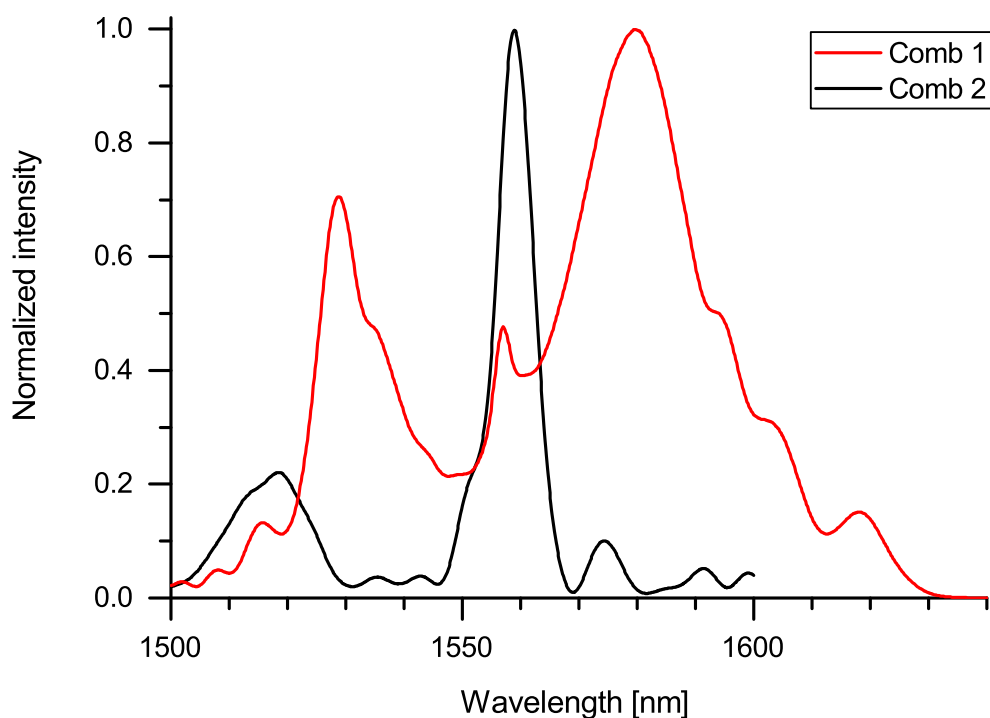


Figure A.1: Spectra of the Er-Oscillator-Amplifier lasers used in the Doppler-limited DC2pES Rb experiment. The spectrum of Comb 1 is drawn in red, the spectrum of Comb 2 is drawn in black.

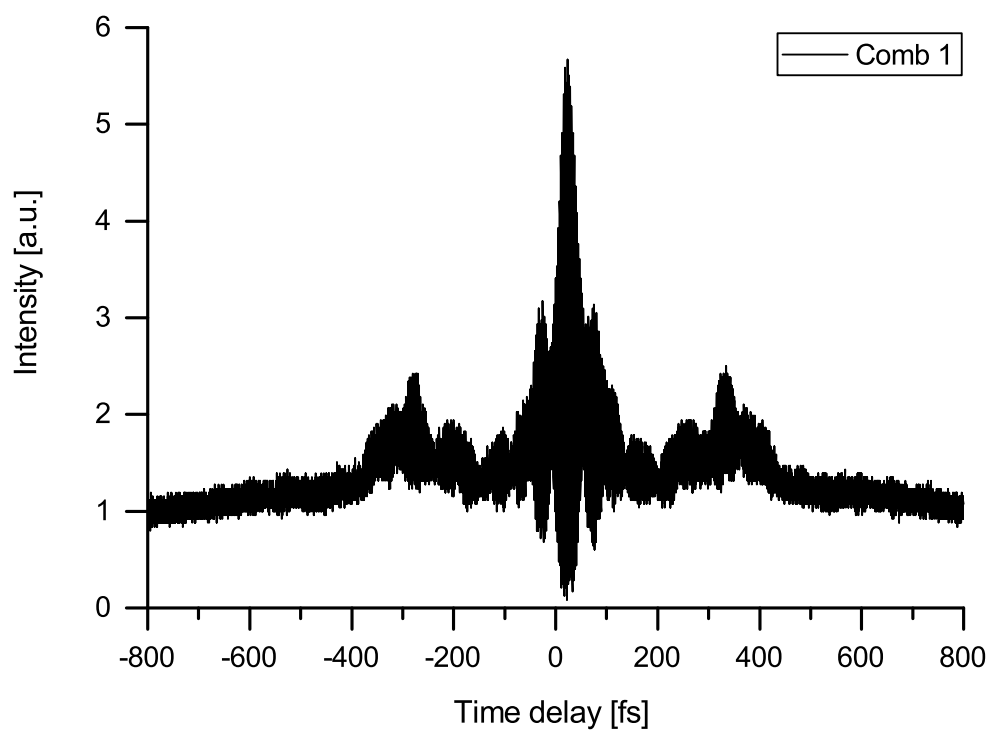


Figure A.2: Second-order interferometric autocorrelation trace of the Er-Oscillator-Amplifier laser Comb 1 used in the Doppler-limited DC2pES Rb experiment. The pulse FWHM, corresponding to the width of the central peak, is 30 fs.

## **B Supplementary Information on Doppler-Free Dual-Comb Two-Photon Spectroscopy on Rb**

### **B.1 Statistical Fit-Quality Measures**

Some statistical measures, associated with the fit reported in Sec. 4.4.2, that are likely to be of much interest to only very few readers of this thesis are provided here.

- Number of points: 9263
- Number of free parameters: 76
- Degrees of freedom (DoF) = Number of points - Number of free parameters = 9187
- Sum of squared residuals (SSR): 0.03331661039483
- SSR/DoF:  $3.626495090326 \cdot 10^{-6}$
- R-squared: 0.996710359029
- Adjusted R-squared: 0.9966827842027

### **B.2 Details on the Calculation of Transition Intensities**

The formula used for calculating the transition probability (Eq. 4.17), is given by Eq. 6.6. Its derivation is detailed below. Ground-state quantities are unprimed, final-state quantities are singly primed, and intermediate-state quantities are doubly primed. Note that  $q = 2$  for circularly polarized beams, whereas  $q = 0$  describes the case of linear polarization. In the calculation, it is assumed that all  $F$  and  $M_F$  levels in the intermediate state can be used with equal probability for the transition, but that only one  $J$  state participates. If all intermediate  $J$  states would contribute, one could simply finish after reducing the reduced matrix element  $\langle LSJ || T^2(\mu^2) || L'S'J' \rangle$  further to  $\langle L || T^2(\mu^2) || L' \rangle$ .

The derivation makes use of equations derived in Ref. [89, Sec. 4.3]. In going from Eq. 6.1 to Eq. 6.2, Eq. 4.44 in Ref. [89] is used. In going from Eq. 6.2 to Eq. 6.3, as well as in going from Eq. 6.4 to Eq. 6.5, Eq. 4.66 in Ref. [89] is used. The reduced matrix elements in the last equation are properties of the electronic transition and can be deduced from lifetime measurements of the transition [93, Sec. 3.3]. Squaring of Eq. 6.6 and summing over all  $M_F$  eliminates the phase factor, the  $3-j$  symbol, and the factor  $\sqrt{5}$ , and essentially Eq. 4.15 is retrieved.

$$I_{gf} \propto \langle LS J F M_F | T_q^2(\mu^2) | L' S J' I F' M'_F \rangle \quad (6.1)$$

$$= (-1)^{F-M_F} \begin{pmatrix} F & 2 & F' \\ -M_F & q & M'_F \end{pmatrix} \langle LS J I F | T^2(\mu^2) | L' S J' I F' \rangle \quad (6.2)$$

$$= (-1)^{F-M_F} \begin{pmatrix} F & 2 & F' \\ -M_F & q & M'_F \end{pmatrix} \cdot (-1)^{J+I+F'} \sqrt{(2F+1)(2F'+1)} \begin{Bmatrix} F & F' & 2 \\ J' & J & I \end{Bmatrix} \langle LS J | T^2(\mu^2) | L' S J' \rangle \quad (6.3)$$

$$= (-1)^{F-M_F+J+I+F'} \sqrt{(2F+1)(2F'+1)} \begin{pmatrix} F & 2 & F' \\ -M_F & q & M'_F \end{pmatrix} \begin{Bmatrix} F & F' & 2 \\ J' & J & I \end{Bmatrix} \cdot (-1)^{J+J'} \sqrt{5} \begin{Bmatrix} 1 & 1 & 2 \\ J' & J & J'' \end{Bmatrix} \langle LS J | T^1(\mu) | L'' S J'' \rangle \langle L'' S J'' | T^1(\mu) | L' S J' \rangle \quad (6.4)$$

$$= (-1)^{F-M_F-J'+I+F'} \sqrt{5(2F+1)(2F'+1)} \begin{pmatrix} F & 2 & F' \\ -M_F & q & M'_F \end{pmatrix} \begin{Bmatrix} F & F' & 2 \\ J' & J & I \end{Bmatrix} \begin{Bmatrix} 1 & 1 & 2 \\ J' & J & J'' \end{Bmatrix} \cdot (-1)^{L+S+J''+1} \sqrt{(2J+1)(2J''+1)} \begin{Bmatrix} J & J'' & 1 \\ L'' & L & S \end{Bmatrix} \langle L | T^1(\mu) | L'' \rangle \cdot (-1)^{L''+S+J'+1} \sqrt{(2J''+1)(2J'+1)} \begin{Bmatrix} J'' & J' & 1 \\ L' & L'' & S \end{Bmatrix} \langle L'' | T^1(\mu) | L' \rangle \quad (6.5)$$

$$= (-1)^{F-M_F-J'+I+F''+L''-L} \sqrt{5(2F+1)(2F'+1)(2J+1)(2J'+1)(2J''+1)} \cdot \begin{pmatrix} F & 2 & F' \\ -M_F & q & M'_F \end{pmatrix} \begin{Bmatrix} F & F' & 2 \\ J' & J & I \end{Bmatrix} \begin{Bmatrix} 1 & 1 & 2 \\ J' & J & J'' \end{Bmatrix} \begin{Bmatrix} J & J'' & 1 \\ L'' & L & S \end{Bmatrix} \begin{Bmatrix} J'' & J' & 1 \\ L' & L'' & S \end{Bmatrix} \cdot \langle L | T^1(\mu) | L'' \rangle \langle L'' | T^1(\mu) | L' \rangle \quad (6.6)$$

## C Supplementary Information on Liquid-Phase Dual-Comb Two-Photon Spectroscopy

### C.1 Linear-Scale Liquid-Phase Dual-Comb Two-Photon Spectra

Figure C.3 below shows the same data as Fig. 5.6, but on a linear scale.

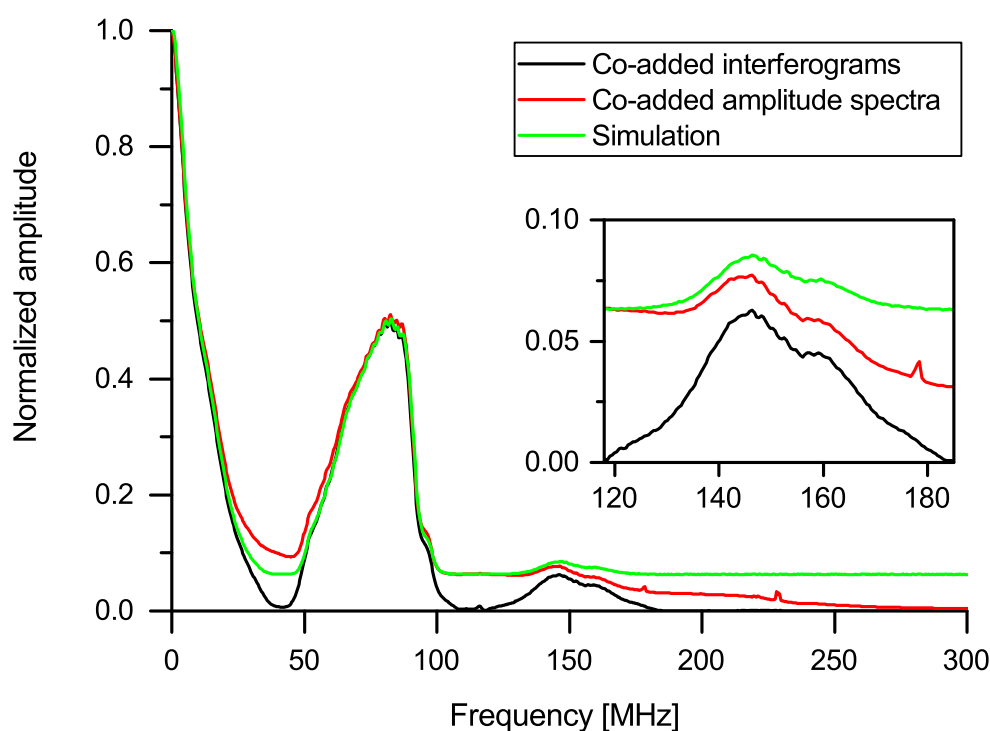


Figure C.3: Averaging of condensed-phase DC2pES spectra. A total of 65536 traces were co-added in the time-domain to yield the black trace. The same 65536 interferograms were individually Fourier-transformed and the resulting amplitude spectra were co-added to yield the red trace. The result of a simulation of the phase-insensitive spectral amplitude average from the time-averaged interferogram associated with the black trace is shown in green. White noise is assumed for this simulation. Note that the spectra were acquired using a BBO crystal, so that lifetime-related filtering effects do not come into play. The measurement parameters are:  $P_1 \approx P_2 \approx 0.02$  W,  $\delta f_{\text{rep}} \approx 900$  Hz.

Figure C.4 below shows the same experimental data as Fig. 5.7, but on a linear scale. Note that an expanded view on the  $2\omega_0$  component on a linear scale is provided by Fig. 5.8.

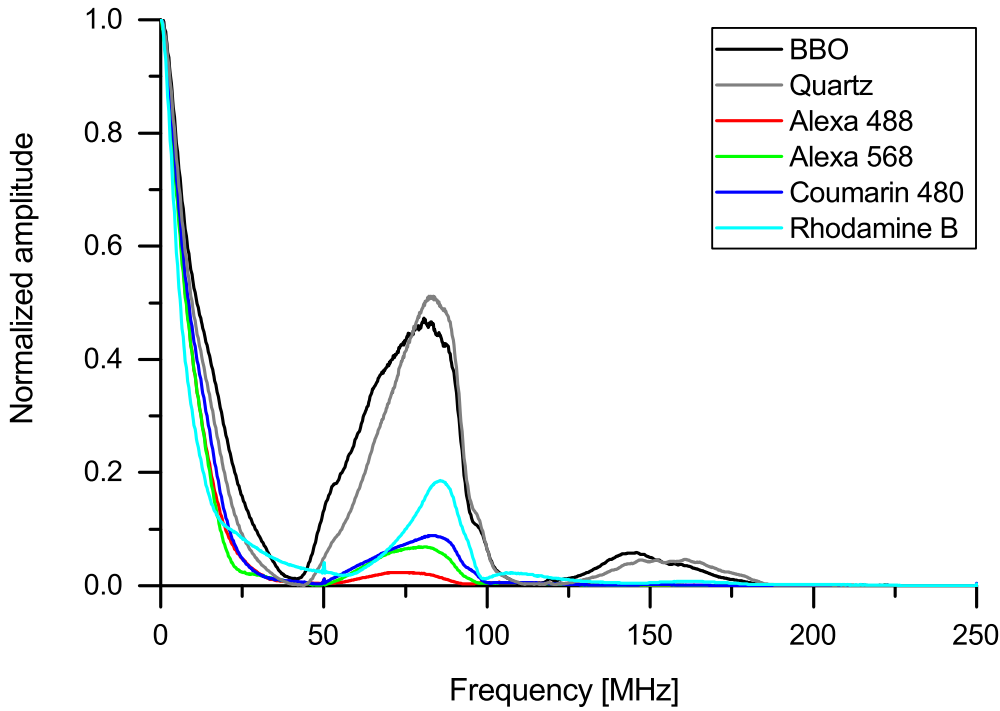


Figure C.4: DC2pES spectra of fluorophores in liquid solution, as well as spectra of collinear quadratic interferometric cross-correlation measurements of quartz and BBO. All spectra were obtained by Fourier transformation of interferograms averaged over 262144 traces. The measurement parameters are:  $P_1 \approx P_2 \approx 0.5$  W,  $\delta f_{\text{rep}} \approx 850$  Hz for all measurements except for the BBO measurement where only  $P_1 \approx P_2 \approx 0.02$  W are used.

## C.2 Details on the Calculation of the Shot-Noise-Equivalent Power

The photon-noise-limited SNR estimate is based on calculating the shot-noise-equivalent-power (NEP) using [128]

$$NEP = \sqrt{P\hbar\omega B}, \quad (6.7)$$

where  $P$  is the average power of detected fluorescence,  $\omega \approx 3.5$  PHz is the fluorescence photons' angular frequency, and  $B$  is the measurement resolution bandwidth, i.e.  $B = 1/T_{\text{FFT window}} = 244141$  Hz, corresponding to a single spectral FFT-bin width of the measurement. Note that Eq. 6.7 is generally used to estimate the noise-floor power level [128, 135]. Estimates for the noise root-mean-square error in the spectral domain<sup>1</sup> and associated SNRs can e.g. be found

<sup>1</sup>Using the root-mean-square error in the spectral domain as opposed to a noise-floor level is sensible for conventional absorption measurements, where signals are manifest as dips in the excitation spectrum of the



in Ref. [136]. The first step of the calculation is to determine the value of  $P$  in the DC2pES measurements. The acquired data encodes for voltages in units of volts. These voltage values can be converted into the PMT's current output by division through the current amplifier's gain of  $10^3$  V/A. The current emitted from the cathode, i.e. before amplification by the 8 internal amplification stages of the PMT, can be calculated by division through the PMT's gain curve,  $1.97 \cdot 10^6 \left(\frac{U_c}{V}\right)^8$  [137], where  $U_c$  denotes the used control voltage. A control voltage of  $\sim 0.6$  V is used in the experiments. This current is proportional to the incoming beam power and the proportionality constant is given by the (wavelength dependent) cathode radiant sensitivity. Its value is specified by the manufacturer of the PMT, Hamamatsu, e.g. 0.13 A/W at 400 nm [137]. From this, the resulting average light power incident on the PMT is calculated to  $P = 10.5 \mu\text{W}$  during the full trace length of 2048 points. Using Eq. 6.7 with the above values yields  $NEP = 1.4$  nW. Out of the 2048 points of the time trace, only 32 points visibly contained modulated signals, i.e. all 2048 points contribute noise, but only 32 points thereof contain signal. The average power of signal-carrying light incident on the PMT  $P_s$ , i.e. the average power associated with these 32 points only, corresponds to  $P_s = 0.55 \mu\text{W}$ . Using  $NEP = 1.4$  nW and  $P_s = 0.55 \mu\text{W}$  yields an SNR of +52 dB without averaging, and +106 dB with averaging over all 262144 recorded traces under the assumption of a scaling of the SNR with the square root of the measurement time. These SNR values are the shot-noise limited SNRs if all the signal were contained in a single FFT bin. The other extreme case would be if the signal would be spread uniformly over all 1024 FFT bins of the full Nyquist bandwidth. The resulting values for this case are -8 dB without averaging, and +46 dB including averaging. Neither of these two cases is found in the broadband DC2pES measurements, and the SNR values need to be scaled accordingly to accommodate for this. Another implication of having neither of these two cases realized in DC2pES measurements is that the "signal" in the signal-to-noise-ratio has no obvious definition anymore. In the present discussion, the term "signal" denotes the largest amplitude value out of all FFT bins. The amount of signal in this FFT bin, relative to the total signal strength of all FFT bins can be estimated from the measured DC2pES spectra themselves. The result of this estimate is 2%. Scaling the above SNR value  $P_s = 0.55 \mu\text{W}$  by this factor to yield the average light power corresponding to the highest amplitude value of the measured DC2pES spectra and then performing the SNR calculation as above yields an SNR of +72 dB. This is the value plotted in yellow in Fig. 5.7.

---

light source. In contrast, in the present fluorescence-based DC2pES spectra, signals are identified as peaks surmounting the noise floor.

# List of Abbreviations

- AC** – Alternating current  
**ADC** – Analog-to-digital converter  
**BBO** – Beta barium borate  
**CARS** – Coherent anti-Stokes Raman spectroscopy  
**CM** – Chirped mirrors  
**CW** – Continuous wave  
**DAQ** – Data acquisition system  
**DC** – Direct current  
**DCS** – Dual-optical-frequency-comb spectroscopy  
**DFCS** – Direct frequency-comb spectroscopy  
**DC2pES** – Dual-comb two-photon excitation spectroscopy  
**DDS** – Direct digital synthesizer  
**Er** – Erbium  
**FFT** – Fast Fourier transform  
**FPGA** – Field programmable gate array  
**FTS** – Fourier-transform spectroscopy  
**FWHM** – Full width at half its maximum value  
**FWM** - Four-wave mixing  
**H** – Hydrogen  
**LC-SLM** – Liquid-crystal spatial light-modulator  
**LN** – Lithium niobate  
**MgO:PPLN** – Magnesium-oxide-doped periodically-poled lithium niobate  
**NEP** – Shot-noise-equivalent power  
**OBD** – Optical beat detection  
**OFC** – Optical frequency combs  
**PD** – Photo detector  
**PLL** – Phase-locked loop  
**PMT** – Photomultiplier tube

**Rb** – Rubidium

**RBW** – Resolution bandwidth

**RF** – Radio frequency

**SH** – Second harmonic

**SHG** – Second-harmonic generation

**SNR** – Signal-to-noise ratio

**SWT** – Sweep time

**Ti:Sa** – Titanium sapphire

**VBW** – Video bandwidth

# List of Figures

2.1	Schematic of a Michelson Interferometer . . . . .	10
2.2	Principle of Optical Frequency Comb Generation . . . . .	14
2.3	Schematic of a Linear Dual-Comb Spectrometer . . . . .	16
2.4	Time-Domain Principle of a Dual-Comb Spectrometer . . . . .	17
2.5	Examples of Dual-Comb Absorption Spectra . . . . .	18
3.1	Rubidium Energy-Level Diagram . . . . .	27
3.2	Dual-Comb Two-Photon Schematic . . . . .	28
3.3	Spectrum and Second-Order Interferometric Autocorrelation Traces of the Er Combs . . . . .	30
3.4	Experimental Setup for Doppler-Limited DC2pES of Gas-Phase Rubidium . . . . .	31
3.5	Detailed Electrical Setup for Doppler-Limited DC2pES of Gas-Phase Rubidium . . . . .	32
3.6	Beat Notes of Comb 1 and Comb 2 with the 192 THz CW Laser. . . . .	34
3.7	Doppler-Limited Time-Domain DC2pES Fluorescence Signal . . . . .	36
3.8	Doppler-Limited Portions of the One- and Two-Photon Excitation Spectra of Rb . . . . .	37
3.9	Experimentally Recorded Doppler-Limited DC2pES Spectrum . . . . .	38
3.10	Portion of the Absorption Dual-Comb Spectrum of Rb . . . . .	39
4.1	Rubidium Energy Hyperfine-Level Diagram . . . . .	44
4.2	Experimental Setup for Doppler-Free DC2pES of Gas-Phase Rubidium . . . . .	46
4.3	Detailed Electrical Setup for Doppler-Free DC2pES of Gas-Phase Rubidium . . . . .	48
4.4	Correction Signals for the $f_{\text{DDS}} = 30.75$ MHz Measurement . . . . .	51
4.5	Doppler-Free Time-Domain DC2pES Fluorescence Signal . . . . .	55
4.6	Illustration of the Creation Process of an Interleaved Spectrum. . . . .	56
4.7	Doppler-Free DC2pES Spectrum of $^{85}\text{Rb}$ and $^{87}\text{Rb}$ Interleaved at 1 MHz . . . . .	57
4.8	Direct Single-Comb Spectrum Equivalent to the DC2pES Spectrum . . . . .	58
4.9	Comparison of the Experimental $5D_{5/2}$ Spectrum with the Corresponding Computed Spectrum . . . . .	59

---

4.10	Comparison of the Experimental $5S_{1/2}$ - $5D_{5/2}$ -Transition Spectrum with the Fitted Model Function . . . . .	63
4.11	Effect of Residual Magnetic Fields. . . . .	65
4.12	Systematic Shifts Due to the Dual-Comb Technique . . . . .	69
5.1	Absolute Two-Photon Cross Sections from the Literature. . . . .	76
5.2	Setup of Condensed-Phase DC2pES. . . . .	77
5.3	Laser Spectra of the Laser Quantum Taccor Lasers. . . . .	78
5.4	Optical Frequency Lock of the Laser Quantum Taccor Lasers. . . . .	79
5.5	Comparison of the Averaged Interferograms of Two Fluorophores. . . . .	81
5.6	Averaging of Condensed-Phase DC2pES Spectra. . . . .	82
5.7	DC2pES Spectra of Fluorophores in Liquid Solution. . . . .	83
5.8	$2f_0$ Spectral Component of DC2pES Fluorophore Solution. . . . .	84
A.1	Spectra of the Er-Oscillator-Amplifier Lasers used in the Doppler-Limited DC2pES Rb Experiment. . . . .	89
A.2	AC of the Er-Oscillator-Amplifier Laser Comb 1 used in the Doppler-Limited DC2pES Rb Experiment. . . . .	90
C.3	Averaging of Condensed-Phase DC2pES Spectra (Linear Scales). . . . .	93
C.4	DC2pES Spectra of Fluorophores in Liquid Solution (Linear Scales). . . . .	94

# List of Tables

4.1	Frequency-Pulling-Induced Shifts. . . . .	67
4.2	Summary of Systematic Shifts. . . . .	70
4.3	Summary of Measured Transition Frequencies and Comparison with Literature Data. . . . .	71

# Bibliography

- [1] T. W. Hänsch. Nobel lecture: Passion for precision. *Rev. Mod. Phys.*, 78(4):1297, 2006.
- [2] N. R. Newbury. Searching for applications with a fine-tooth comb. *Nature Photon.*, 5(4): 186, 2011.
- [3] P. R. Griffiths and J. A. de Haseth. *Fourier transform infrared spectrometry*, volume 171 of *Chemical analysis*. Wiley-Interscience, Hoboken, N.J., 2nd edition, 2007. ISBN 978-0-471-19404-0.
- [4] B. Bernhardt. *Dual Comb Spectroscopy*. Ph.D. thesis, Ludwig-Maximilians-Universität München, 2011.
- [5] K. A. Tillman, R. R. J. Maier, D. T. Reid, and E. D. McNaghten. Mid-infrared absorption spectroscopy of methane using a broadband femtosecond optical parametric oscillator based on aperiodically poled lithium niobate. *J. Opt. A: Pure Appl. Opt.*, 7(6):S408, 2005.
- [6] A. Bartels, D. Heinecke, and S. A. Diddams. 10-GHz Self-Referenced Optical Frequency Comb. *Science*, 326(5953):681, 2009.
- [7] T. J. Kippenberg, R. Holzwarth, and S. A. Diddams. Microresonator-Based Optical Frequency Combs. *Science*, 332(6029):555, 2011.
- [8] A. G. Griffith, R. K. W. Lau, J. Cardenas, Y. Okawachi, A. Mohanty, R. Fain, Y. H. D. Lee, M. Yu, C. T. Phare, C. B. Poitras, A. L. Gaeta, and M. Lipson. Silicon-chip mid-infrared frequency comb generation. *Nat. Commun.*, 6(6299), 2015.
- [9] T. Ideguchi, S. Holzner, B. Bernhardt, G. Guelachvili, N. Picqué, and T. W. Hänsch.

- Coherent Raman spectro-imaging with laser frequency combs. *Nature*, 502(7471):355, 2013.
- [10] W. Demtröder. *Laser spectroscopy 2: Experimental techniques*. Springer, 5th edition, 2015. ISBN 9783662446416.
- [11] Ye. V. Baklanov and V. P. Chebotayev. Narrow resonances of two-photon absorption of super-narrow pulses in a gas. *Appl. Phys.*, 12(1):97, 1977.
- [12] E. V. Baklanov and V. P. Chebotaev. Two-photon absorption of ultrashort pulses in a gas. *Sov. J. Quantum Electron.*, 7(10):1252, 1977.
- [13] B. Dick, R. M. Hochstrasser, and H. P. Trommsdorff. Resonant molecular optics. In D. S. Chemla and J. Zyss, editors, *Nonlinear optical properties of organic molecules and crystals*, volume 2 of *Quantum electronics—principles and applications: a series of monographs*, page 159. Academic Press, Orlando, 1987. ISBN 0323157769.
- [14] S. Mukamel. *Principles of Nonlinear Optical Spectroscopy*. Oxford University Press, USA, New York, 1999. ISBN 0195132912.
- [15] G. He and S. H. Liu. *Physics of nonlinear optics*. World Scientific, Singapore and River Edge and NJ, 1999. ISBN 9789810233198.
- [16] E. L. Degl’Innocenti and M. Landolfi. *Polarization in spectral lines*, volume 307 of *Astrophysics and space science library*. Kluwer Academic Publishers, Dordrecht and Boston, 2004. ISBN 9781402024146.
- [17] B. Falkenburg. *Particle metaphysics: A critical account of subatomic reality*. Frontiers collection. Springer, Berlin and New York, 2007. ISBN 9783540337317.
- [18] P. F. Dunn. *Measurement and data analysis for engineering and science*. McGraw-Hill series in mechanical engineering. McGraw-Hill Higher Education, Boston, 2005. ISBN 0072825383.
- [19] R. Glenn and S. Mukamel. Nonlinear transmission spectroscopy with dual frequency combs. *Phys. Rev. A*, 90(2):023804, 2014.
- [20] J. P. Ogilvie, K. J. Kubarych, A. Alexandrou, and M. Joffre. Fourier transform measure-



- ment of two-photon excitation spectra: applications to microscopy and optimal control. *Opt. Lett.*, 30(8):911, 2005.
- [21] Y. Silberberg and D. Meshulach. Coherent quantum control of two-photon transitions by a femtosecond laser pulse. *Nature*, 396(6708):239, 1998.
- [22] P. M. Goorjian and S. T. Cundiff. Nonlinear effects on the carrier-envelope phase. *Opt. Lett.*, 29(12):1363, 2004.
- [23] N. R. Newbury and B. R. Washburn. Theory of the frequency comb output from a femtosecond fiber laser. *IEEE J. Quantum Electron.*, 41(11):1388, 2005.
- [24] T. R. Schibli, I. Hartl, D. C. Yost, M. J. Martin, A. Marcinkevičius, M. E. Fermann, and J. Ye. Optical frequency comb with submillihertz linewidth and more than 10 W average power. *Nature Photon.*, 2(6):355, 2008.
- [25] S.-J. Lee, B. Widiyatmoko, M. Kourogi, and M. Ohtsu. Ultrahigh Scanning Speed Optical Coherence Tomography Using Optical Frequency Comb Generators. *Jpn. J. Appl. Phys.*, 40(Part 2, No. 8B):L878, 2001.
- [26] S. Schiller. Spectrometry with frequency combs. *Opt. Lett.*, 27(9):766, 2002.
- [27] F. Keilmann, C. Gohle, and R. Holzwarth. Time-domain mid-infrared frequency-comb spectrometer. *Opt. Lett.*, 29(13):1542, 2004.
- [28] T. Ideguchi, B. Bernhardt, G. Guelachvili, T. W. Hänsch, and N. Picqué. Raman-induced Kerr-effect dual-comb spectroscopy. *Opt. Lett.*, 37(21):4498, 2012.
- [29] N. F. Ramsey. A Molecular Beam Resonance Method with Separated Oscillating Fields. *Phys. Rev.*, 78(6):695, 1950.
- [30] J. C. Bergquist, S. A. Lee, and J. L. Hall. Saturated absorption with spatially separated laser fields: Observation of optical "Ramsey" fringes. *Phys. Rev. Lett.*, 38(4):159, 1977.
- [31] M. M. Salour and C. Cohen-Tannoudji. Observation of Ramsey's interference fringes in the profile of Doppler-free two-photon resonances. *Phys. Rev. Lett.*, 38(14):757, 1977.
- [32] A. Marian, M. C. Stowe, J. R. Lawall, D. Felinto, and J. Ye. United time-frequency spectroscopy for dynamics and global structure. *Science*, 306(5704):2063, 2004.

- [33] R. G. Beausoleil and T. W. Hänsch. Ultrahigh-resolution two-photon optical Ramsey spectroscopy of an atomic fountain. *Phys. Rev. A*, 33(3):1661, 1986.
- [34] M. Bellini, A. Bartoli, and T. W. Hänsch. Two-photon Fourier spectroscopy with femtosecond light pulses. *Opt. Lett.*, 22(8):540, 1997.
- [35] K. Isobe, A. Suda, M. Tanaka, F. Kannari, H. Kawano, H. Mizuno, A. Miyawaki, and K. Midorikawa. Fourier-transform spectroscopy combined with a 5-fs broadband pulse for multispectral nonlinear microscopy. *Phys. Rev. A*, 77(6):063832, 2008.
- [36] H. Hashimoto, K. Isobe, A. Suda, F. Kannari, H. Kawano, H. Mizuno, A. Miyawaki, and K. Midorikawa. Measurement of two-photon excitation spectra of fluorescent proteins with nonlinear Fourier-transform spectroscopy. *Appl. Opt.*, 49(17):3323, 2010.
- [37] T. Ideguchi, A. Poisson, G. Guelachvili, N. Picqué, and T. W. Hänsch. Adaptive real-time dual-comb spectroscopy. *Nat. Commun.*, 5(3375), 2014.
- [38] I. Coddington, W. C. Swann, and N. R. Newbury. Coherent dual-comb spectroscopy at high signal-to-noise ratio. *Phys. Rev. A*, 82(4):043817, 2010.
- [39] B. Bernhardt, A. Ozawa, P. Jacquet, M. Jacquy, Y. Kobayashi, Th. Udem, R. Holzwarth, G. Guelachvili, T. W. Hänsch, and N. Picqué. Cavity-enhanced dual-comb spectroscopy. *Nature Photon.*, 4(1):55, 2010.
- [40] A. Schliesser, M. Brehm, and F. Keilmann. Frequency-comb infrared spectrometer for rapid, remote chemical sensing. *Opt. Express*, 13(22):9029, 2005.
- [41] E. J. Catanzaro, T. J. Murphy, E. L. Garner, and W. R. Shields. Absolute isotopic abundance ratio and atomic weight of terrestrial rubidium. *J. Res. Natl. Bur. Stand. Sect. A*, 73(5):511, 1969.
- [42] J. M. Hollas. *High Resolution Spectroscopy*. Elsevier Science, Burlington, 1982. ISBN 1483100901.
- [43] J. E. Sansonetti. Wavelengths, Transition Probabilities, and Energy Levels for the Spectra of Rubidium (Rb I through Rb XXXVII). *J. Phys. Chem. Ref. Data*, 35(1):301, 2006.

- 
- [44] J. P. Connerade. *Highly excited atoms*, volume 9 of *Cambridge monographs on atomic, molecular, and chemical physics*. Cambridge University Press, Cambridge and New York, 1998. ISBN 9780521432320.
- [45] Z. Zheng, A. M. Weiner, K. R. Parameswaran, M.-H. Chou, and M. M. Fejer. Femtosecond second-harmonic generation in periodically poled lithium niobate waveguides with simultaneous strong pump depletion and group-velocity walk-off. *J. Opt. Soc. Am. B*, 19(4):839, 2002.
- [46] J. Luo, Y. Wang, W. Liang, J. Fonseca-Campos, and C.-Q. Xu. Characteristics of femtosecond second-harmonic generation in periodically poled lithium niobate. In *Photonics North 2006*, page 634349. International Society for Optics and Photonics, 2006.
- [47] R. DeSalvo, D. J. Hagan, M. Sheik-Bahae, G. Stegeman, E. W. van Stryland, and H. Vanherzeele. Self-focusing and self-defocusing by cascaded second-order effects in KTP. *Opt. Lett.*, 17(1):28, 1992.
- [48] A. Bostani, A. Tehranchi, and R. Kashyap. Engineering of effective second-order nonlinearity in uniform and chirped gratings. *J. Opt. Soc. Am. B*, 29(10):2929, 2012.
- [49] A. Bostani, M. Ahlawat, A. Tehranchi, R. Morandotti, and R. Kashyap. Tailoring and tuning of the broadband spectrum of a step-chirped grating based frequency doubler using tightly-focused Gaussian beams. *Opt. Express*, 21(24):29847, 2013.
- [50] D. Sheng, A. Pérez Galván, and L. A. Orozco. Lifetime measurements of the 5d states of rubidium. *Phys. Rev. A*, 78(6):062506, 2008.
- [51] M. J. Snadden, R. B. M. Clarke, and E. Riis. FM spectroscopy in fluorescence in laser-cooled rubidium. *Opt. Commun.*, 152(4–6):283, 1998.
- [52] Ph. Marteau, J. Obriot, C. Chalier, and G. H. Arie. Phase error correction in real time Fourier transform spectroscopy. *Infrared Phys.*, 16(3):345, 1976.
- [53] D. B. Chase. Phase Correction In Fourier Transform Infrared (FTIR). In Hajime Sakai, editor, *1981 International Conference on Fourier Transform Infrared Spectroscopy*, SPIE Proceedings, page 252. SPIE, 1981.

- [54] C. D. Porter and D. B. Tanner. Correction of phase errors in fourier spectroscopy. *Int. J. Infrared Milli. Waves*, 4(2):273, 1983.
- [55] J.-D. Deschênes, P. Giaccari, and J. Genest. Optical referencing technique with CW lasers as intermediate oscillators for continuous full delay range frequency comb interferometry. *Opt. Express*, 18(22):23358, 2010.
- [56] A. Papandreou-Suppappola. *Applications in time-frequency signal processing*. The electrical engineering and applied signal processing series. CRC Press, Boca Raton, 2003. ISBN 9781420042467.
- [57] M. Prevedelli, T. Freearde, and T. W. Hänsch. Phase locking of grating-tuned diode lasers. *Appl. Phys. B*, 60(2):3, 1995.
- [58] T. Ideguchi, A. Poisson, G. Guelachvili, N. Picqué, and T. W. Hänsch. Adaptive dual-comb spectroscopy in the green region. *Opt. Lett.*, 37(23):4847, 2012.
- [59] U. D. Rapol, A. Krishna, and V. Natarajan. Precise measurement of hyperfine structure in the  $5P_{3/2}$  state of  $^{85}\text{Rb}$ . *Eur. Phys. J. D*, 23(2):185, 2003.
- [60] A. Banerjee, D. Das, and V. Natarajan. Absolute frequency measurements of the D1 lines in  $^{39}\text{K}$ ,  $^{85}\text{Rb}$ , and  $^{87}\text{Rb}$  with  $\sim 0.1$  ppb uncertainty. *Europhys. Lett.*, 65(2):172, 2004.
- [61] F. Nez, F. Biraben, R. Felder, and Y. Millerioux. Optical frequency determination of the hyperfine components of the  $5P_{1/2} - 5D_{3/2}$  two-photon transitions in rubidium. *Opt. Commun.*, 102(5,6):432, 1993.
- [62] R. F. Gutterres, C. Amiot, A. Fioretti, C. Gabbanini, M. Mazzoni, and O. Dulieu. Determination of the  $^{87}\text{Rb}$  5p state dipole matrix element and radiative lifetime from the photoassociation spectroscopy of the  $\text{Rb}_2 0_g^- (P_{3/2})$  long-range state. *Phys. Rev. A*, 66(2):024502, 2002.
- [63] A. Marian, M. C. Stowe, D. Felinto, and J. Ye. Direct Frequency Comb Measurements of Absolute Optical Frequencies and Population Transfer Dynamics. *Phys. Rev. Lett.*, 95(2):023001, 2005.
- [64] P. Fendel, S. D. Bergeson, Th. Udem, and T. W. Hänsch. Two-photon frequency comb spectroscopy of the 6s-8s transition in cesium. *Opt. Lett.*, 32(6):701, 2007.

- 
- [65] J. Wu, D. Hou, Z. Qin, Z. Zhang, and J. Zhao. Observation of Rb two-photon absorption directly excited by an erbium-fiber-laser-based optical frequency comb via spectral control. *Phys. Rev. A*, 89(4):041402, 2014.
- [66] J. N. Eckstein, A. I. Ferguson, and T. W. Hänsch. High-Resolution Two-Photon Spectroscopy with Picosecond Light Pulses. *Phys. Rev. Lett.*, 40(13):847, 1978.
- [67] K. N. Rao. *Spectroscopy of the earth's atmosphere and interstellar medium*. Elsevier Science, Oxford, 1992. ISBN 0323146759.
- [68] W. K. Bischel, Patrick J. Kelly, and C. K. Rhodes. Observation of Doppler-Free Two-Photon Absorption in the  $\nu_3$  Bands of  $\text{CH}_3\text{F}$ . *Phys. Rev. Lett.*, 34(6):300, 1975.
- [69] E. Riedle, H. J. Neusser, and E. W. Schlag. Electronic spectra of polyatomic molecules with resolved individual rotational transitions: Benzene. *J. Chem. Phys.*, 75(9):4231, 1981.
- [70] J. P. Doering. Electronic energy levels of benzene below 7 eV. *J. Chem. Phys.*, 67(9):4065, 1999.
- [71] T. J. Quinn. Practical realization of the definition of the metre, including recommended radiations of other optical frequency standards (2001). *Metrologia*, 40(2):103, 2003.
- [72] L. S. Vasilenko, V. P. Chebotaev, and A. V. Shishaev. Line Shape of Two-Photon Absorption in a Standing-Wave Field in a Gas. *JETP Letters*, 12(3):113, 1970.
- [73] F. Biraben, B. Cagnac, and G. Grynberg. Experimental Evidence of Two-Photon Transition without Doppler Broadening. *Phys. Rev. Lett.*, 32(12):643, 1974.
- [74] P. L. Kelley, H. Kildal, and H. R. Schlossberg. Highly selective excitation of atoms and molecules using two-photon processes. *Chem. Phys. Lett.*, 27(1):62, 1974.
- [75] T. W. Hänsch, K. C. Harvey, G. Meisel, and A. L. Schawlow. Two-photon spectroscopy of Na 3s-4d without Doppler broadening using a cw dye laser. *Opt. Commun.*, 11(1):50, 1974.
- [76] R. Teets, J. Eckstein, and T. W. Hänsch. Coherent Two-Photon Excitation by Multiple Light Pulses. *Phys. Rev. Lett.*, 38(14):760, 1977.

- [77] M. C. Stowe, M. J. Thorpe, A. Pe'er, J. Ye, J. E. Stalnaker, V. Gerginov, and S. A. Diddams. Direct frequency comb spectroscopy. volume 55 of *Advances in Atomic, Molecular, and Optical Physics*, page 1. Elsevier, 2008. ISBN 9780123737106.
- [78] A. J. Olson, E. J. Carlson, and S. K. Mayer. Two-photon spectroscopy of rubidium using a grating-feedback diode laser. *Am. J. Phys.*, 74(3):218, 2006.
- [79] K. Predehl. *A 920 km optical fiber link for frequency metrology at the 19th decimal place*. Ph.D. thesis, Ludwig-Maximilians-Universität München, 2012.
- [80] C. J. Bordé. Forme de raie en spectroscopie à deux quanta sans élargissement Doppler. *C. R. Acad. Se. Paris*, 282(B):341, 1976.
- [81] A. Messiah. *Quantum mechanics*. Dover Books on Physics. Courier Corporation, 2014. ISBN 9780486784557.
- [82] M. A. Yuratich and D. C. Hanna. Nonlinear atomic susceptibilities. *J. Phys. B: At. Mol. Phys.*, 9(5):729, 1976.
- [83] Institute of Electronic Measurements KVARZ. Ch1-75a Active Hydrogen Maser. Available: <http://www.kvarz.com/general/1-75E.html> [Accessed 11 Oct. 2015].
- [84] A. Matveev. Personal communication, Nov. 2014.
- [85] S. Droste, F. Ozimek, Th. Udem, K. Predehl, T. W. Hänsch, H. Schnatz, G. Grosche, and R. Holzwarth. Optical-Frequency Transfer over a Single-Span 1840 km Fiber Link. *Phys. Rev. Lett.*, 111(11):110801, 2013.
- [86] M. Wojdyr. Fityk: A general-purpose peak fitting program. *J. Appl. Crystallogr.*, 43(5): 1126, 2010.
- [87] F. Biraben, M. Bassini, and B. Cagnac. Line-shapes in Doppler-free two-photon spectroscopy. The effect of finite transit time. *J. Phys. France*, 40(5):445, 1979.
- [88] A. Marian. *Direct Frequency Comb Spectroscopy for Optical Frequency Metrology and Coherent Interactions*. Ph.D. thesis, University of Colorado, 2005.
- [89] S. A. Meek. *A Stark Decelerator on a Chip*. Ph.D. thesis, Freie Universität Berlin, 2010.

- 
- [90] H.-C. Chui, M.-S. Ko, Y.-W. Liu, J.-T. Shy, J.-L. Peng, and H. Ahn. Absolute frequency measurement of rubidium 5S-7S two-photon transitions with a femtosecond laser comb. *Opt. Lett.*, 30(8):842, 2005.
- [91] B. P. Stoicheff and E. Weinberger. Frequency Shifts, Line Broadenings, and Phase-Interference Effects in Rb\*\*+Rb Collisions, Measured by Doppler-Free Two-Photon Spectroscopy. *Phys. Rev. Lett.*, 44(11):733, 1980.
- [92] C. B. Alcock, V. P. Itkin, and M. K. Horrigan. Vapour Pressure Equations for the Metallic Elements: 298–2500K. *Can. Metall. Quart.*, 23(3):309, 1984.
- [93] D. A. Steck. Rubidium 87 D line data. Available: <http://www.steck.us/alkalidata/rubidium87numbers.pdf> [Accessed 21 Oct. 2015], 2010.
- [94] W. G Pfann and J. H Hollomon. *Zone Melting*. Literary Licensing, LLC, 2013. ISBN 9781258799427.
- [95] J. Reader (CEO Ophos Instruments Inc.). Personal e-mail communication, July 2013.
- [96] I. Barmes, S. Witte, and K. S. E. Eikema. High-Precision Spectroscopy with Counter-propagating Femtosecond Pulses. *Phys. Rev. Lett.*, 111(2):023007, 2013.
- [97] L. Hilico, R. Felder, D. Touahri, O. Acef, A. Clairon, and F. Biraben. Metrological features of the rubidium two-photon standards of the BNM-LPTF and Kastler Brossel Laboratories. *Eur. Phys. J. Appl. Phys.*, 4(2):219, 1998.
- [98] J. E. Stalnaker, S. L. Chen, M. E. Rowan, K. Nguyen, T. Pradhananga, C. A. Palm, and D. F. Jackson Kimball. Velocity-selective direct frequency-comb spectroscopy of atomic vapors. *Phys. Rev. A*, 86(3):033832, 2012.
- [99] J. Dempster. *The laboratory computer: A practical guide for physiologists and neuroscientists*. Biological techniques series. Academic Press, London, 2001. ISBN 0122095510.
- [100] J. R. Wolberg. *Data analysis using the method of least squares: Extracting the most information from experiments*. Springer, Berlin and New York, 2006. ISBN 9783540256748.
- [101] E. Peters, D. C. Yost, A. Matveev, T. W. Hänsch, and Th. Udem. Frequency-comb

- spectroscopy of the hydrogen 1S-3S and 1S-3D transitions. *Ann. Phys.*, 525(7):L29, 2013.
- [102] D. C. Yost, A. Matveev, E. Peters, A. Beyer, T. W. Hänsch, and Th. Udem. Quantum interference in two-photon frequency-comb spectroscopy. *Phys. Rev. A*, 90(1):012512, 2014.
- [103] E. R. Tkaczyk, A. H. Tkaczyk, K. Mairing, J. Y. Ye, J. R. Baker, and T. B. Norris. Control of Two-photon Fluorescence of Common Dyes and Conjugated Dyes. *J. Fluoresc.*, 19(3):517, 2009.
- [104] Hamamatsu Photonics K.K. LCOS-SLM (Liquid Crystal on Silicon - Spatial Light Modulator): X10468/X13267/X13138 series. Available: [http://www.hamamatsu.com/resources/pdf/ssd/x10468\\_series\\_etc\\_kacc1172e.pdf](http://www.hamamatsu.com/resources/pdf/ssd/x10468_series_etc_kacc1172e.pdf) [Accessed 5 Oct. 2015], 2015.
- [105] M. H. Brenner, D. Cai, J. A. Swanson, and J. P. Ogilvie. Two-photon imaging of multiple fluorescent proteins by phase-shaping and linear unmixing with a single broadband laser. *Opt. Express*, 21(14):17256, 2013.
- [106] J. P. Ogilvie, D. Débarre, X. Solinas, J.-L. Martin, E. Beaurepaire, and M. Joffre. Use of coherent control for selective two-photon fluorescence microscopy in live organisms. *Opt. Express*, 14(2):759, 2006.
- [107] P. Pantazis and W. Supatto. Advances in whole-embryo imaging: a quantitative transition is underway. *Nat. Rev. Mol. Cell. Biol.*, 15(5):327, 2014.
- [108] A. E. Siegman. *Lasers*. University Science Books, 1986. ISBN 0935702113.
- [109] H. Abramczyk. *Introduction to laser spectroscopy*. Elsevier, Amsterdam and Boston, 1st edition, 2005. ISBN 9780444516626.
- [110] O. Svelto. *Principles of lasers*. Plenum Press, New York, 4th edition, 1998. ISBN 9780306457487.
- [111] S. Potvin and J. Genest. Dual-comb spectroscopy using frequency-doubled combs around 775 nm. *Opt. Express*, 21(25):30707, 2013.



- [112] M. Kullmann, A. Hipke, P. Nuernberger, T. Bruhn, D. CG Götz, M. Sekita, D. M. Guldi, G. Bringmann, and T. Brixner. Ultrafast exciton dynamics after Soret-or Q-band excitation of a directly  $\beta$ ,  $\beta'$ -linked bisporphyrin. *Phys. Chem. Chem. Phys.*, 14(22): 8038, 2012.
- [113] A. Konara, V. V. Lozovoya, and M. Dantusa. Electronic dephasing of molecules in solution measured by nonlinear spectral inteferometry. *J. Spectrosc. Dyn.*, 4:26, 2014.
- [114] M. Wollenhaupt, A. Assion, and Th. Baumert. Short and Ultrashort Laser Pulses. In F. Träger, editor, *Springer Handbook of Lasers and Optics*, page 1047. Springer, Berlin, Heidelberg, 2012. ISBN 3642194095.
- [115] W. G. Fisher, E. A. Wachter, F. E. Lytle, M. Armas, and C. Seaton. Source-Corrected Two-Photon Excited Fluorescence Measurements between 700 and 880 nm. *Appl. Spectrosc.*, 52(4):536, 1998.
- [116] Developmental Recourse for Biophysical Imaging Optoelectronics, Cornell University. Two photon action cross sections. Available: [http://www.drbio.cornell.edu/cross\\_sections.html](http://www.drbio.cornell.edu/cross_sections.html) [Accessed 20 Feb. 2015], 2013.
- [117] M. J. Tauber, R. A. Mathies, X. Chen, and S. E. Bradforth. Flowing liquid sample jet for resonance Raman and ultrafast optical spectroscopy. *Rev. Sci. Instrum.*, 74(11):4958, 2003.
- [118] V. Mizrahi and J. E. Sipe. Phenomenological treatment of surface second-harmonic generation. *J. Opt. Soc. Am. B*, 5(3):660, 1988.
- [119] Th. Tsang. Optical third-harmonic generation at interfaces. *Phys. Rev. A*, 52(5):4116, 1995.
- [120] A. Bartels (CEO Laser Quantum GmbH). Personal phone communication, 2014.
- [121] ISS Inc. Lifetime Data of Selected Fluorophores. Available: [http://www.iss.com/resources/reference/data\\_tables/LifetimeDataFluorophores.html](http://www.iss.com/resources/reference/data_tables/LifetimeDataFluorophores.html) [Accessed 2 Sept. 2015].
- [122] OriginLab Corporation. Algorithms (FFT). Available: <http://www.originlab.com/doc/Origin-Help/FFT1-Algorithm> [Accessed 25 Sept. 2015].

- [123] National Instruments Corporation. The Fundamentals of FFT-Based Signal Analysis and Measurement in LabVIEW and LabWindows/CVI. Available: <http://www.ni.com/white-paper/4278/en/> [Accessed 25 Sept. 2015].
- [124] C. L. Lubbers. *On gas pockets in wastewater pressure mains and their effect on hydraulic performance*, volume 11/2007 of *Delft Hydraulics select series*. IOS Press, Amsterdam, Netherlands, 2007. ISBN 9781586037895.
- [125] E. Janssen and A. H. M. van Roermund. *Look-ahead based sigma-delta modulation. Analog circuits and signal processing*. Springer, Dordrecht and New York, 2011. ISBN 978-94-007-1387-1.
- [126] E. L. Wehry. *Modern Fluorescence Spectroscopy*. Modern Analytical Chemistry. Springer US, Boston and MA, 1981. ISBN 146841092X.
- [127] K. Murari, Y. Zhang, S. Li, Y. Chen, M.-J. Li, and X. Li. Compensation-free, all-fiber-optic, two-photon endomicroscopy at 1.55  $\mu\text{m}$ . *Opt. Lett.*, 36(7):1299, 2011.
- [128] C. A. DiMarzio. *Optics for Engineers*. CRC Press, Hoboken, 2011. ISBN 1439897042.
- [129] V. V. Lozovoy, I. Pastirk, K. A. Walowicz, and M. Dantus. Multiphoton intrapulse interference. II. Control of two- and three-photon laser induced fluorescence with shaped pulses. *J. Chem. Phys.*, 118(7):3187, 2003.
- [130] E. Baumann, F. R. Giorgetta, W. C. Swann, A. M. Zolot, I. Coddington, and N. R. Newbury. Spectroscopy of the methane  $\nu_3$  band with an accurate midinfrared coherent dual-comb spectrometer. *Phys. Rev. A*, 84(6):062513, 2011.
- [131] A. Ozawa and Y. Kobayashi. Chirped-pulse direct frequency-comb spectroscopy of two-photon transitions. *Phys. Rev. A*, 86(2):022514, 2012.
- [132] A. Ozawa, Z. Zhao, M. Kuwata-Gonokami, and Y. Kobayashi. High average power coherent vuv generation at 10 MHz repetition frequency by intracavity high harmonic generation. *Opt. Express*, 23(12):15107, 2015.
- [133] J. M. Dudley, G. Genty, and S. Coen. Supercontinuum generation in photonic crystal fiber. *Rev. Mod. Phys.*, 78(4):1135, 2006.

- [134] J. Roy, J.-D. Deschênes, S. Potvin, and J. Genest. Continuous real-time correction and averaging for frequency comb interferometry. *Opt. Express*, 20(20):21932, 2012.
- [135] J. Taylor, F. Quinlan, and S. Diddams. Characterization of noise properties in photodetectors: A step toward ultra-low phase noise microwaves. Technical report, DTIC Document, 2009.
- [136] S. P. Davis, Mark C. Abrams, and J. W. Brault. *Fourier transform spectrometry*. Academic Press, San Diego, 2001. ISBN 9781281036629.
- [137] Hamamatsu Photonics K.K. Metal Package PMT: Photosensor Modules H10720/H10721 Series. Available: [http://www.hamamatsu.com/resources/pdf/etd/m-h10720\\_h10721e.pdf](http://www.hamamatsu.com/resources/pdf/etd/m-h10720_h10721e.pdf) [Accessed 12 Aug. 2015].

# Acknowledgements

- Mein Dank gebührt zunächst meinem Doktorvater Prof. Theodor W. Hänsch dafür mir die Möglichkeit gegeben zu haben, meine persönliche Forscherneugier unter exzellenten Bedingungen auszuleben. Diese Bedingungen sind insbesondere auf die vielen starken Wissenschaftler zurückzuführen, die er vermochte, am MPQ in seiner Division zu versammeln. Ihnen allen möchte ich für die stimulierenden wissenschaftlichen Diskussionen, aber auch für die schönen Wanderungen, Mountainbike-Touren, Skiausfahrten und Wakeboarding-Sessions danken!
- I'd like to thank Takuro Ideguchi, Antonin Poisson und Birgitta 'Gitti' Bernhardt for teaching me the nitty-gritty details of dual-comb spectroscopy when I was still a novice in the field. Some special thanks goes to Antonin for all his well-crafted and ingeniously-placed lab traps.
- Meinem Ph.D.-Leidensgenossen Simon Holzner möchte ich für viele heitere Momente danken die wohl uns beiden sehr dabei geholfen haben manch eine schwierige Situation gut wegzustecken. Der Austausch mit dir war immer "path-clearingly" hilfreich!
- Ich möchte meinem Kollegen Bernhard Bohn für all die Momente der gefühlten Normalität danken, die durch dich in unsere Gruppe kamen. Du kannst stolz auf deine Arbeit sein! Mögest du für selbige bei den Feldmännern die verdiente Anerkennung erfahren. Who's the best? No! You ;>.
- My thanks also goes to my quasi-successors Kathrin Mohler and Zaijun Chen. Your Ph.D.-hat production skills are something to behold, while your lab-skills are getting there. J/k ;-). I always very much enjoyed your company! May you manage to get your Ph.D. with the least possible amount of brain damage.
- I'd like to thank our "How about we go back to work?"-PostDoc Ming Yan for always making sure we don't waste too much time having lunch, so that we can have lovely

---

hot-pot sessions in the evenings. Thanks also for sharing your insightful knowledge with me. I wish to you that your multitude of nicely sophisticated “in preperation” papers will all get submitted and accepted.

- Einen besonderen Dank möchte ich Samuel A. Meek aussprechen. Der alte Spruch “Alleine schafft man nicht so viel wie zu zweit, auch nicht die Hälfte.” hat sich während meiner Ph.D.-Zeit einmal mehr bewahrheitet. Nur durch den intensiven Austausch mit dir war es mir möglich all die in dieser Arbeit vorgestellten Ergebnisse zu erzielen. Behalte dir deine unkapriziöse Art! Die Arbeitszeit, aber vor allem die Freizeit, die ich mit dir verbracht habe, hat mir immer große Freude bereitet. Hoffentlich sieht man sich noch viel öfter, auch wenn du jetzt erst mal wo anders gestrandet bist. In any case, may your own group grow and prosper!
- I’d like to extend the preceding wish to our highly talented further former or current PostDocs, Kana Iwakuni, Pei-Ling Luo, and Clément Lafargue. Thanks for sharing your knowledge with me and for joining and organizing many pleasant dinners.
- Ich möchte auch meinen Eltern, Arthur und Monika Hipke, meinem Bruder Viktor Hipke, sowie meinen Großeltern, Friedrich und Barbara Hipke und Lydia Brikardin für all die Fürsorge und Unterstützung danken die ich durch euch erfahren durfte. Jeder Erfolg den ich feier ist zu mindestens gleichen Teilen euer Erfolg. Danke euch für alles!
- Meiner geliebten Freundin Katrin möchte ich für die unzähligen wundervollen Momente danken die mein Leben so unendlich bereichern. Es werden noch viele mehr kommen. Ich freue mich auf mein Leben mit dir.

# List of Publications

## Journal Articles

A. Hipke, S. A. Meek, T. W. Hänsch, and N. Picqué. Broadband Doppler-free two-photon excitation spectroscopy with laser frequency combs. *In preparation*, 2016.

A. Hipke, S. A. Meek, T. Ideguchi, T. W. Hänsch, and N. Picqué. Broadband Doppler-limited two-photon and stepwise excitation spectroscopy with laser frequency combs. *Phys. Rev. A*, 90(1):011805, 2014.

M. Kullmann, A. Hipke, P. Nuernberger, T. Bruhn, D. C. G. Götz, M. Sekita, D. M. Guldi, G. Bringmann, and T. Brixner. Ultrafast exciton dynamics after Soret-or Q-band excitation of a directly  $\beta,\beta'$ -linked bisporphyrin. *Phys. Chem. Chem. Phys.*, 14(22):8038, 2012.

A. Hipke, S. Lübeck, and H. Hinrichsen. Absorbing boundaries in the conserved Manna model. *J. Stat. Mech.*, (7):P07021, 2009.

## Conference Contributions

A. Hipke, S. A. Meek, N. Picqué, and T. W. Hänsch. Doppler-free broadband two-photon excitation spectroscopy with two optical frequency combs. In *DPG-Verhandlungen*. German Physical Society (DPG), 2014.

A. Hipke, S. A. Meek, G. Guelachvili, T. W. Hänsch, and N. Picqué. Doppler-free broad spectral bandwidth two-photon spectroscopy with two laser frequency combs. In *CLEO: Science and Innovations*, page CTh5C.8. Optical Society of America (OSA), 2013.

A. Hipke, S. A. Meek, T. W. Hänsch, and N. Picqué. Highly multiplexed dual-comb two-photon excitation spectroscopy. In *CLEO: Science and Innovations*, page CTu3H.3. Optical Society of America (OSA), 2013.

# Curriculum Vitae

## Institutional Address

Max Planck Institute of Quantum Optics  
Hans-Kopfermann-Straße 1  
85748 Garching, Germany  
PHONE: +49 89 3 29 05 - 286  
E-MAIL: arthur.hipke@mpq.mpg.de

## Personal Data

NAME: Arthur Hipke  
DATE OF BIRTH: 18 July 1986  
PLACE OF BIRTH: Duschanbe, Tajikistan  
NATIONALITY: German

## Education

- SEPT. 2011 – Ph.D., Ludwig Maximilians University, Munich, Germany &  
PRESENT Max Planck Institute of Quantum Optics, Garching, Germany  
Thesis: “Dual-frequency-comb two-photon spectroscopy”  
Laboratory of Prof. Dr. Theodor W. Hänsch
- OCT. 2008 – Master of Science with Honors, FOKUS Physics, Julius Maximilians University,  
JULY 2011 Würzburg, Germany  
Thesis: “Ultrafast dynamics of a new, intrinsically chiral model bisporphyrin”  
Laboratory of Prof. Dr. Tobias Brixner
- AUG. 2009 – Master of Science, Physics, Rutgers—The State University of New Jersey,  
MAY 2010 New Brunswick, NJ, USA  
Essay: “Beyond Monte Carlo: Novel techniques for the analysis of stochastic systems in biochemistry”  
Group of Prof. Dr. Eduardo D. Sontag



- APR. 2006 – Bachelor of Science, Physics, Julius Maximilians University, Würzburg,  
MAY 2009 Germany  
Thesis: “Influence of various boundary conditions on the behavior of the  
Manna model with a conserved background field”  
Group of Prof. Dr. Haye Hinrichsen
- JULY 2005 – Alternative Civilian Service  
MAR. 2006 Caritas Heilbronn-Hohenlohe, position as administration secretary
- SEPT. 1996 – Abitur (general qualification for university entrance),  
JUNE 2005 Justinus Kerner Gymnasium (secondary school), Heilbronn, Germany